

>>>> Final Technical Report <<<<

Submitted to the Air Force Office of Scientific Research

Report Period: 06-01-96 to 11-30-99

**Project Title: Radiation Physics and Reliability Issues in III-V Compound
Semiconductor Nanoscale Heterostructure Devices**

Grant Number: F49620-96-1-0173

Principal Investigator:

**Prof. S.M. Goodnick
Arizona State University
Department of Electrical Engineering
Tempe, AZ 85287 – 5706
PH: (602) 965-6410
FAX: (602) 965-3838
e-mail: stephen.goodnick@asu.edu**

Co-Principal Investigator

**Prof. S. Subramanian
Oregon State University
Department of Electrical and Computer Engineering
Corvallis, OR 97331-3211
PH: (541) 737-2974
FAX: (541) 737-1300
e-mail: subram@ece.orst.edu**

20000728 066

REPORT DOCUMENTATION PAGE

AFRL-SR-BL-TR-00-

Public reporting burden for this collection of information is estimated to average 1 hour per response, including gathering and maintaining the data needed, and completing and reviewing the collection of information, collection of information, including suggestions for reducing this burden, to Washington Headquarters Service, Paperwork Project, Suite 1204, Arlington, VA 22202-4302, and to the Office of Management and Budget, Paperwork Project, Suite 1204, Arlington, VA 22202-4302.

sources,
ct of this
Jefferson
}

0324

1. AGENCY USE ONLY (Leave blank)		2. REPORT DATE		3. REPORT TYPE AND DATES COVERED 01 Jun 96 to 30 Nov 99 Final	
4. TITLE AND SUBTITLE Radiation Physics and Reliability Issues in III-V Compound Semiconductor Nanoscale Heterstructure Devices				5. FUNDING NUMBERS 61102F 2305/BX	
6. AUTHOR(S) Dr S. M. Goodnick					
7. PERFORMING ORGANIZATION NAME(S) AND ADDRESS(ES) Oregon State University Dept of Electrical & Computer Engineering Corvallis, OR 97331-3211				8. PERFORMING ORGANIZATION REPORT NUMBER	
9. SPONSORING/MONITORING AGENCY NAME(S) AND ADDRESS(ES) AFOSR/NE 801 North Randolph Street, Rm 732 Arlington, VA 22203-1977				10. SPONSORING/MONITORING AGENCY REPORT NUMBER F49620-96-1-0173	
11. SUPPLEMENTARY NOTES					
12a. DISTRIBUTION AVAILABILITY STATEMENT Approved for public release, distribution unlimited				12b. DISTRIBUTION CODE	
13. ABSTRACT (Maximum 200 words) We have investigated the following three types of devices in this research program: (1) Heterojunction Bipolar Transistors (2) High Electron Mobility Transistors and (3) Resonant Tunneling Diodes. The following three types of radiation were used in our investigations: (a) Gamma radiation (b) Electron radiation and (c) Neutron radiation. Electrons constitute an important component of the trapped radiation in the earth's magnetic field (Van Allen's belt). Neutron and gamma radiation are encountered in the weapon's environment. Neutrons are also generated by the interaction of cosmic rays with earth's atmosphere.					
14. SUBJECT TERMS				15. NUMBER OF PAGES	
				16. PRICE CODE	
17. SECURITY CLASSIFICATION OF REPORT UNCLASSIFIED		18. SECURITY CLASSIFICATION OF THIS PAGE UNCLASSIFIED		19. SECURITY CLASSIFICATION OF ABSTRACT UNCLASSIFIED	
				20. LIMITATION OF ABSTRACT UL	

TABLE OF CONTENTS

Section	Page
1. Executive Summary	1
2. Interaction of Radiation with Materials	6
3. Radiation Effects in InP/InGaAs Heterojunction Bipolar Transistors	21
4. Radiation Effects in AlGaAs/GaAs Heterojunction Bipolar Transistors	47
5. Radiation Effects in High Electron Mobility Transistor Structures and Devices	56
6. Resonant Tunneling Diodes	69
7. Conclusions	73
BIBLIOGRAPHY	75

1. Executive Summary

Nuclear and space radiation environments cause significant changes in the performance of semiconductor devices and integrated circuits. Such changes may be temporary (e.g. soft errors in memories and logic circuits) or permanent leading to an eventual failure of the electronic subsystem. Hence there has been considerable emphasis placed on devising methods to reduce radiation-induced degradation of semiconductor devices. One approach to solving this problem is to develop radiation-hardened devices and circuits. A key step in developing radiation-hardened electronics is the understanding of the basic effects of radiation in electronic materials, devices and circuits. Understanding the basic mechanisms can lead to several benefits. 1. Reliable predictions of the radiation response of the devices in the radiation environments of interest can be made. 2. Novel approaches to device hardening may be developed. 3. Procedures for radiation hardness assurance can be developed.

The radiation effects literature is quite extensive. There are many published books that deal with the different types of radiation damage and their effects on the different types of electronic devices. A few of them are listed in the bibliography [1.1- 1.5]. In addition to these books, a major source of radiation effects information is the proceedings of the annual Nuclear and Space Radiation Effects Conference (NSREC) published in the December issues of the IEEE Transaction on Nuclear Science since 1966 (some other months for a few earlier years). It is clearly evident from the above publications that a substantial amount of research has been performed in order to understand the radiation effects in semiconductor devices. Considerable insight into the mechanisms responsible for the radiation effects has been achieved. Many effects are well understood at least qualitatively. However, a large body of this knowledge pertains to Si CMOS and bipolar devices. In comparison, very limited information is available on III-V devices. Radiation effects in GaAs JFETs and MESFETs have been investigated in some detail and they are reviewed by Zuleeg [1.6].

High speed nanoscale (at least in one dimension) heterojunction devices including high electron mobility transistors (HEMTs), heterojunction bipolar transistors (HBTs) and resonant tunneling diodes (RTDs) were developed during the eighties. The high performance of these devices is an attractive feature for their use in lightweight electronic systems for space applications. However, there have been very few reports on the radiation effects in these devices [1.7 - 1.13]. Our research program funded by AFOSR and started in 1996 was aimed at developing a comprehensive understanding of the radiation effects in these modern heterojunction devices. In keeping with the intent of the original BAA, the main focus of our program has been to study the basic mechanisms of radiation effects in these devices with the goal of recommending improvements in device designs. In this report, we summarize the important results and significant achievements of the work performed under this grant.

Research in the radiation response of devices involves two major steps. The first step is to develop an understanding of the interaction of radiation with the materials of interest. The details of such interactions for many types of radiation are well documented for silicon. The basic theories behind these interactions are also well established and they are described in many books. However, at the time when our research program was started, very little was known about the nature of interaction of different types of radiation with the newer materials (e.g. InGaAs, InP, etc.) that are used in the modern heterojunction devices. Hence, a major goal of our research program was to apply the well-known theories of radiation interaction to establish a quantitative understanding of the interaction of radiation in these new materials. This step is essential to correlate the results of the laboratory-based measurements to the response of the devices in the actual radiation environment. The second step in the radiation research is to determine the

physical mechanisms responsible for the observed response of the devices. This step is necessary for developing novel hardening techniques as well as for establishing reliable hardness-assurance procedures. We have carefully addressed the issues related to both these steps in our research program as will be evident from the results described in this report.

Radiation damage in materials may be classified into the following three main categories: (1) Ionizing damage (2) Displacement damage and (3) Single Event Effects. The distribution of damage into the above three categories depends upon the nature of radiation. For example, electromagnetic radiation (γ rays, X rays, etc.) causes primarily ionization damage and only a very small amount of displacement damage. The electrons also cause predominantly ionizing damage accompanied by a non-negligible displacement damage. On the other hand, the damage caused by neutrons is primarily due to displacement damage. Protons can cause all three types of damage.

Ionizing damage is a very important concern in Si CMOS devices. The charges created by the ionization process can be trapped within the oxide as well as at the oxide-silicon interface and in turn can significantly affect the device characteristics. Silicon bipolar devices are affected by both the displacement damage and by the ionization damage. The latter arises from the charges trapped in the passivating oxide layers at the junction boundaries that in turn give rise to surface recombination currents and induced surface channels.

MOS technology is not popular in the case of III-V devices due to the lack of a good oxide (or insulator). The insulating layers are only used as passivating layers and are not integral part of the device action. Hence, the III-V devices are generally found to be extremely hard to total ionizing dose effects. On the other hand, the displacement damage effects and the single event effects can be comparable to that of the Si devices. The main focus of our research program was the investigation of the physical mechanisms responsible for the displacement damage effects in modern III-V heterojunction devices.

We have investigated the following three types of devices in this research program: (1) Heterojunction Bipolar Transistors (2) High Electron Mobility Transistors and (3) Resonant Tunneling Diodes. The following three types of radiation were used in our investigations. (a) Gamma radiation (b) Electron radiation and (c) Neutron radiation. Electrons constitute an important component of the trapped radiation in the earth's magnetic field (Van Allen's belt). Neutron and gamma radiation are encountered in the weapons environment. Neutrons are also generated by the interaction of cosmic rays with earth's atmosphere.

All the radiation services were provided by OSU Radiation Center. A ^{60}Co gamma cell was used for the gamma radiation. A ^{90}Sr beta source was used for the electron radiation. Neutron radiation was derived from OSU TRIGA nuclear reactor.

The combination of the three types of radiation with the three types of devices leads to a number of combinations for possible investigation. Since it is not practical to address all the possible combinations in a single program, we focused our efforts on a few of them. We have carried out a thorough investigation of the response of InP/InGaAs HBTs for all the three types of radiation. We have also investigated the electron irradiation effects in AlGaAs/GaAs HBTs. AlGaAs/GaAs HEMT devices were investigated for electron and neutron radiation effects. AlGaAs/GaAs double barrier resonant tunneling diodes were investigated for electron and gamma irradiation. The different combinations of device types and radiation types investigated in this program are summarized in Table I.

Table I: Combinations of device types and radiation types used in this investigation

Device type	Gamma	Electron	Neutron
InP/InGaAs HBTs	X	X	X
AlGaAs/GaAs HBTs		X	
AlGaAs/GaAs HEMTs		X	X
AlGaAs/GaAs DBRTDs	X	X	

The devices that we used in our investigations fall under three categories based on the level of sophistication. At the top most level we used state-of-the-art devices supplied by our collaborators. We performed only the radiation and characterization. Our work on RTDs falls under this category. The devices were supplied to us by Prof. Sollner, MIT Lincoln laboratories. At the middle level we obtained state-of-the-art device structures grown by our collaborators. We fabricated the devices (including the mask design) and also performed the radiation and characterization. All our work on InP/InGaAs belongs to this category. High quality device structures grown by Metal Organic Chemical Vapor Deposition (MOCVD) were supplied to us by Dr. Andrew Dentai Lucent Technologies, Crawford Hill Laboratory. At the very basic level, we grew our own device structures by molecular beam epitaxy (MBE), fabricated the devices and performed the radiation and characterization. Our work on AlGaAs/GaAs HBTs and AlGaAs/GaAs HEMTs belongs to this category. The quality of the devices under this category was not as good as the ones in the first two cases. However, this level of research provided an excellent opportunity for the training of our graduate students in a variety of skills needed by the industry and defense.

At a microscopic level, radiation damage affects the basic material properties (e.g. carrier lifetime, mobility, etc.). These changes in turn affect the device level parameters at a macroscopic level. Device models are required to relate the experimentally observed degradation of device parameters to the radiation-induced changes in the basic material parameters. We have carried out device modeling at different levels in our effort toward identifying the basic mechanisms responsible for the observed changes in the device parameters. At the top most level we have used commercially available device models (e.g. SPICE) to characterize the device degradation in terms of standard device model parameters. This approach is very simple but appealing since the results of the analysis are very useful for the circuit/system designers in predicting the system response from the degradation of device level parameters. However, this approach does not always work for the modern heterojunction devices since many features specific to the operation of the heterojunction devices are not incorporated in the commercial device models. In such cases, we developed our own SPICE-like device models to characterize the radiation damage of the devices. The disadvantage in these empirical device models is that they do not give much insight into the physical mechanisms. Hence, we also developed sophisticated analytical device models that describe the device characteristics directly in terms of the microscopic material

parameters. Such models have provided very valuable insight into the basic mechanisms responsible for the device degradation.

The results of our investigations have been published in a number of journals including IEEE Trans. Nucl. Sciences, IEEE Trans. Electron Devices, and Microelectronics Reliability. We also reported some of these results in conferences including Nuclear and Space Radiation Effects Conference and International Reliability Symposium. A lot of work described in this report has not yet been published. Our work to date has resulted in one M.S. thesis (Aveek Sarkar, 1998) and one Ph.D. thesis (Alexei Shatalov, defense expected in July 2000). Both these students were supported by this grant. Two more M.S. students (Marc Mims and Babu Nepali - supported by this grant) have nearly completed their dissertations. Another Ph.D. student (Bongim Jun) is currently working on the radiation effects in HEMTs.

The most significant achievements of our investigations are summarized below.

- **Theoretical calculations of radiation interaction**

- We have developed a set of programs for the calculation of ionizing and non-ionizing energy deposition due to gamma, electron and neutron radiation in a few materials of interest (e.g. InP, InGaAs, polyimide, etc.) that are used in modern heterojunction devices. For the purpose of validation of our programs, we also carried out these calculations for silicon and compared them with the results published in the literature.

- **Radiation effects on HEMT basic parameters and devices**

1. Two dimensional electron gas (2-DEG) channel mobility is found to decrease for all the three types of radiation. In all the cases the mobility degradation is due to the displacement damage in the vicinity of the 2-DEG (buffer layer and spacer layer). Magnitude of degradation increases from gamma to electron to neutron radiation.
2. 2 DEG concentration also decreases due to the radiation-induced acceptor-like defects (displacement damage) in the buffer layer.
3. Mobility degradation is smaller for samples protected by a passivating layer of SiO₂.
4. Threshold voltage (V_T) shifts to more positive values due to the decrease of 2-DEG concentration.
5. Device transconductance degrades due to mobility degradation as well as due to the threshold voltage shifts.

- **Radiation effects in HBTs**

The four major degradation effects observed in the case of HBTs are:

1. Current gain degradation due to an increase in the base current. The main component of the base current that increases after irradiation is the B-E junction space charge recombination current. In contrast with the silicon bipolar transistors, the surface component of the base current at the junction peripheries is found to be unaffected by radiation in polyimide passivated compound semiconductor HBTs.
2. Output conductance (or Early voltage) degradation is caused by degradation of B-C junction breakdown voltage and the consequent increase in avalanche multiplication in the B-C junction.
3. Increase in $V_{ce,sat}$ caused by an increase in series resistance.
4. Increase in $V_{ce,offset}$ due to the displacement damage in the B-C junction.

- **Radiation effects in RTDs**

1. No Change in peak current or valley current was observed after gamma irradiation.
2. Peak voltage changes slightly after gamma irradiation. Change in valley voltage is smaller. Change is caused by an increase in series resistance due to contact metal degradation.
3. Electron irradiation produced no change.

The rest of this report is organized as follows. Section 2 describes the basic theoretical aspects of radiation interaction with matter. Calculations of energy deposition for the three types of radiation in the specific materials of interest to the heterojunction devices are described. Experimental results and analysis of the effects of electron, neutron and gamma radiation in InP/InGaAs HBTs are described in Section 3. Electron radiation effects in AlGaAs/GaAs HBTs are described in Section 4. Radiation effects in HEMTs are described in Section 5 while the results on RTD are described in Section 6. Finally, the important conclusions of this work and the directions for future work are presented in Section 7.

List of journal publications resulting from this program

1. A. Bandyopadhyay, S. Subramanian, S. Chandrasekhar, A.G. Dentai, and S.M. Goodnick, "Degradation of DC characteristics of InGaAs/InP single heterojunction bipolar transistors under electron irradiation," *IEEE Trans. Electron Devices*, vol. 46, pp. 840-849, May 1999.
2. A. Bandyopadhyay, S. Subramanian, S. Chandrasekhar, A.G. Dentai, and S.M. Goodnick, "Degradation of InGaAs/InP dingle heterojunction bipolar transistors under electron irradiation," *IEEE Trans. Electron Devices*, vol. 46, pp. 850-858, May 1999.
3. A. Shatalov, S. Subramanian, S. Chandrasekhar, A. Dentai and S. Subramanian, "Electron irradiation effects in polyimide passivated InP/InGaAs single heterojunction bipolar transistors," *IEEE Trans. Nucl. Sci.*, vol. 40, pp. 1570-1577, Dec. 1999.
4. S. Subramanian, A. Sarkar, L. Ungier, and S.M. Goodnick, "Integrity of III-V heterojunction interfaces under gamma irradiation", *IEEE Trans. Nucl. Sci.* 44, pp. 1862-1869, Dec. 1997.
5. A. Sarkar, S. Subramanian, and S.M. Goodnick, "Electron Irradiation Effects in AlGaAs/GaAs Single Heterojunction Bipolar Transistors", To appear in *IEEE Trans. Electron Devices*, 2000.
6. A. Shatalov, S. Subramanian, S. Chandrasekhar, A. Dentai and S. Subramanian, "Neutron irradiation effects in InP/InGaAs single heterojunction bipolar transistors," Accepted for presentation in Nuclear and Space Radiation Effects Conference, Reno, 2000., and subsequently to be published in *IEEE Trans, Nucl. Sci.* Dec., 2000.
7. A. Shatalov, S. Subramanian, A. Dentai, S. Chandrasekhar and S.M. Goodnick, "Neutron-radiation-induced shift in the offset voltage of InP/InGaAs single heterojunction bipolar transistors" To appear in *J. Appl. Phys.*, 2000.

List of M.S. and Ph.D. theses resulting from this program

1. A. Sarkar, "Radiation effects in compound semiconductor heterostructure devices," M.S. Dissertation, Oregon State University, Corvallis, OR, August 1998.
2. Alexei Shatalov, "Radiation Effects in InP/InGaAs Herojunction Bipolar Transistors", Ph.D. Thesis, Oregon State University, 2000.
3. M. Mims, "Electron Irradiation Effects in AlGaAs/GaAs High Electron Mobility Transistor", M.S. Thesis, Oregon State University, 2000.

SECTION 2

Interaction of Radiation with Materials

Semiconductor devices are often used in systems that operate in a wide variety of ambient conditions. While some applications offer clean mild environments, others expose these systems to different levels of stress including radiation. Military and commercial space satellites are constantly exposed to radiation present in the natural space environment. High-energy electrons (few MeV) and protons (few hundred MeV) trapped in the magnetic field of the earth, cosmic rays (nuclei with energies up to few ZeV), solar particles and cascades of gamma photons and neutrons are the typical radiation hazards present in the space. Relative and absolute magnitude of the fluxes and energies of different particles typically vary with altitude and position. But even at the lower end, the orbits of the manned spacecraft missions pose potentially dangerous radiation levels. Other radiation environments include military applications where significant exposures to neutron and gamma radiation are expected, semiconductor manufacturing (ions, betas and x-rays) and medicine (gamma rays, x-rays, electrons and neutrons).

Energetic particles and photons present in the natural space and other radiation environments can create significant damage in semiconductor materials and devices by displacing atoms and/or by generating charges in the material. Based on the nature of damage created by radiation effects they are usually divided into three primary groups. (1) Displacement damage effects (DDE) resulting from the dislodging of the atoms from their normal sites in a crystal lattice that affect mostly the bulk properties of the materials. (2) Total dose effects (TDE) are those which result from the charge and charge center generation by ionizing radiation. These effects are responsible for degradation of devices in MOS technologies. (3) Finally, there are single event effects (SEE) resulting from the interactions with a single or a burst of high energy particles passing through the device. For example, an energetic heavy ion can produce displacement spikes and/or induce the so-called ionization channels up to a few microns in diameter. The channels can cause significant current and/or voltage transients which may change the state of a circuit or even result in permanent damage.

As the incident particle traverses a solid, it interacts with material atoms and loses its kinetic energy to atomic electrons and/or atoms. The probability of these processes is determined by the corresponding reaction cross sections and can be estimated. The situation, however, is much more complicated as one has to account for all the created secondary particles (electrons and atoms) which in turn can introduce further damage. In contrast to the secondary electrons, which, as a rule, do not have enough energy to cause further atomic displacements, primary knock-on atoms (PKAs) can sometime induce collision cascades and sub-cascades, resulting in considerable ionizing and displacement damage. Furthermore, in the case of so-called 'nonionizing' radiation such as neutrons, almost all the damage is created by PKAs and their secondary particles.

The first successful analytical theory addressing the problem of the division of the PKA dissipated energy between the ionizing and displacement damage effects was developed by Lindhard et al. [2.1]. They formulated integral equations describing the process of PKA slowing down in an arbitrary medium. Knowing the details of PKA's interaction with electrons of the media and the inter-atomic potentials these equations can be solved numerically. The solution of the Lindhard's integral equation provides us with an expression for the dimensionless kinetic energy, $L(\epsilon)$, transferred to the atoms by a PKA of initial dimensionless energy ϵ . $L(\epsilon)$ is also

called Lindhard partition function. Clearly, $L(\epsilon)/\epsilon$ gives the fraction of PKA energy available for dislodging atoms. An example of the normalized $L(\epsilon)/\epsilon$ for bulk gallium is shown in Fig. 2.1. One of the quantities of our interest is the number of atoms displaced in a collision cascade. There are

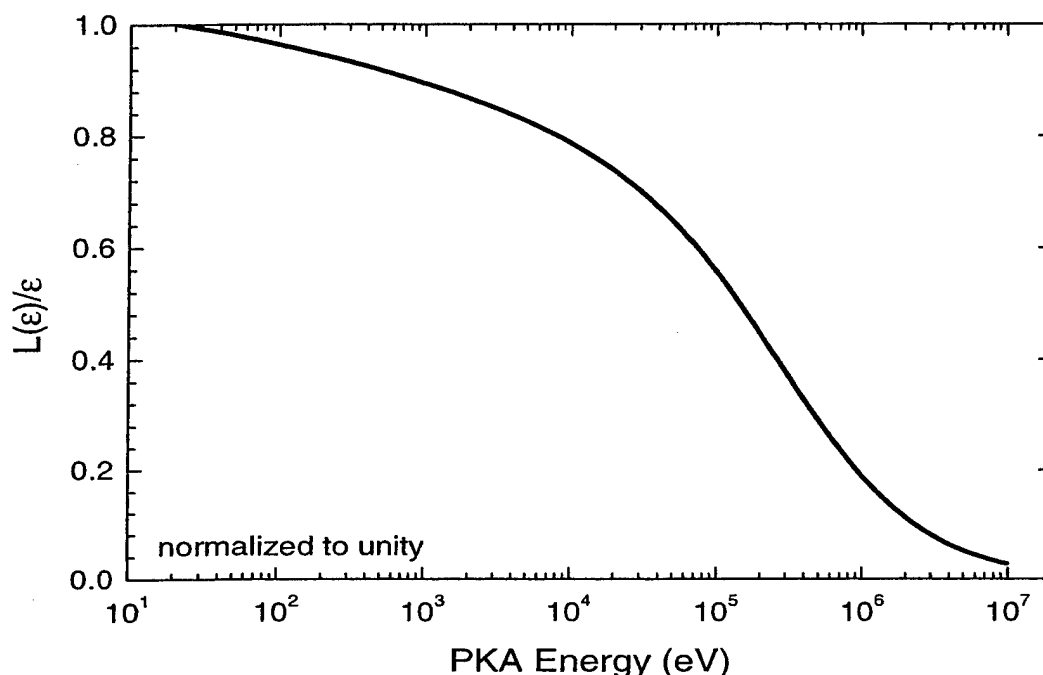


Fig. 2.1 Normalized Lindhard partition function for gallium

several different approaches [2.2] to the problem of calculating the number of the displacements, ranging from simple Kinchin-Pease analytical equations to very complex computer-time-consuming molecular dynamics simulations. Norgett et al. [2.3] proposed relatively successful model based on the modified Kinchin-Pease formula and the Lindhard's energy partition theory. According to them the number of displacements produced by one PKA is

$$N_d(T) = \frac{\kappa L(\epsilon)}{\epsilon} \frac{T}{2E_d} \quad (2.1)$$

where $\kappa=0.8$ is the displacement efficiency and E_d is displacement threshold energy for a given atom in the material. There is some uncertainty in the values of E_d as different theoretical and experimental methods give different estimates. Sometimes E_d is even used as an empirical parameter to fit the theory to the measured results. The displacement energy values listed in Table 2.1 are the ones most commonly used by the radiation-hardness community and therefore will be used in this work.

Table 2.1. Displacement threshold energies in different semiconductor materials

Atom	Matrix	E_d (eV)
Si	Si	21
Ga	GaAs	10
As	GaAs	10
In	InP	6.7
P	InP	8.7

2.1 Interaction of Electron Radiation with Matter

In this section we briefly describe the theory of electron irradiation effects in semiconductor materials. First, we discuss the interactions of electrons with matter and the methods for the calculation of the stopping powers, ranges and absorbed doses. Then we consider the production of atomic displacements and calculate the non-ionizing energy loss (NIEL) and displacement dose.

Energetic electrons passing through a solid interact with atoms and electrons of the medium leading to a wide variety of physical processes. At relatively high energies (>few hundred MeV) the electrons are slowed down by the emission of Cherenkov radiation, and through nuclear reactions. At lower energies, however, the interaction cross sections for these reactions drop significantly and the so-called electronic and nuclear slowing down become more dominant. *Bremsstrahlung* plays some role at very low energies, typically few hundred eV and lower. As we are interested in the energy range $E < 1.5$ MeV in our present experiments, only the last three mechanisms will be considered in some detail. It is customary to separate the total stopping power into three components, corresponding to electron collision, nuclear collision, and radiative stopping, S_{ce} , S_{cn} and S_r , respectively.

$$S = S_{ce} + S_{cn} + S_r \quad (2.2)$$

In the following sections these individual stopping mechanisms will be considered in detail.

2.1.1 Electron Collision Stopping

Inelastic Coulomb collision with bound atomic electrons is the most effective slowing down mechanism for incident electrons for energies less than a few MeV. The mass collision stopping power can be written as [2.4]

$$S_{ce} = n_a \rho Z \int_0^{E_{\max}} E \frac{d\sigma}{dE} dE \quad (2.3)$$

where n_a is the atomic density measured in atoms/cm³, Z is the atomic number, E_{\max} is the largest possible energy transfer, and $d\sigma/dE$ is the differential cross section for the transfer of energy E from the incident electron to an atomic electron. For mixtures of elements the effective atomic number, Z_{eff} is used in place of Z .

The original theory for calculating Eq. 2.3 was developed by Bethe and Bloch [2.5] and is based on the classical approach and does not take into account quantum mechanical aspects of the problem. More sophisticated Moller's approach includes relativistic, spin and exchange effects and is the one most commonly used nowadays. Calculated electron mass-collision stopping powers in Si, InP, InGaAs, Au and polyimide are shown in Fig. 2.2.

2.1.2 Radiative Stopping Power

The radiative stopping power is calculated from electromagnetic and relativistic theory as given by Berger [2.6]. Calculated radiative electron stopping powers in Si, InP, InGaAs, Au and polyimide are shown in Fig 2.3. Below 10 MeV, the radiative stopping powers are considerably

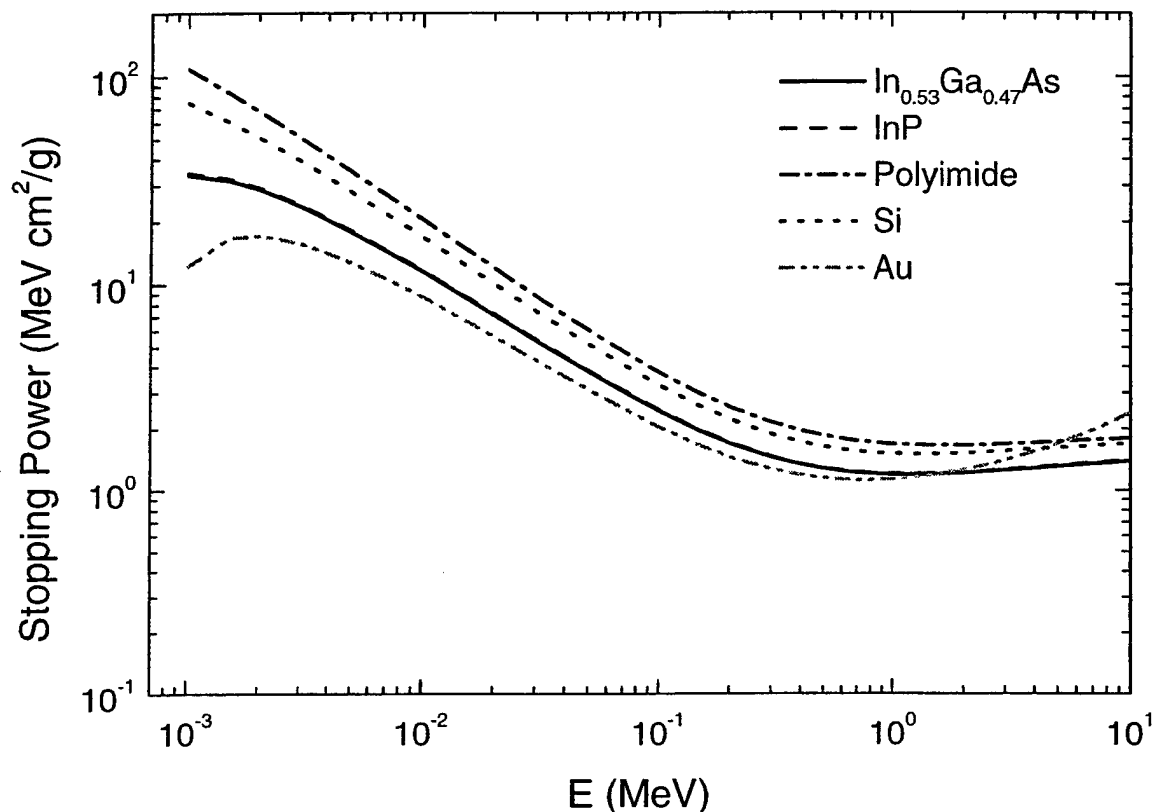


Fig. 2.2 Calculated electron mass-collision stopping powers in Si, InP, InGaAs, Au and polyimide

less than the electron collision stopping powers and can be safely neglected except for very low energies. At low energies, on the order of few tens eV, the incident electrons can not participate in inelastic scattering by atomic electrons, as their energy is not sufficient to excite/ionize atoms of the medium. In this case the *bremsstrahlung* emission, also called radiative stopping, becomes dominant slowing-down mechanism.

2.1.3 CSDA Range and Ionizing Energy Deposition

As electron traverses material it continuously interacts with atomic electrons, nuclei and atom as a whole. As a result of these inelastic and elastic scattering events the incident electron slows down by losing its energy to electrons and nuclei in the host material. This is a statistical process and hence there is a distribution of possible energy losses for each collision. It is, however, a relatively good approximation to neglect the energy loss fluctuations and assume that the electron loses its energy according to the mean energy loss per unit path length given by the stopping power. In this so-called continuously slowing down approximation (CSDA) the range for an electron of initial energy T_0 slowing down to rest is given by

$$R_{CSDA} = \int_0^{T_0} \left(\frac{dT}{\rho dx} \right)^{-1} dT \quad (2.4)$$

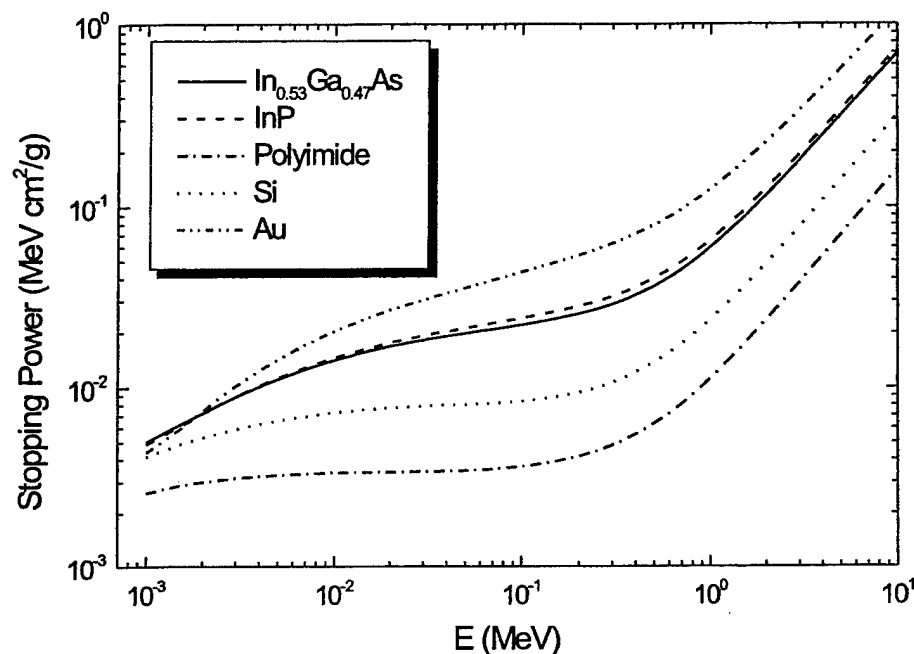


Fig. 2.3 Calculated radiative electron stopping powers in Si, InP, InGaAs, Au and polyimide

Calculated CSDA ranges in Si, InP, InGaAs, Au and polyimide are shown in Fig. 2.4. Using the CSDA ranges, the mass stopping powers and the thickness of the active layers in a typical HBT device, the slowing down of electrons in the active volume of our devices is found to be very small. Hence, the total dose deposited in the device volume by a monoenergetic beam of characteristic energy E and fluence $\psi(E)$ is easily calculated from the electron-collision mass stopping power $S_{ce}(E)$ shown in Fig. 2.2 by using the relation

$$D(E) = \psi(E) S_{ce}(E) \text{ MeV/g} \quad (2.5)$$

Note that the radiative and nuclear collision stopping powers are neglected and only the electron collision stopping power is used. This approximation does not introduce any significant error for the energy range of the interest (~ 1 MeV). Converting units from MeV/g to conventional *rads* one obtains

$$D(E) = 1.6 \times 10^{-8} \psi(E) S_{ce}(E) \text{ rads} \quad (2.6)$$

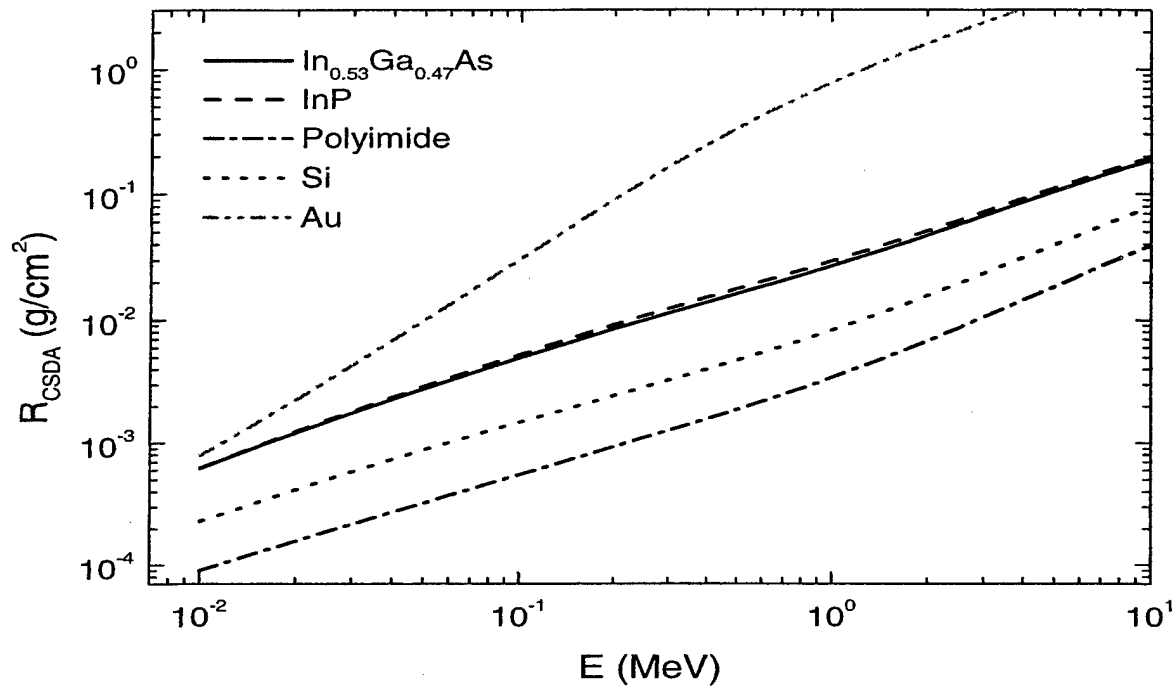


Fig. 2.4 Calculated CSDA ranges in Si, InP, InGaAs, Au and polyimide

In the case of a continuous electron energy distribution the energy spectrum of the electrons should be combined with the energy dependence of the stopping power

$$D = 1.6 \times 10^{-8} \int_0^{E_{\max}} \frac{d\psi(E)}{dE} S_{ce}(E) dE \text{ rads} \quad (2.7)$$

It is clear, of course, that this equation is the exact expression for the total ionizing dose (TID) which is very close to the total absorbed dose for the beta radiation of the given energy range. Fig. 2.5 shows depth profile of TID rate for electrons of initial energy 1-MeV (mean energy of β -rays emitted by $^{90}\text{Sr}/^{90}\text{Y}$ source) in a thick layer of silicon. Keeping in mind that the typical total thickness of the studied devices is about 1-2 μm it must be concluded that the absorbed energy is almost the same in all regions of the device. Therefore all subsequent calculations will be performed for monoenergetic electrons of 1 MeV.

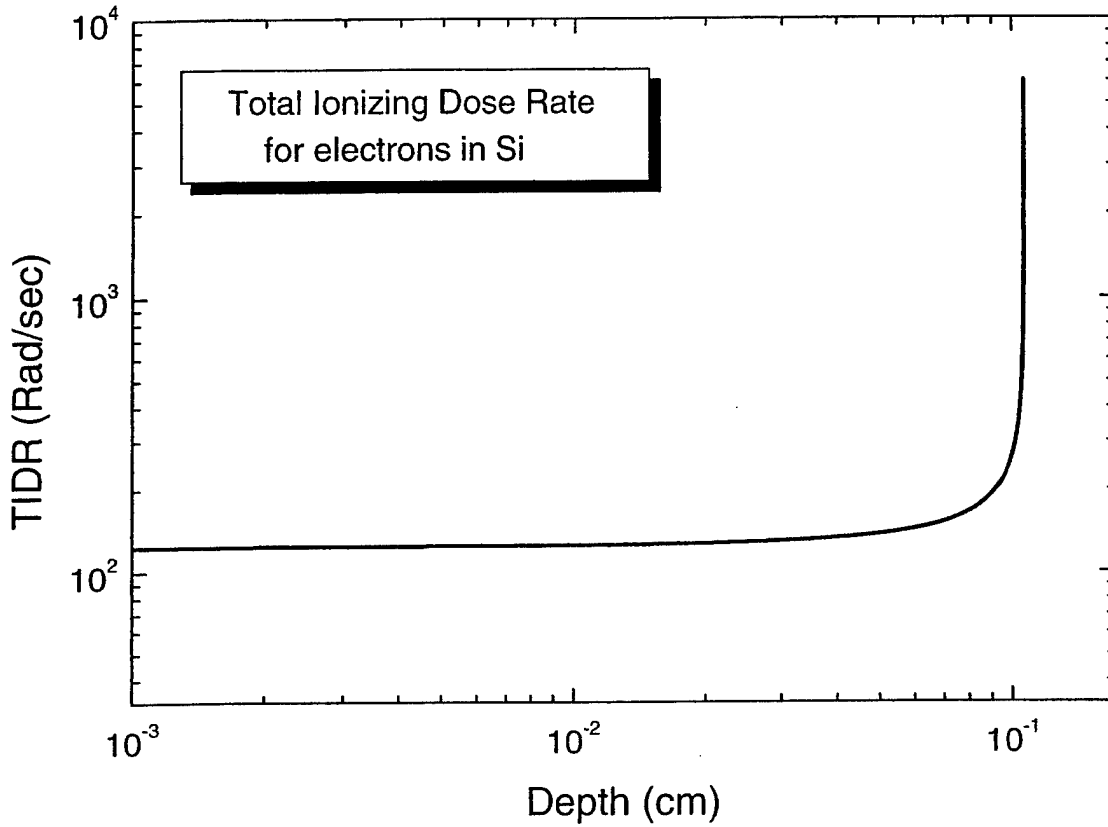


Fig. 2.5 Total ionizing dose rate for 1 MeV electrons in a thick layer of silicon

2.1.5 Displacement damage and Non-ionizing energy loss (NIEL)

Calculation of NIEL, S_d , for electrons consists of evaluation of the following integral [2.7]

$$S_d = \frac{N_A}{A} \int_0^\pi L[T(\Theta)] T\{\Theta\} \frac{d\sigma(\Theta)}{d\Omega} d\Omega \quad (2.8)$$

where $T(\theta)$ is the energy transferred to the recoiling nucleus by an electron scattered elastically at an angle θ , $L[T(\theta)]$ is the corresponding Lindhard partition function and $d\sigma/d\Omega$ is the Mott cross-section [2.8] for the elastic scattering event. Calculated NIEL for electrons in Si, GaAs, InGaAs and InP are shown in Fig. 2.6. The displacement dose D_d is calculated from the following equation.

$$D_d = 1.6 \times 10^{-8} \int_0^{E_{\max}} S_d(E) \frac{d\psi(E)}{dE} dE. \quad (2.9)$$

In the simplest case when the electron fluence is monoenergetic, the above equation reduces to

$$D_d = 1.6 \times 10^{-8} S_d(E) \psi(E). \quad (2.10)$$

The density of displacement defects introduced by a fluence of electrons is given by

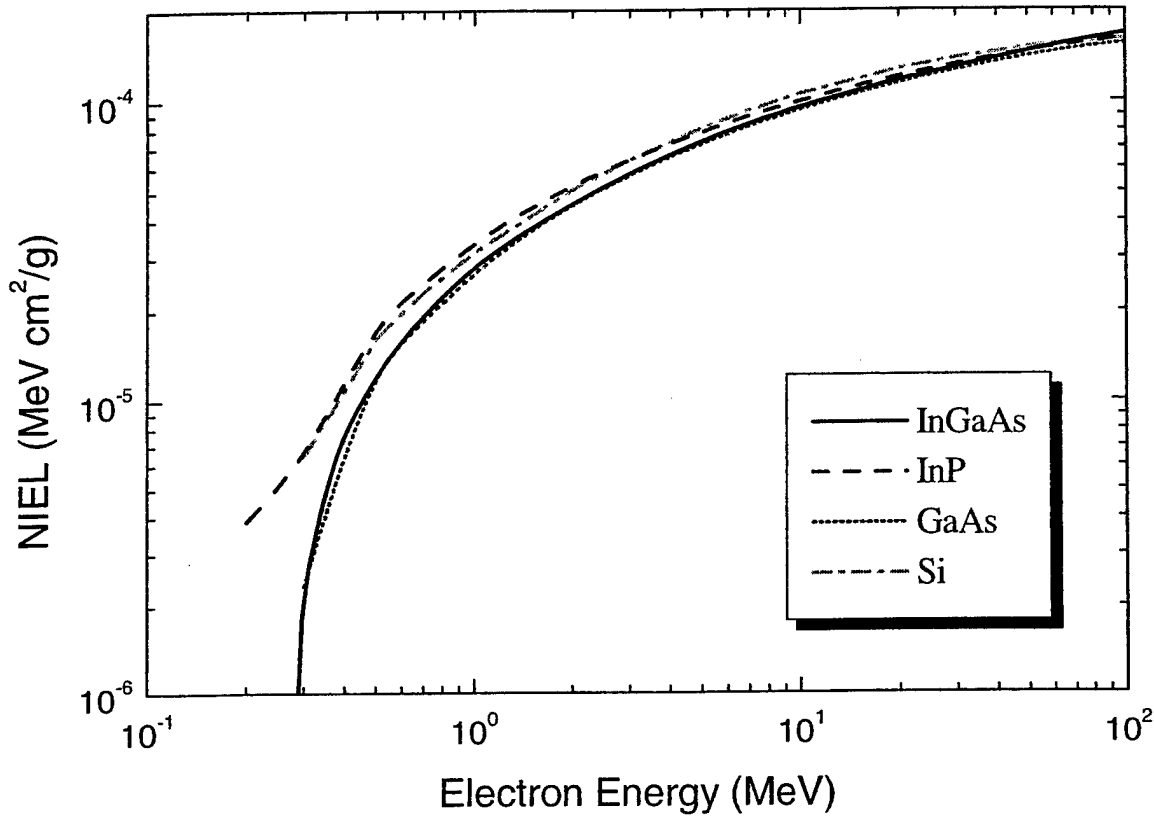


Fig. 2.6 Calculated NIEL for electrons in Si, GaAs, InGaAs and InP

$$N_d = n_a \int_0^{E_{\max}} dE \int_0^{\pi} \frac{L[E_a(E, \theta)]}{\epsilon} \frac{\kappa E_a(E, \theta)}{2E_d} \frac{d\psi}{dE} \frac{d\sigma(E, \theta)}{d\Omega} d\Omega \quad (2.11)$$

where we have made use of Lindhard's partition function and modified Kinchin-Pease equation for the calculation of number of displacements. In the equation above $E_a(E, \theta)$ is the energy of the recoil atom in an elastic scattering event in which the electron is scattered through an angle θ , and is given by

$$E_a(E, \theta) = \frac{2E(E + 2m_0c^2)}{M_0c^2} \sin^2(\theta/2) \quad (2.12)$$

where m_0 and M_0 are the rest masses of electron and the recoil atom, respectively.

At this point, we define two useful quantities, the defect introduction rate per unit fluence, a_T and the defect introduction rate per unit ionizing dose deposited in the material, A_T , which are defined by the following equations.

$$N_d = a_T \Psi = A_T D \quad (2.13)$$

where Ψ is the electron fluence and D is the absorbed ionizing dose. The calculated values of a_T and A_T in Si, GaAs, InGaAs and InP for 1 MeV electrons are listed in Table 2.2. Using the experimentally measured values of Ψ or D and using the calculated values of a_T or A_T , the expected defect density can be easily calculated.

Table 2.2 Displacement damage introduction rate for 1 MeV electrons per unit electron flux, per unit ionizing dose, 1 Rad(Si) and non-ionizing energy loss in different materials.

Material	a_T (cm ⁻¹)	S_d (eVcm ² /gm)	A_T (Rad ⁻¹ (Si)cm ⁻³)
Si	1.4	31.4	0.6×10^8
GaAs	5.6	26.5	2.3×10^8
InGaAs	6.2	28.5	2.6×10^8
InP	7.4	33.5	3.1×10^8

2.2 Interaction of Neutron Radiation with Matter

The production of atomic displacements by neutron irradiation occurs mainly through two different mechanisms: (1) nuclear reactions, the products of which can cause atomic displacements, and (2) by direct energy transfer through elastic or inelastic scattering. In both cases, the displacement is produced if the recoiling nucleus has an energy in excess of the displacement threshold, E_d . The recoil can have enough energy to produce further displacements before coming to rest in the lattice. The PKA energy deposition is described by the Lindhard's partition theory.

First we calculated the partial displacement kerma (also called damage energy production cross section) for In, P, Ga, Si and As. Then, using the results of the calculations for the separate elements, we calculated the total displacement kerma for InP and InGaAs compounds. For In, P, Ga and Si the ENDF/B-VI library available from T-2 Nuclear Information Service of Los Alamos National Laboratories was used. Unfortunately the ENDF/B-VI library data does not provide adequate data for As, in which case the ENDL82 library available from the Radiation Safety Information Computational Center was employed. The calculated displacement kermas for InP and InGaAs are shown in Fig. 2.7 and 2.8, respectively.

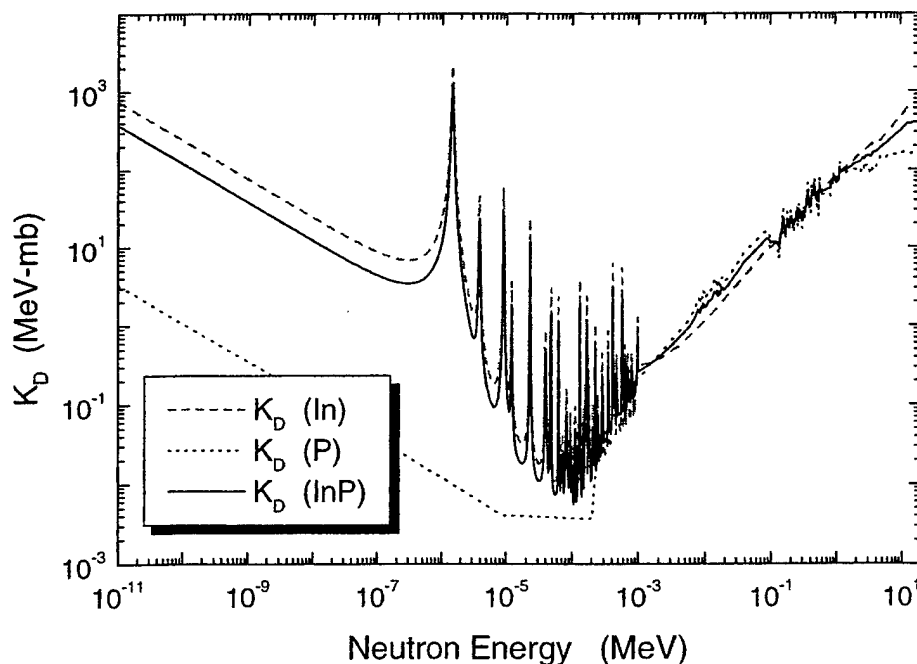


Fig. 2.7 Calculated neutron displacement kerma in In, P, and InP

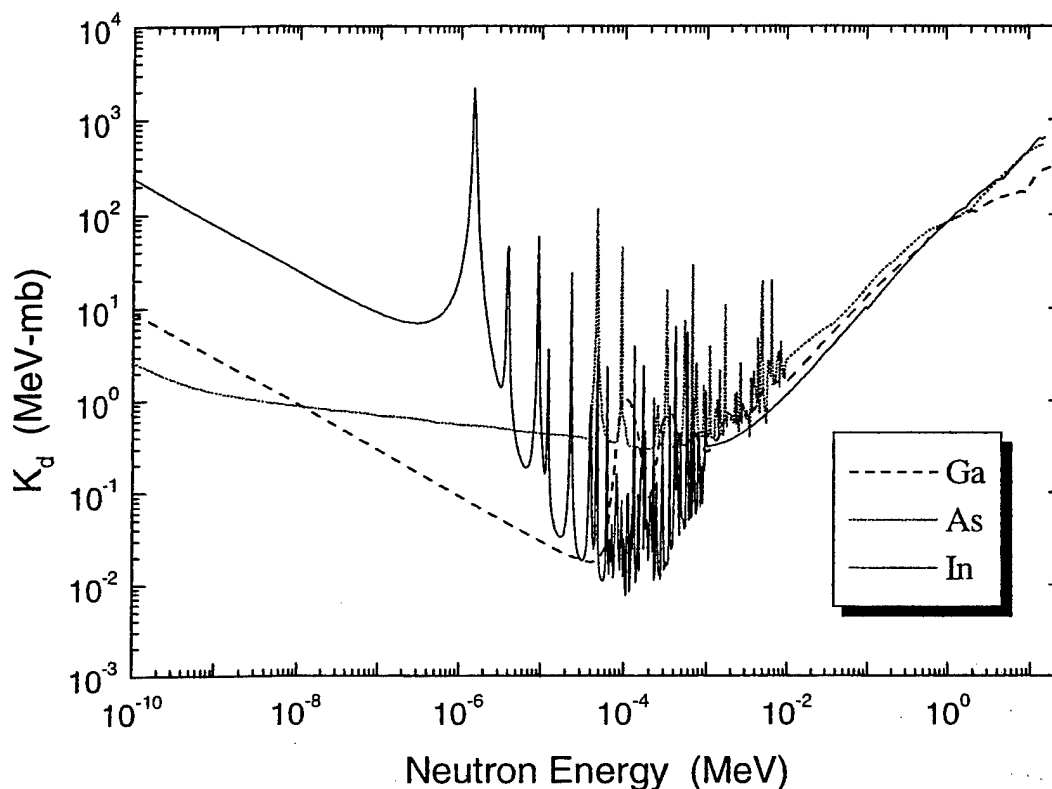


Fig. 2.8 Calculated neutron displacement kerma in InGaAs

2.2.1 Neutron Damage Equivalence and NIEL

All neutron irradiation experiments were performed using OSU TRIGA "Marc II" 1 MW reactor operated at 100 kW. The samples were enclosed in cadmium boxes to block the thermal neutrons ($E_{th} < 0.5$ eV) and reduce ionization damage. For the irradiation the samples were positioned in the Rotating Specimen Rack (RSR), also called "Lazy Suzan". Differential neutron energy spectrum at the RSR -- result of the Monte Carlo Neutron Photon (MCNP) transport simulation -- is shown in Fig. 2.9. Furthermore, the total epi-thermal and fast neutron fluxes were measured using foil activation dosimetry technique, with results of 10^{10} cm $^{-2}$ and 5×10^{10} cm $^{-2}$ for epi-thermal ($0.5\text{-eV} < E < 10$ keV) and fast neutron ($E > 10$ keV) fluxes, respectively, for the reactor operated at 100 kW. The integrated flux for the fast neutron part of the MCNP calculated spectrum was normalized to one and then multiplied by the fast neutron flux value obtained from the direct measurement. In other words, the MCNP results were used only to obtain the shape of the spectrum, while the absolute values of the flux were determined from the dosimetry measurements. Similar procedure was used for the analysis of the epi-thermal neutron flux.

Energy spectra of a neutron flux produced by an accelerator or nuclear reactor may vary drastically from one facility to another. To be able to interpret and compare the results of irradiation by sources of different energy spectra the so-called 'equivalent monoenergetic neutron fluence' is often used. The method relies on the knowledge of the energy spectrum of the neutron source and the degradation effects as a function of energy. Using 1 MeV (standard value used by the radiation-hardness community) as a reference energy, the equivalent monoenergetic neutron flux can be calculated as

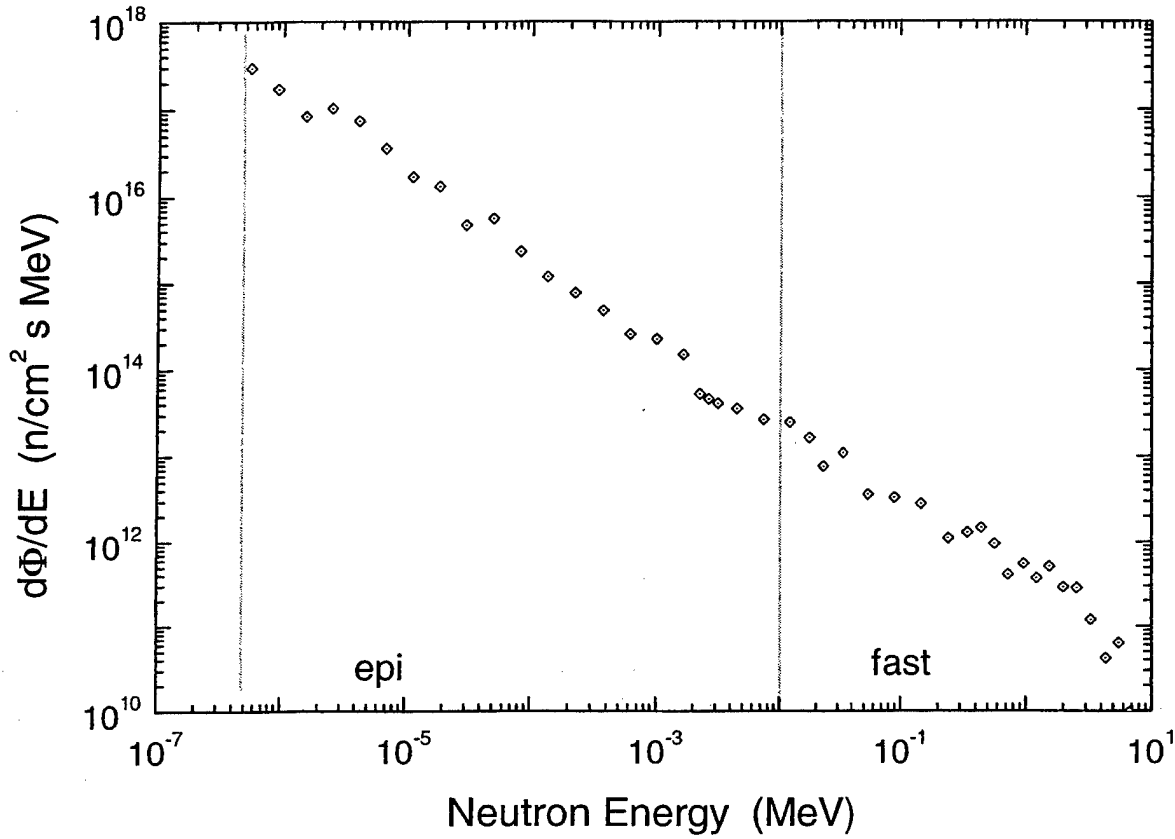


Fig. 2.9 "Lazy Suzan" neutron energy spectrum

$$\phi_{eq,1MeV} = \int_0^{\infty} \frac{d\phi(E)}{dE} \frac{F_D(E)}{F_D(1MeV)} dE \quad (2.14)$$

It should be noted that the damage function is different for different semiconductors and therefore $\phi_{eq,1MeV}$ should be calculated separately for each material of interest. Using the calculated displacement kerma for InP and InGaAs (see Figs. 2.7 and 2.8) and Lazy Suzan energy spectrum the integral is evaluated in the range of 0.5 eV-10 MeV.

Although the displacement kerma can be used as a direct measure of the damage energy deposited in the material, it is more convenient to perform some unit conversion and present the results in terms of the non-ionizing energy loss. Recalling that the units for NIEL is MeVcm²/gm, the conversion equation is

$$S_d = 10^{-27} \frac{K_D n_a}{\rho} [MeVcm] \quad (2.15)$$

The calculated values of NIEL at 1MeV neutron energy for Si, GaAs, InGaAs and InP are listed in Table 2.3. Displacement introduction rate can be simply calculated from the NIEL results using the modified Kinchin-Pease model and these results are also included in Table 2.3.

Table 2.3 Displacement kerma, neutron NIEL and damage introduction rate for 1MeV neutrons in Si, GaAs, InGaAs and InP.

Material	K_D MeV mb	S_d MeV cm ² /gm	α_T cm ⁻¹
Si	95	2.04×10^{-3}	90
GaAs	70	0.64×10^{-3}	136
InGaAs	82	0.58×10^{-3}	127
InP	78	0.64×10^{-3}	141

2.3 Interaction of Gamma radiation with matter

Photons have zero rest mass and are electrically neutral. They interact with target atoms through photoelectric effect, Compton scattering, and pair production. In all three cases, the interaction produces energetic free electrons. The energy range in which photoelectric effect dominates depends on the atomic number Z of the target material. The probability of a photoelectric interaction decreases with increasing photon energy and decreases with the atomic number Z . The incident photon energy is completely absorbed by the target atom. The difference between the photon energy and the binding energy of the electron ejected by the photon (photoelectron) is carried by the photoelectron as kinetic energy.

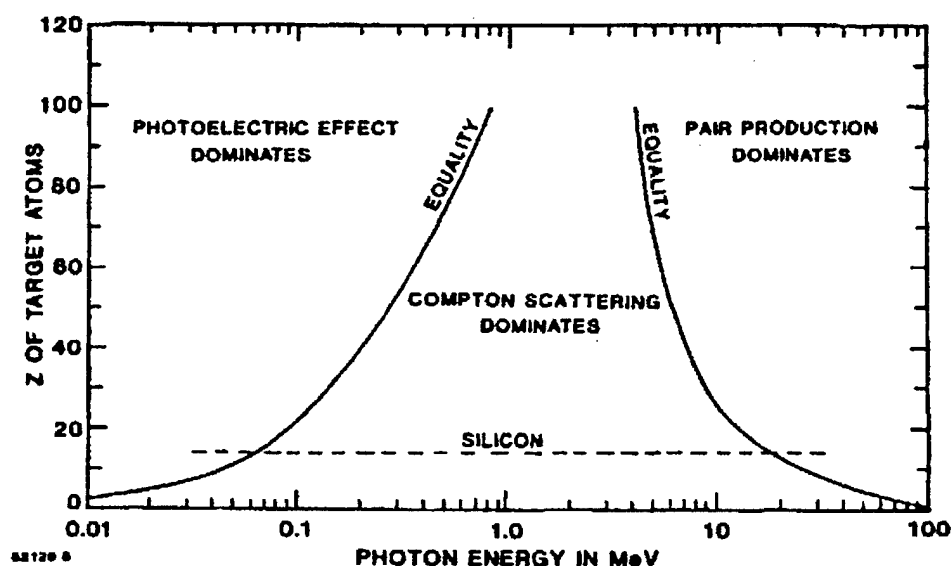


Fig. 2.10 Relative importance of the three photon processes as a function of photon energy and the atomic number (Z) of the target atom.

In contrast to the photoelectric effect, Compton scattering does not involve complete absorption of the incident photon energy. Instead, the incident photon gives up a part of its energy to scatter an atomic electron and the lower energy scattered photon continues to travel in the target material. The electron released from the atom by this process is called the Compton electron. The third type of photon interaction with matter is called pair production in which the incident photon is completely absorbed by the target atom and an electron-positron pair is produced. The threshold energy for this process is quite high (> 1.0 MeV) and it increases with

decreasing Z . The relative importance of the three photon interactions as a function of photon energy and the atomic number of the target atom is shown in Fig. 2.10. The solid lines correspond to equal interaction cross sections for the overlapping effects. For silicon, the photoelectric effect dominates at energies < 50 keV and pair production at energies > 20 MeV. Thus, over a wide, intervening photon energy range, Compton scattering dominates and the subsequent energy deposition takes place through the interaction of the Compton electrons with the target atoms. We now discuss briefly the basics of the Compton scattering and photoelectric effect and the physics necessary to evaluate their contributions to the damage production.

Compton Effect

In a Compton scattering event, the incident photon of energy $h\nu$ loses part of its energy T_e to the Compton electron scattered at an angle θ . The photon is scattered through an angle ϕ and emerges with an energy $h\nu' = h\nu - T_e$. Depending upon θ , the kicked electron can have any value of energy lying between 0 and $T_{e,max}$ given by

$$T_{e,max} = \frac{2h\nu\alpha}{1+2\alpha}$$

where $\alpha = h\nu/m_e c^2$, and the electron binding energy is assumed to be negligible. For further

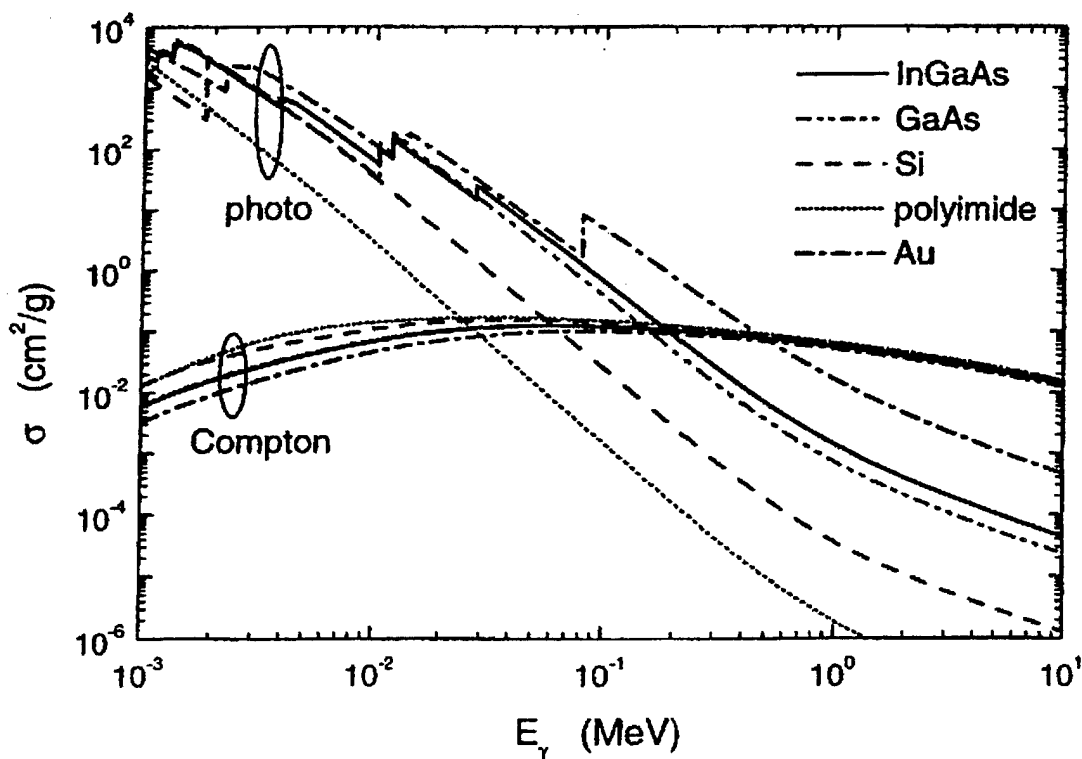


Fig. 2.11 Compton scattering cross-section and photoelectric cross-section as a function of photon energy in selected materials.

analysis, the differential cross section for the photon scattering needs to be evaluated. Using Dirac's relativistic theory, Klein and Nishima have derived fairly accurate differential cross sections for the scattering process. The KN theory, however, was derived for free electrons. Sufficiently good results for scattering by bound inner shell electrons are achieved simply by multiplying the KN cross sections by the Hartree-Fock incoherent scattering functions available through XCOM data base [2.9]. Calculated cross sections for Compton scattering are shown in Fig. 2.11 for Si, GaAs, InGaAs, Au and polyimide. The values of cross sections at $E_\gamma = 1.25$ MeV are listed in Table 2.4. The corresponding flux of Compton electrons per incident photon is also listed in Table 2.4. For comparison, the photoelectric effect cross sections calculated by Berger et al [2.10] are also shown in Fig. 2.11 and the values for 1.25 MeV photons are listed in Table 2.4. It should be noted that the photoelectric effect cross sections are much lower than that for Compton effect except for high Z elements such as Au. Hence, in our further analysis we use only the Compton electrons for the damage calculations.

Spectrum Resulting from Electron Slowing Down

The electron spectrum incident on some layer in the device may not necessarily coincide with the initial photon-generated spectrum since electrons get slowed down along their path to the region of interest. As discussed in Section II, the high energy electrons dissipate their energy through a series of collisions. In the vast majority of collisions an electron loses only a very small fraction of its energy, and the probability of the large energy losses due to radiative or knock-on events is usually low. Under these conditions the spectrum resulting from the slowing down process is simply inversely proportional to the total electron stopping power in the medium (see for example). Applying this rule to the Compton electrons introduced by the gamma radiation, the energy spectrum of the slowed down electrons can be evaluated as

$$\phi(T_e) = \left[\frac{dT_e}{dx}(T_e) \right]^{-1} T_e \int_{T_e}^{T_{e,\max}} N(T_e') dT_e'$$

where $N(T_e')$ is the number of electrons generated in a unit volume per photon per unit time. Calculated slowed down spectra for Si, GaAs, InGaAs and InP are shown in Fig. 2.12. Finally, the total electron flux is calculated by integrating slowed down differential electron flux and the results are also included in Table 2.4.

Table 2.4 Cross sections for Compton scattering (σ_c) and photoelectric effect (σ_{pe}), primary Compton electron flux and total slowed down flux produced by one incident gamma photon of energy 1.25 MeV in different materials.

Material	σ_c (1.25MeV) (cm ² /g)	σ_{pe} (1.25MeV) (cm ² /g)	Φ_c (cm ⁻²)	Φ_{slowed} (cm ⁻²)
Si	0.058	2.33×10^{-5}	0.119	0.016
Au	0.056	1.04×10^{-2}	0.021	0.023
GaAs	0.051	4.63×10^{-4}	0.064	0.017
InP	0.052	1.62×10^{-3}	0.072	0.018
InGaAs	0.051	8.94×10^{-4}	0.064	0.018
Polyimide	0.058	1.24×10^{-6}	0.168	0.014

Non ionizing energy loss and Displacement dose

Once the slowed-down electron spectrum is calculated, the non-ionizing energy loss and the displacement dose can be calculated using the techniques already discussed for electrons in section 2.1. Calculated non-ionizing energy loss and displacement dose deposited by one 1.25

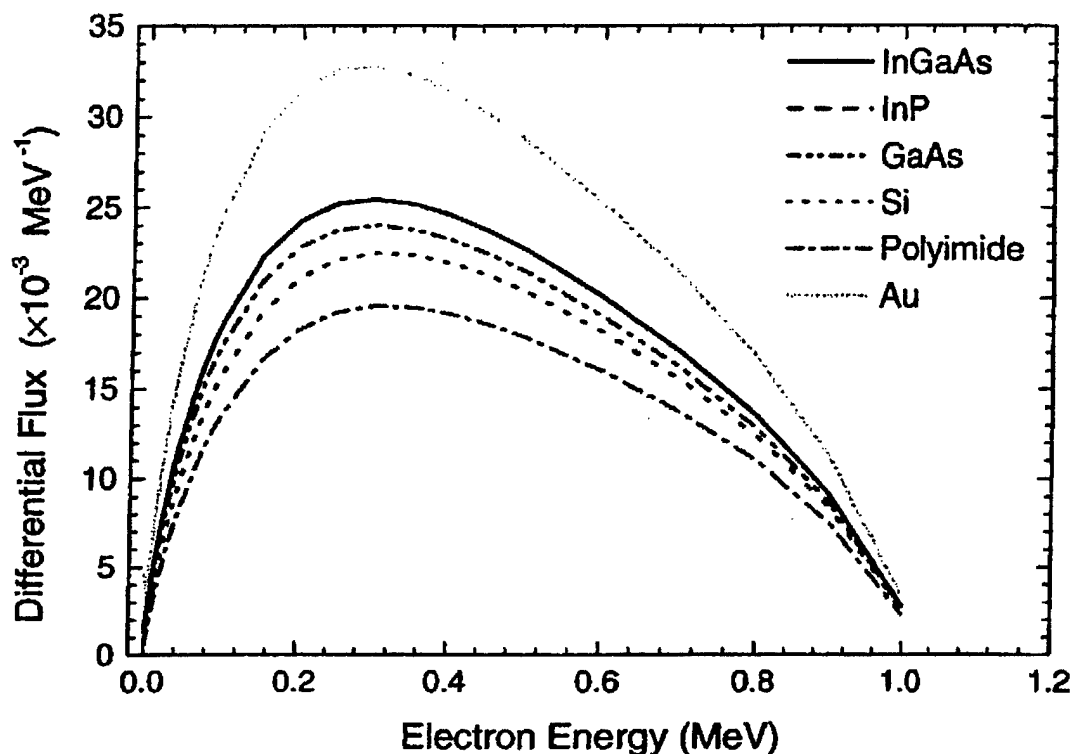


Fig. 2.12 Calculated slowed down electron spectra produced by a single 1.24 MeV photon in selected materials.

MeV photon in Si, GaAs, InGaAs and InP are listed in Table 2.5. It is convenient at this stage to introduce the concept of equivalent 1 MeV electron fluence. It is defined as the 1MeV electron fluence that produces the same damage effect as the actual photon fluence. The calculated equivalent 1MeV electron fluences, Ψ_{equiv} produced by 1Mrad(Si) 1.25 MeV gamma photon flux in Si, GaAs, InGaAs and InP are listed in Table xx. The number of displacements for 1 Mrad(Si) is calculated from

$$N = \kappa \frac{S_{niel}(1MeV)}{2E_d} \rho \Psi_{equiv}$$

The calculated number of displacements for 1 Mrad(Si) in different materials are also listed in Table 2.5.

Table 2.5 Non-ionizing energy loss, displacement dose, equivalent 1MeV electron fluence and number of displacements for 1 Mrad(Si) of 1.25 MeV gamma radiation in different materials.

Material	S_d^γ (MeV cm ² /g)	D_d^γ (rad)	$\Psi_{1MeV, equiv}$ (10 ¹³ cm ⁻²)	A_T (10 ⁷ rad(Si) ⁻¹ cm ⁻³)
Si	1.83x10 ⁻⁷	2.93x10 ⁻¹⁵	1.1	1.5
GaAs	1.42x10 ⁻⁷	2.27x10 ⁻¹⁵	1.0	5.6
InP	2.28x10 ⁻⁷	2.27x10 ⁻¹⁵	1.2	9.7
InGaAs	2.28x10 ⁻⁷	2.27x10 ⁻¹⁵	1.0	5.8

SECTION 3

Radiation Effects in InP/InGaAs Heterojunction Bipolar Transistors

In this section we present our experimental results, analysis and discussion of radiation effects in InP/InGaAs heterojunction bipolar transistors (HBTs). We have investigated the radiation effects in these devices caused by all three types of radiation including electrons, neutrons and gamma rays. In the case of electron irradiation we have also made a comparison between the performance degradation of unpassivated devices and passivated devices and between single heterojunction devices (SHBTs) and double heterojunction devices (DHBTs). First, we present in Section 3.1 our experimental results of electron irradiation effects in unpassivated SHBTs and DHBTs. The results of this section are analyzed by using a SPICE-like device model developed by us. We then present experimental results of electron irradiation effects in polyimide passivated SHBTs in Section 3.2. These results are again analyzed by using our custom SPICE device model. In Section 3.3, we present our results of neutron irradiation effects in passivated SHBTs. Different results of this section are analyzed by different models including commercial SPICE model, our own SPICE model and an analytical model. Finally, in section 3.4, we present our experimental results on gamma irradiation effects in SHBTs. The results of this section are analyzed only qualitatively.

3.1. Electron Irradiation effects in unpassivated InP/InGaAs HBTs

In this section, we present our experimental results on the DC characteristics of InGaAs/InP SHBTs and DHBTs exposed to electron irradiation. We have also developed a SPICE-like model to describe the DC common-emitter collector current-voltage (I_C - V_{CE}) characteristics of the device. The details of this model are published elsewhere [3.1, 3.2]. All the parameters of this model can be extracted from Gummel measurements. The extracted model parameters of the device before and after irradiation are used to study the radiation-induced degradation of the device performance.

The devices were supplied by Dr. S. Chandrasekhar, Lucent Technologies, Crawford Hill Laboratory. Electron irradiation of the devices was performed at the OSU Radiation Center using a $^{90}\text{Sr}/^{90}\text{Y}$ 100 mCi beta-radiation source. The wafer was placed directly under the source in close proximity of about 2 mm as shown schematically in Fig. 3.1. The device terminals were left in a floating condition at ambient temperature during irradiation. We believe that the biasing condition during irradiation is not a serious issue in the present experiments since the ionizing damage does not play a significant role in the performance degradation of these devices (HBTs). The electrical characterization of the devices was performed using an HP 4145B parameter analyzer before irradiation and after various intermediate doses.

The DC common-emitter collector current-voltage (I_C - V_{CE}) characteristics of a typical unpassivated InP/InGaAs SHBT prior to irradiation and after a dose of $5.4 \times 10^{15} \text{ e/cm}^2$ are shown in Figs. 3.2a. and 3.2b, respectively. Comparison of Figs. 3.2a and 3.2b reveals the following prominent degradation effects: (1) reduction of the collector current (I_C) for a fixed base current (I_B); (2) increase of the collector output conductance ($\Delta I_C / \Delta V_{CE}$) in the forward active regime; and (3) increase of the collector-emitter voltage, $V_{CE,sat}$ at which the emitter current begins to saturate. The I_C - V_{CE} characteristics at a base current of 60 μA for different doses are plotted in Fig. 3.3. From this figure, it is seen that the output conductance increases after a dose of $1.2 \times$

10^{15} cm^{-2} whereas the degradation in I_C becomes significant after a cumulative dose of $2.4 \times 10^{15} \text{ cm}^{-2}$. On the other hand, the increase in $V_{CE(sat)}$ is appreciable only after a dose of $5.4 \times 10^{15} \text{ cm}^{-2}$.

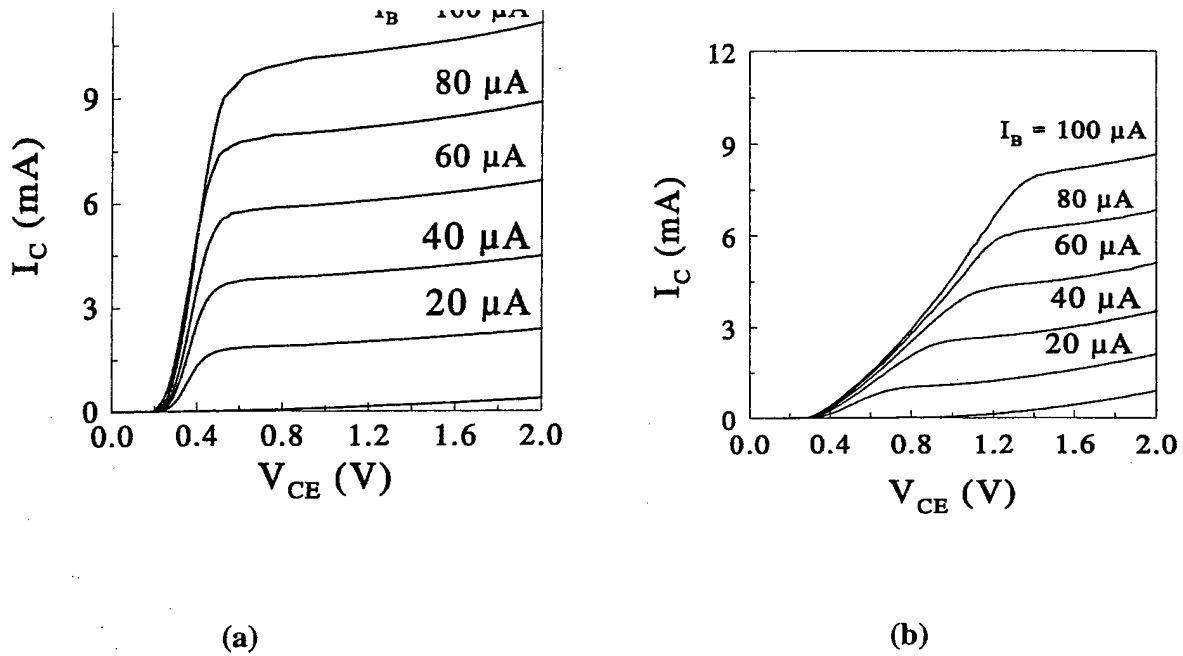


Fig. 3.2 I_C - V_{CE} characteristics of a typical unpassivated InP/InGaAs SHBT. (a) Unirradiated (b) After irradiation with $5.2 \times 10^{15} \text{ e/cm}^2$.

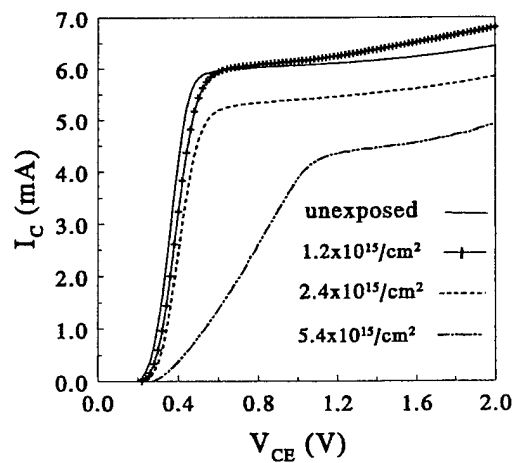


Fig. 3.3 I_C - V_{CE} characteristics of the same device for various electron doses

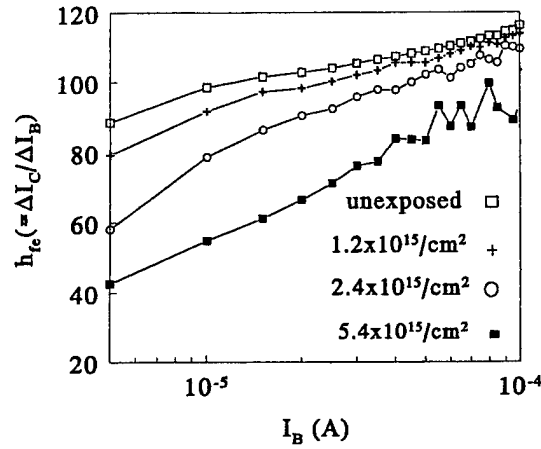
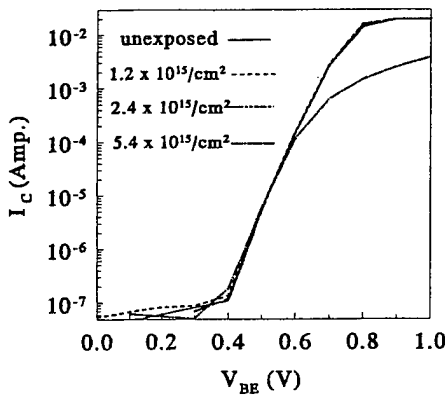
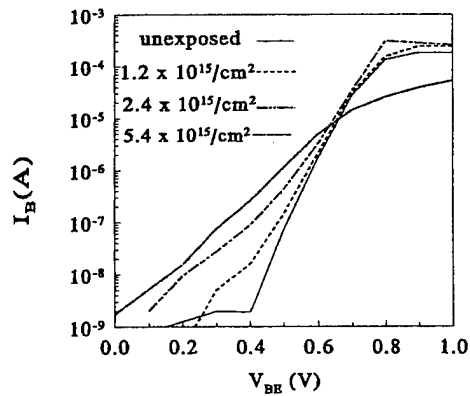


Fig. 3.4 Base current dependence of current gain after different electron doses.

The degradation in I_C as observed in Figs. 3.2 and 3.3 manifests in the degradation of common-emitter current gain ($h_{fe} = \Delta I_C / \Delta I_B$). The base current dependence of gain at $V_{CE}=1.5V$ before and after irradiation is shown in Fig. 3.4. It is seen that the gain degradation (Δh_{fe}) is more at low base currents and decreases gradually at higher base currents. The gain degradation mechanism may be understood with the help of Gummel plots shown in Figs. 3.5a and 3.5b. It is seen that the collector current for a given V_{BE} shows very little change with irradiation. It is only the base current that increases with increasing dose. Thus the gain degradation is caused by increase in the base current. A quantitative analysis of our experimental results using our SPICE model leads to the following conclusions.



(a)



(b)

Fig. 3.5 Gummel plots of (a) I_C and (b) I_B at various of electron doses.

1. The device model parameter representing the recombination in the neutral base region and at its surface increases only by a factor of two after irradiation. On the other hand, the coefficient corresponding to the recombination in the emitter-base junction region increases by nearly six orders of magnitude. Thus we conclude that the gain degradation is mainly caused by the increased recombination at radiation-induced traps in the base-emitter junction and its periphery. The bulk and the surface components of the B-E junction region

recombination could not be separated since devices with different emitter sizes were not included in this work. This effect was later investigated in the case of passivated devices.

2. The ideality factor n representing the recombination in the emitter-base space-charge region and at its periphery shows a significant increase and its value exceeds 2 after exposure. The ideality factor for the collector current does not change appreciably.
3. The increase in the output conductance of the device after irradiation is caused by a decrease in the breakdown voltage of the collector-base junction and the resulting avalanche multiplication of the carriers in the B-C junction depletion regions. The defects introduced in the collector-base junction region are believed to be responsible for the reduction of the junction breakdown voltage.
4. The increase in $V_{CE,off}$ is caused by an increase in emitter series resistance after irradiation.

We also made a similar study of electron irradiation effects in InP/InGaAs/InP DHBTs [3.2]. Comparison between SHBTs and DHBTs showed that the degradation of current gain is similar in both the cases for similar levels of radiation dose. This similarity is believed to be resulting from the fact that emitter-base heterojunctions in both types of devices are nominally identical. Since, our analysis shows that the degradation of current gain is caused by an increased recombination in the emitter-base junction region, the degradation is expected to be similar in both the cases.

Our analysis of the increase in the output conductance of the devices showed that the collector-base junction breakdown voltage of SHBTs decreased from 10 to 3.8V after a dose of $5.4 \times 10^{15} \text{ e/cm}^2$. The breakdown voltage of DHBTs decreased from 18 to 3.5V after a dose of $14.5 \times 10^{15} \text{ e/cm}^2$. The decrease in breakdown voltage roughly scales with the radiation dose. The larger breakdown voltage of the DHBTs before radiation (18 V) is related to the larger band gap of the collector. However, the radiation-induced degradation of the breakdown voltage of DHBTs seems to be very similar to that of SHBTs. Hence, DHBTs do not seem to offer any significant advantage over the SHBTs in terms of radiation tolerance.

The degradation in $V_{CE(sat)}$, however, was significantly different in the two cases. As mentioned earlier, the increase in $V_{CE(sat)}$ is related to an increase in emitter resistance. The emitter resistance of SHBT appears to have increased significantly after electron irradiation as deduced from the observed increase in $V_{CE(sat)}$ from 0.4 to 1.2 V. On the other hand, in the case of DHBTs, $V_{CE(sat)}$ does not show any significant change and hence the emitter resistance appears to be unaffected. Since the emitter material is the same in both cases, we believe that this difference in the increase in the emitter resistances is related to a difference in the degradation of contact resistances. It is very likely that a difference in the processing conditions during the metal deposition has resulted in a larger degradation of the contact resistance in one case over the other.

3.2. Electron Irradiation effects in passivated InP/InGaAs HBTs

3.2.1 Experimental Results

The device structures used in this study were grown by Metal Organic Vapor Deposition (MOCVD) technique by Dr. Andrew Dentai, Lucent Technologies, at Crawford Hill Laboratory. We developed the complete device fabrication steps including the design of masks at Oregon State University. Devices with different perimeter/area ratios of the emitter were included in the mask design in order to separate out the bulk and surface effects. The devices were passivated with a coating of polyimide. The details of the device processing and the lay out of the different devices are described elsewhere [3.3]. Device analysis is carried out at different levels ranging from the commercial SPICE models to custom developed analytical models. The details of the analytical model are also described in Ref. 3.3. The experimental results and the discussion of results of this section are published in Ref. 3.4.

Electron radiation exposure used in this study (sections 3.1 and 3.2) are expressed in terms of cumulative electron fluence. However, in order to be able to make meaningful comparison of these results with those obtained in other electron radiation environments, we have calculated the corresponding ionizing doses, displacement doses, and the expected number of radiation-induced displacements using the theoretical formulation developed in Section 2. The results are summarized in Table 3.1.

Table 3.1 Exposure duration in number of days using 100 mCi ^{90}Sr source, electron fluences, ionizing and displacement doses and the expected number of displacement defects in InGaAs (base and collector regions of the SHBT structure used in this work).

No. of days	Fluence e/cm^2	Cumulative Fluence e/cm^2	D^{InGaAs} (Mrad)	D^{Si} (Mrad)	D_d^{InGaAs} (krad)	N_d (cm^{-3})
1	8.14×10^{14}	8.14×10^{14}	19	24	0.3	6×10^{15}
2	1.63×10^{15}	2.44×10^{15}	57	72	0.8	1.8×10^{16}
4	3.26×10^{15}	5.70×10^{15}	132	166	2.0	4.2×10^{16}
4	3.26×10^{15}	8.96×10^{15}	208	262	3.1	6.6×10^{16}
8	6.51×10^{15}	1.55×10^{16}	360	454	5.4	1.1×10^{17}
14	1.14×10^{16}	2.68×10^{16}	622	784	9.4	2.0×10^{17}

The common emitter I-V (I_C - V_{CE}) characteristics of a typical device of emitter area $750 \mu\text{m}^2$ ($P/A = 0.173 \mu\text{m}^{-1}$) at different base currents (I_B) prior to irradiation are shown in Fig. 3.6a. The I_C - V_{CE} characteristics of the same device after electron irradiation to a cumulative fluence of $2.7 \times 10^{16} \text{e}/\text{cm}^2$ are shown in Fig. 3.6b. The I_C - V_{CE} characteristics of the same device at a base current of $50 \mu\text{A}$ after various intermediate electron fluences are shown in Fig. 3.7. The most significant effect of electron irradiation as observed in Figs. 3.6 and 3.7 is a change in the slope of the I_C - V_{CE} characteristics of the device in the saturation regime after electron irradiation. The maximum collector current for a given I_B is found to be unaffected for electron fluences less than $2.4 \times 10^{15} \text{e}/\text{cm}^2$. For higher electron fluences, the collector current begins to decrease. However,

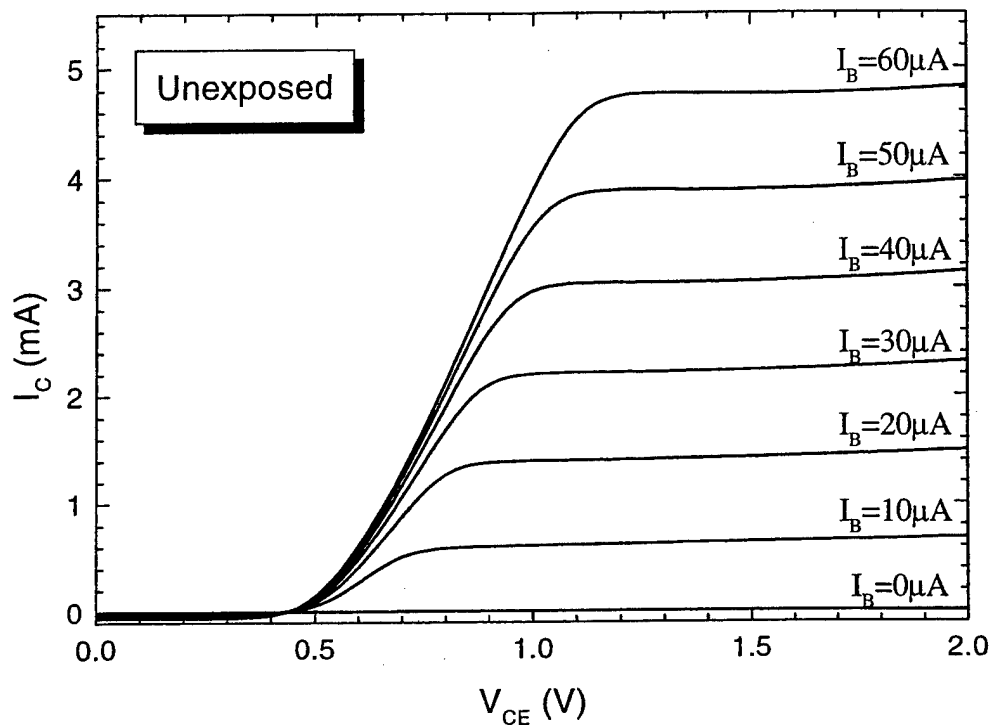


Fig. 3. 6a I_C - V_{CE} characteristics of a typical InP/InGaAs SHBT at different base currents prior to irradiation.

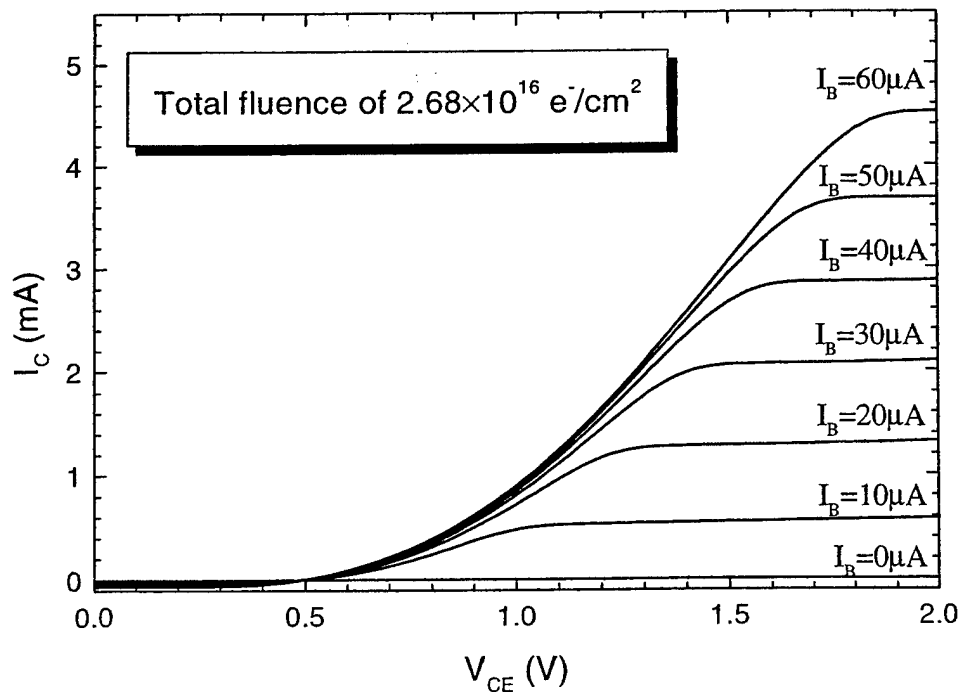


Fig. 3.6 b I_C - V_{CE} characteristics of the same device as in Fig. 3.5 after a dose of $2.7 \times 10^{16} \text{ e}^-/\text{cm}^2$.

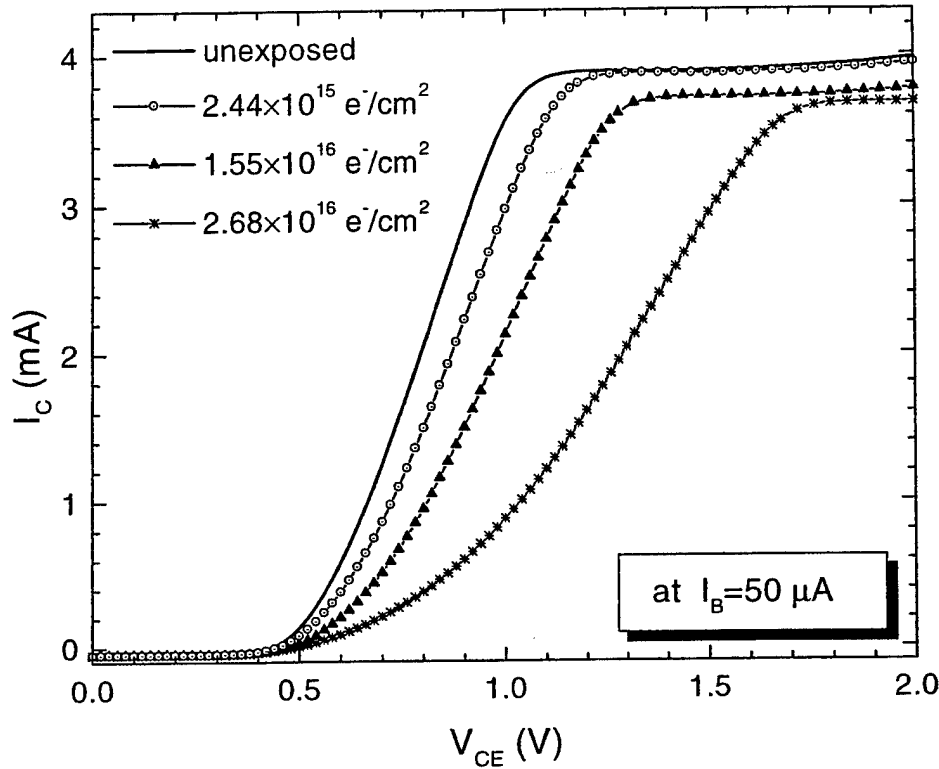


Fig. 3.7 I_C - V_{CE} characteristics of the same device as in Fig. 3.5 at a base current of 50 μ A after various electron doses..

the maximum decrease of the collector current in the active regime after the highest cumulative fluence of $2.7 \times 10^{16} \text{ e}^-/\text{cm}^2$ was found to be only 9 percent. The output conductance of the passivated devices is seen to be completely unaffected even after the highest electron dose. Finally, a slight increase of $V_{CE,off}$ is observed; its discussion will however be postponed till Section 3.3.

The degradation of the DC current gain is found to obey the Messenger-Spratt relationship

$$\frac{1}{\beta} = \frac{1}{\beta_0} + K_\beta \phi_e \quad (3.1)$$

as shown in the Fig. 3.8. From the slope of the best fit line the gain degradation coefficient K_β is found to be $3.7 \times 10^{-20} \text{ cm}^2/\text{e}$.

The Gummel plots of I_C and I_B as functions of V_{BE} for different electron fluences are shown in Fig. 3.9. The collector current shows a constant leakage current for $V_{BE} < 0.6 \text{ V}$. At intermediate values of V_B ($0.6 < V_{BE} < 0.9$) the collector current is unaffected for all the electron doses. The collector current saturates at high values of V_{BE} . We believe that this saturation is caused by the collector series resistance. The maximum collector current, as well as the value of V_{BE} at which the collector current reaches a maximum, decreases with electron fluence implying an increase in the collector series resistance with the dose.

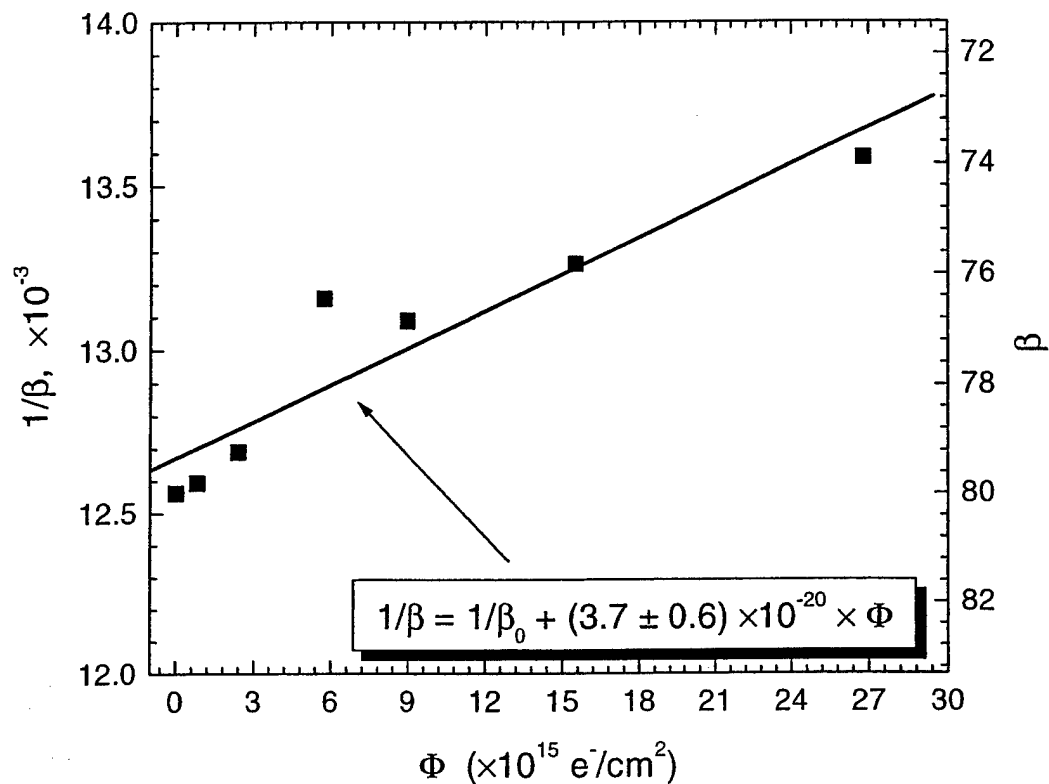


Fig. 3.8 Inverse gain as a function of electron fluence.

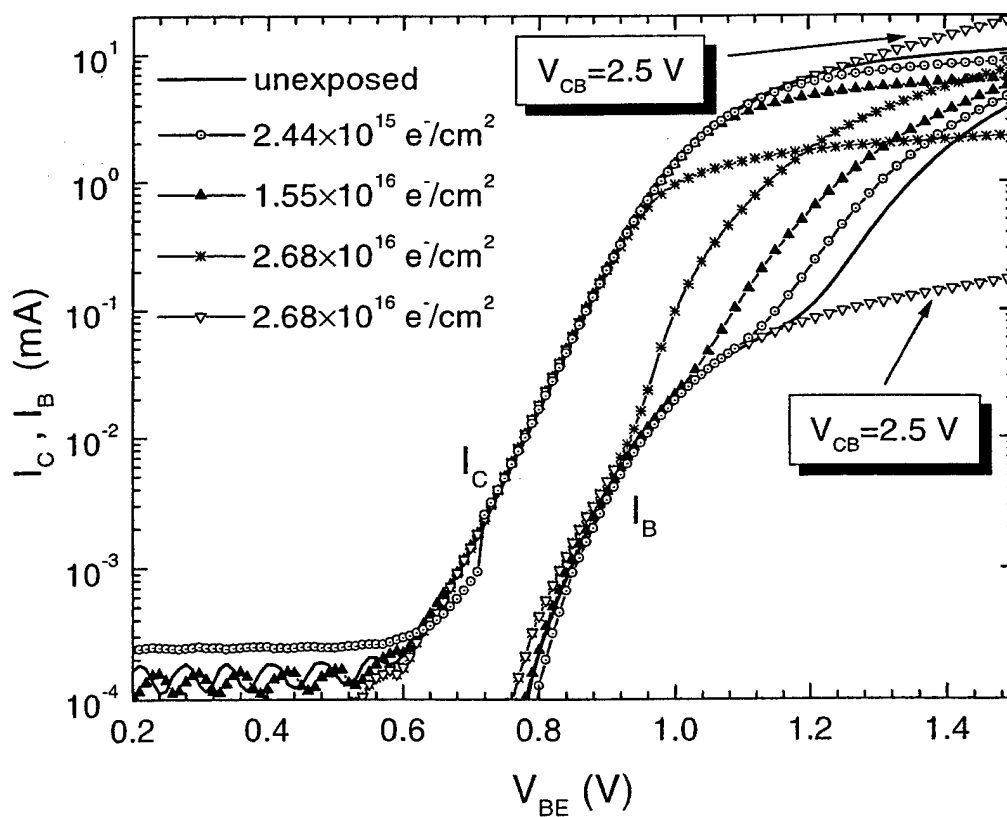


Fig. 3.9 Gummel plots of I_C and I_B at various electron doses

The base current, on the other hand, shows a sharp increase in the high V_{BE} regime. We believe that this behavior is caused by the collector series resistance as shown by Liou et al. [3.5] and Sotoodeh et al. [3.6]. The Gummel measurements are normally done with a zero voltage applied across the base and collector probes (i.e. $V_{CB} = 0$). The collector current causes a voltage drop across the collector series resistance, which in turn forward biases the internal base-collector junction and gives rise to additional base current. The voltage drop across the series resistor becomes significant as I_C increases giving rise to a sharp increase in I_B in the high V_{BE} regime. This model is also independently verified by Gummel measurements at $V_{CB} = 2.5V$. At this value of V_{CB} the base-collector junction remains reverse biased even at the highest value of V_{BE} eliminating the sharp increase in I_B as shown in Fig. 3.9 for the highest dose. It is also significant to note that the sharp increase in I_B (with $V_{CB} = 0$) occurs at progressively lower values of V_{BE} with increasing electron dose. Once again this behavior is consistent with a gradual increase in the collector series resistance with increasing electron irradiation dose.

In the low V_{BE} regime ($V_{BE} < 1.0 V$), the base current decreases slightly for small doses (up to $2.44 \times 10^{15} \text{ e/cm}^2$) and then begins to increase for larger doses. The DC common emitter current gain as a function of the collector current is shown in Fig. 3.10 for various electron doses. At low collector currents ($I_C < 1 \text{ mA}$), the current gain increases slightly for low doses and then begins to decrease for the higher doses. This behavior correlates with the decrease of I_B for low doses followed by an increase at higher doses shown in Fig. 3.9. A similar decrease in I_B for small doses of gamma irradiation of InAlAs/InGaAs HBTs has been reported by Witmer [3.7].

It is also seen from Fig. 3.10 that the gain increases with collector current, reaches a maximum at some value of I_C and then begins to decrease for higher I_C . The decrease in gain at higher I_C is also due to the collector series resistance. The value of I_C at which the gain reaches a maximum decreases with the increase in electron dose confirming an increase in the collector series resistance with electron irradiation. In order to check independently the hypothesis of the

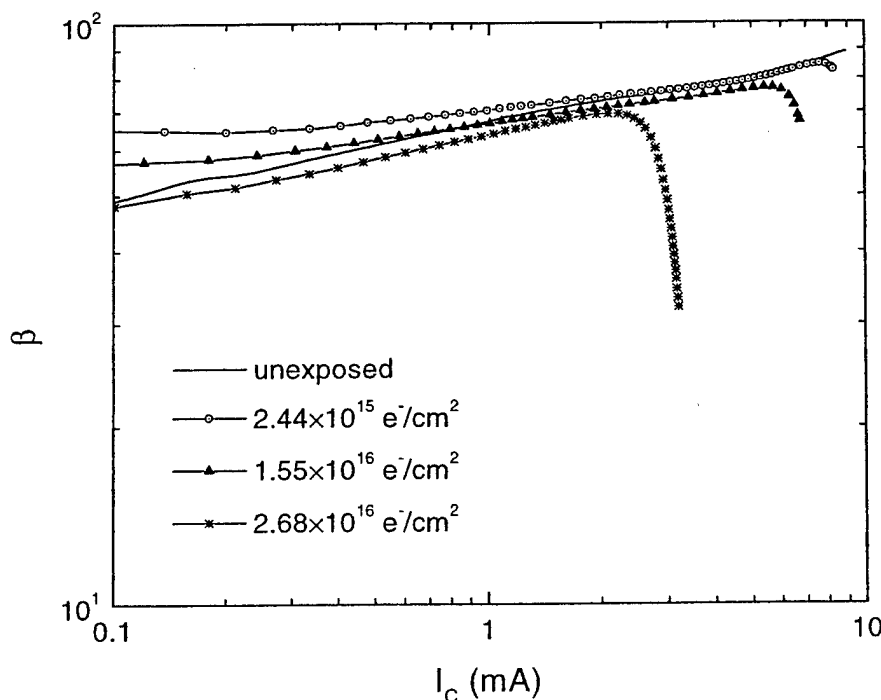


Fig. 3.10 Collector current dependence of gain for various electron doses.

increase in the collector series resistance with increasing electron dose, we also performed I-V measurements of base-emitter and base-collector junctions of the HBTs. While the BE diodes showed no evidence of increase in series resistance, the BC diodes showed a gradually increasing series resistance with increasing electron fluence. The ideality factor for the BC diode (n_{BC}) showed an increase from 1.27 prior to irradiation to 1.82 after the highest dose. This increase in the ideality factor is easily explained by the increase in the generation-recombination current (which has an ideality factor of 2.0) caused by the radiation induced defects in the collector depletion region.

3.2.2 Gain Degradation Mechanisms

From the Gummel plots in Fig. 3.9, it is seen that the collector current does not change with irradiation. It is the small changes in the base current with irradiation that gives rise to the gain degradation. The base current ideality factor is found to be ~ 1.8 for all the electron doses. It is well known that the recombination current arising junction space charge region (SCR) has an ideality factor ~ 2 . Hence we believe that the base current in our devices is mainly contributed by the emitter base junction SCR recombination. The gain degradation is also due to the increase in the junction SCR component of the base current. The collector current dependence of gain shown in Fig. 3.10 supports this hypothesis. At low V_{BE} , the base current is almost entirely made of junction SCR current and hence the gain degradation is more. As the collector current (or base current) is increased, the gain degradation becomes smaller. It is well known that the quasi-neutral base region recombination begins to dominate at the higher base currents. The smaller gain reduction at higher base currents indicates that the quasi-neutral region recombination is not significantly affected by electron irradiation. The quasi-neutral bulk recombination predominantly takes place via radiative recombination and Auger recombination. The radiative recombination rate is proportional to the product (pn) of the hole and electron concentration in the base. The Auger recombination rate goes as pn^2 or np^2 . Since the base region of an HBT is typically very heavily doped (10^{19} cm^{-3}) the radiation-induced defects do not significantly affect the carrier concentrations in the base. Hence the base current arising from these mechanisms is also not affected by electron irradiation.

The slight increase in current gain at smaller doses seen in Fig. 3.10 is believed to be related to the charge build up in the polyimide layer due to the ionization damage. This hypothesis is supported by the results of our test experiments on Si MIS capacitors using the polyimide as the insulating layer that shows a shift of the C-V curves after electron irradiation suggesting the trapping of negative charges in the polyimide layer. For higher electron doses, this effect saturates and the increased recombination due to the radiation-induced defects in the bulk and the periphery of the depletion region causes the base current to increase again. The mechanism proposed here for the gain increase at small doses is somewhat similar to that of the total dose effects caused by the charge trapping in the oxide layers near the junction regions in silicon bipolar transistors [3.8]. However, it is interesting to note that in contrast with silicon BJTs the total dose effects in InP/InGaAs HBTs are small and that the gain degradation is mainly dominated by the displacement damage in the base-emitter junction region.

At very high collector currents, the gain begins to decrease due to the collector series resistance. Using a custom Ebers-Moll model we fitted the Gummel plots in Fig. 3.9 to extract the values of the series resistances associated with the emitter R_E , the base R_B and the collector R_C . The extracted values of R_E , R_B , and R_C were found to be 21, 50 and 52 ohms, respectively, before irradiation, and 31, 81, and 380 ohms after the highest dose of electron irradiation.

3.2.3 Comparison with Unpassivated Devices

In contrast with the studies on unpassivated InP/InGaAs SHBTs and DHBTs presented in Section 3.1, the polyimide-passivated devices show much less degradation. The degradation effects in the unpassivated devices include a larger gain reduction, increase in the output conductance and an increase in $V_{CE,sat}$ due to an increase in series resistance. As is evident from the Gummel measurements, the decrease of current gain is caused by an increase in the base current. The difference in the base currents between the passivated and unpassivated devices can only arise from the BE junction surface (perimeter) recombination and the extrinsic-base surface recombination. The recombination in the bulk depletion region (under the emitter contact) and in the intrinsic quasi-neutral base region are expected to be identical in both the cases. The energy loss of electrons in the polyimide layer is very small (less than 0.02~MeV) and hence the total ionizing dose rate (dD/dt) in the active volume of the device is nearly the same for both the passivated and the unpassivated samples. Hence, the increased radiation hardness of the passivated devices is not due to the 'radiation shield' provided by the polyimide layer. We attribute the larger degradation of the unpassivated devices to the presence of the free surface. We believe that the free surface of a semiconductor is more susceptible to radiation damage than a passivated surface is due to the presence of a large number of dangling bonds at the free surface. Our studies of the mobility degradation of unpassivated modulation-doped heterostructures [3.9] also show evidence of the susceptibility of a free surface to more radiation damage.

The increase in the output conductance of the unpassivated devices after irradiation was argued to be caused by a reduction of BC junction breakdown voltage [3.1, 3.2]. On the other hand, the passivated devices studied in this work did not show any increase in the output conductance even after the highest electron dose. This difference in behavior between the passivated and the unpassivated devices shows that the breakdown of the BC junction of the unpassivated devices may be triggered at the junction edges rather than in the bulk since the bulk damage in both types of devices is expected to be same.

The increase in $V_{CE,sat}$ has been observed in both the unpassivated and the passivated devices. However, this increase in the unpassivated devices in our earlier work was found to be related to an increase in the emitter series resistance whereas it is found to be related to an increase in the collector series resistance in this work. It should be also pointed out that the magnitude of the increase in $V_{CE,sat}$ is not uniform for all the devices studied. While some devices show a larger increase other devices show a much smaller increase. The results shown in Figs.3.6 and 3.7 are typical. This non-uniform degradation of $V_{CE,sat}$ suggests that the increase in series resistance might be related to the degradation of the contact resistance rather than the bulk resistance. The variability of the surface conditions on the wafer just before the metal deposition may be responsible for the non-uniform degradation of contacts on different devices. Further work is necessary to understand and eliminate this degradation behavior.

3.2.4 P/A Ratio Dependence of Gain Degradation

The gain degradation in the active regime for devices with different size emitters were found to be nearly the same and did not show any correlation with the P/A ratio of the devices. However, this comparison is not quite meaningful since the current densities of the different emitter size devices in the active regime are different for the same value of I_B . The gain degradation at a given collector current density for a wide range of P/A ratio devices could not be compared due to the parasitic series resistance effects on the gain at high collector currents. The P/A ratio dependence of the gain degradation for devices within a limited range of P/A shows that the normalized gain degradation is smaller for the larger P/A devices. This result is explained as

follows. As argued earlier, the radiation-induced damage at the emitter periphery is small for the passivated devices. Thus one may assume that the base current arising from the surface recombination at the BE junction periphery is not affected by irradiation. Since this component of the current is more dominant in the larger P/A devices, the overall gain degradation is smaller. A similar behavior has been observed by Song et al. [3.10] for the neutron irradiated AlGaAs/GaAs HBTs and by Sarkar et al [3.11] for the electron irradiated AlGaAs/GaAs HBTs as discussed in Section 4.

3.2.5 Degradation Variation

To conclude this section, we briefly present some data on the statistical variation of the device parameters and their degradation obtained from a larger number of devices. Unirradiated transistors exhibited gain in the range from 51 to 70 (see Fig. 3.11) with the mean of 60 and standard deviation of 6. After irradiation some of the devices showed lower gains in the range of 80% - 100% of β_0 . The distribution of the gain for different devices is shown in Fig. 3.12 for the highest dose used. A few devices showed either little improvement or no degradation at all, while majority of the devices have gains of 80-90% of their initial values.

Initial $V_{CE,sat}$ values, which are determined by the series resistance effects, fall into the range of 0.95-1.05 V. For most of the devices $V_{CE,sat}$ degrades very quickly. Some devices, however, show relatively little change of this parameter. No correlation is observed between the initial and final values of the saturation voltage. Final distribution of $V_{CE,sat}$ is shown in Fig. 3.13 for the devices after the highest dose. The voltages vary in the range of 1-3 V. The exact cause of such a wide $V_{CE,sat}$ distribution is not currently understood, but is most likely related to the sample surface conditions immediately before the contact deposition.

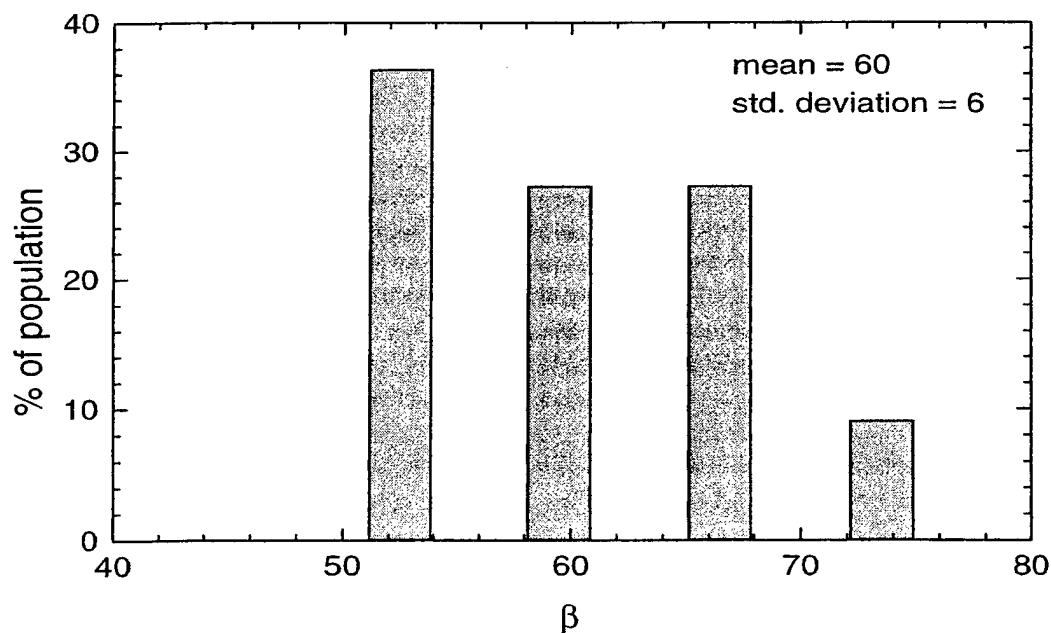


Fig. 3.11 Gain distribution of the device population before irradiation

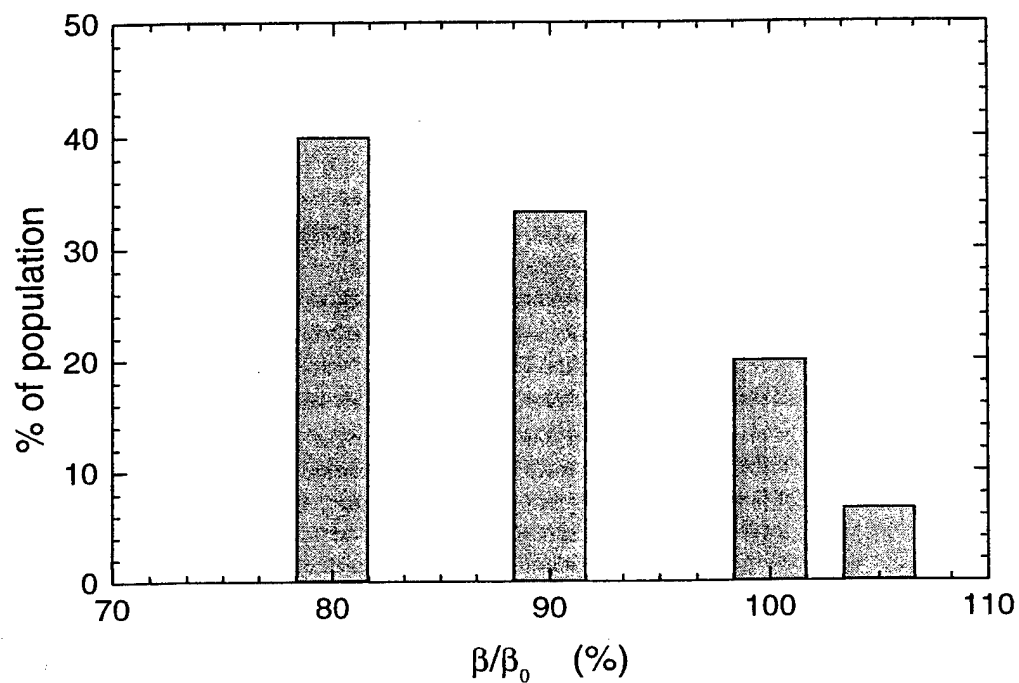


Fig. 3.12 Gain distribution of the device population after the highest dose

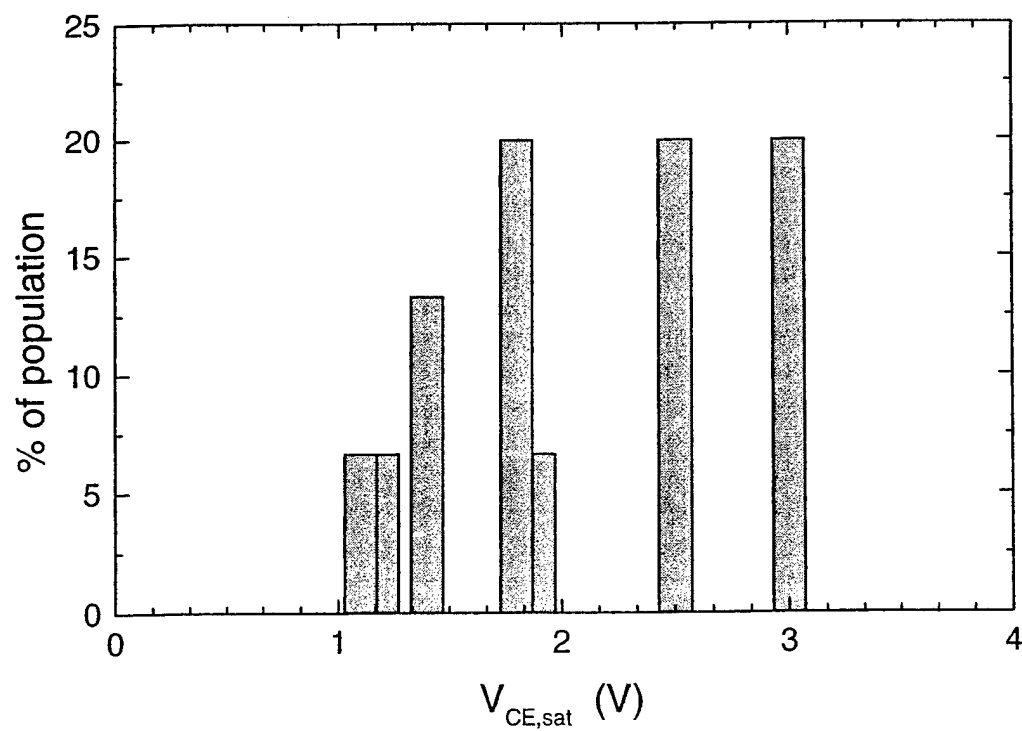


Fig. 3.13 Distribution of $V_{CE,sat}$ of the device population after the highest dose.

3.3 Neutron Irradiation effects in InP/InGaAs HBTs

Neutron irradiation was performed at ambient temperature using the Triga Mark II nuclear reactor at Oregon State University Radiation Center operated at 100 KW. The samples were in the wafer form and the devices were unbiased during irradiation. The samples were enclosed in cadmium boxes during irradiation to block the thermal neutrons. The electrical characterization of the devices was performed before and after irradiation using HP4145B parameter analyzer. Separate wafer-segments cut from the same wafer were used for different doses. A significant number of devices were characterized to ensure the uniformity of the observed radiation effects. The tested devices included different emitter sizes in the range from 150 to 2600 μm^2 .

The common emitter J_C - V_{CE} characteristics of a typical device with an emitter area of 1050 μm^2 at a base current of 40 μA for different neutron doses are shown in Figure 3.14. The two most significant effects of neutron radiation observed from this figure are: (1) Decrease of collector current or equivalently the decrease of common emitter current gain and (2) Increase of collector-emitter offset voltage ($V_{CE, \text{offset}}$). Our analysis of the experimental data shows that these two effects are caused by the neutron irradiation induced defects in the emitter-base junction region, and the base-collector junction region, respectively.

In order to understand the current gain degradation mechanism, we have performed Gummel measurements before and after irradiation. The results are shown in Fig. 3.15. The collector current has a significant leakage component in the low V_{BE} range in our unirradiated devices. The origin of this leakage current is not presently understood. However this leakage current decreases significantly after neutron irradiation. In the intermediate V_{BE} range, the collector current is found to be practically unaffected by neutron irradiation. The decrease of collector current in the high V_{BE} range is caused by a combination of both high-level injection effects and the emitter series resistance. We have performed a SPICE device model analysis of the J_C - V_{BE} characteristics for different doses by using the equation

$$J_C = J_{C0} \exp\left(\frac{qV_{BE}'}{mkT}\right) \quad \dots(3.2a)$$

where V_{BE}' is the actual voltage across the BE junction which is related to the applied voltage V_{BE} through the relation

$$V_{BE}' = V_{BE} - I_E R_E - I_B R_B \quad \dots(3.2b)$$

where R_E and R_B are the series resistances associated with the emitter and base. By fitting the experimental data to eqs. 3.2a and 3.2b, we have extracted the collector current ideality factor m , saturation current density J_{C0} and the emitter series resistance. It is observed that the saturation current ($\sim 2 \times 10^{-7}$ A/cm²) and the ideality factor (~ 1.3) for the collector current are relatively unaffected by neutron irradiation. The collector current ideality factor m is normally unity for a homojunction transistor. For an HBT, a value of $m \sim 1.3$ is typical and it is related to the conduction band spike at the B-E heterojunction. The insensitivity of the values of m and J_{C0} to neutron irradiation shows that the current injection mechanism (thermionic emission) at the B-E heterojunction is not affected by radiation. The normalized emitter series resistance is found to increase from 1.0 to ~ 1.8 after the highest dose used in this work.

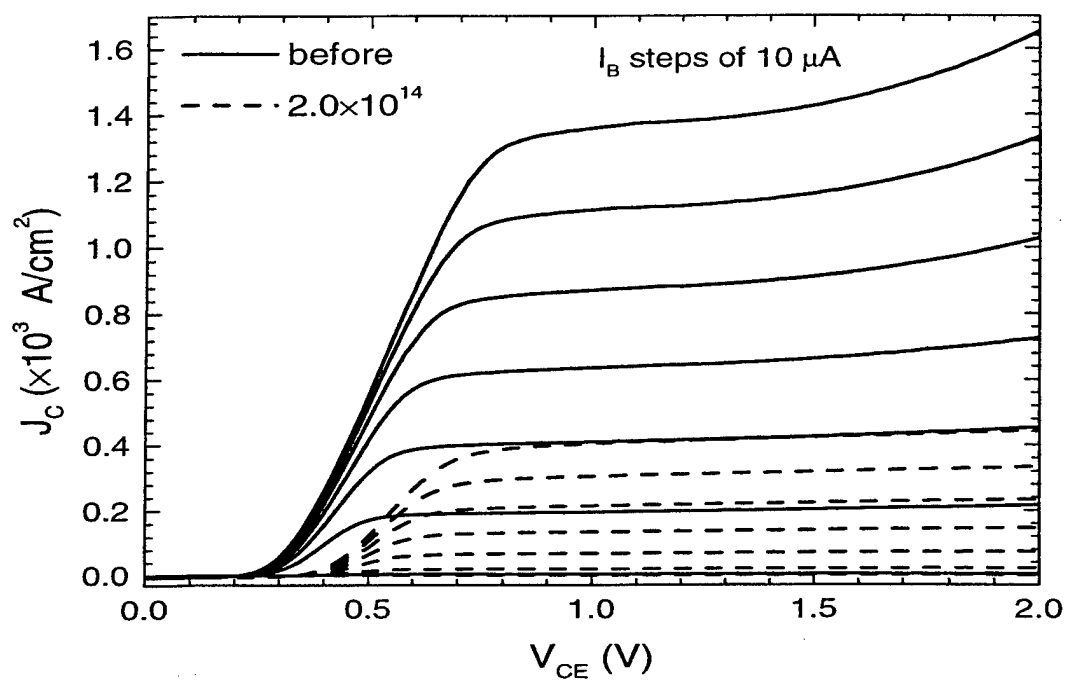


Figure 3.14: The common emitter J-V (J_C - V_{CE}) characteristics for various neutron fluences.

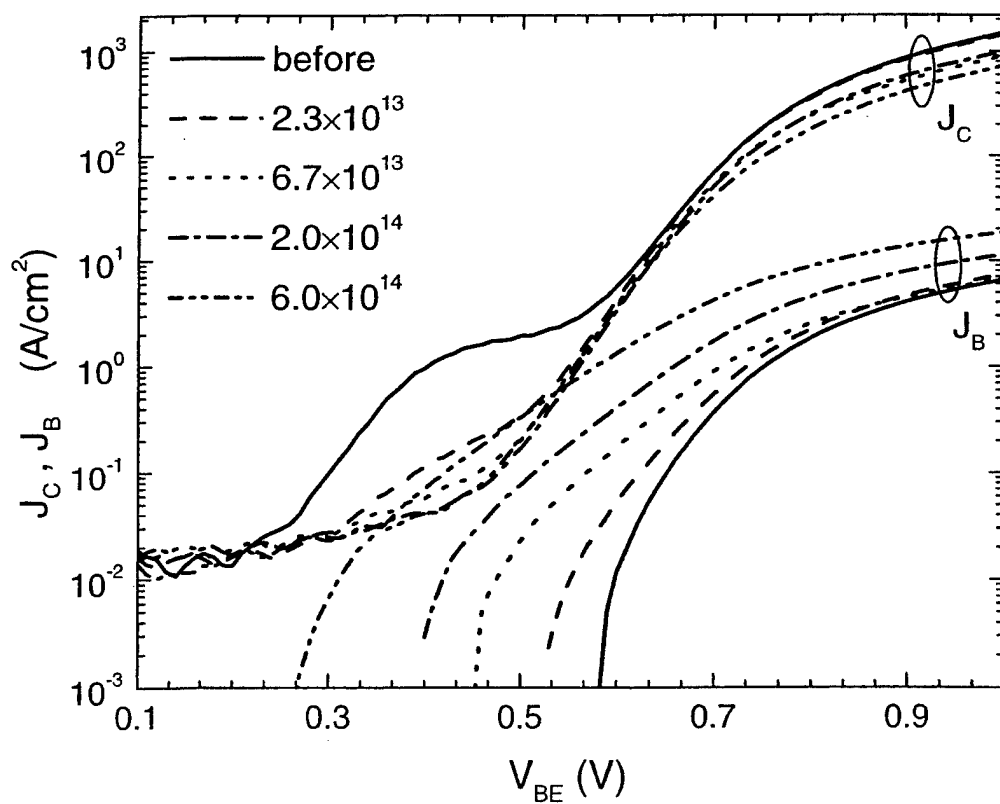


Figure 3.15: Gummel plots of J_C and J_B for intermediate fluences

The base current increases steadily with increase in dose as shown in Fig. 3.15. Since the collector current is relatively unchanged with radiation, the increase in base current implies a degradation of current gain with increasing neutron dose. The collector current dependence of gain for various neutron doses is shown in Fig. 3.16. The dependence of current gain on the collector current can be understood by analyzing the different components of the base current given by

$$J_B = J_{B,BR} + J_{B,SCR} + J_{surf} \quad \dots(3.3)$$

where $J_{B,BR}$, $J_{B,SCR}$, and J_{surf} arise from the recombination in the quasi-neutral bulk region of the base, recombination in the B-E junction space charge region (SCR), and the surface recombination at the B-E junction periphery and the extrinsic base region, respectively. For our devices, $J_{B,scr}$ is found to be small since the current gain is only weakly dependent on the emitter size (P/A ratio) as shown in Fig. 3.17. In fact, the current gain of the devices after the final dose is completely independent of P/A suggesting that the base current in the irradiated devices is almost entirely due to bulk recombination. We analyzed the base current by using the following expressions for the first two terms in eq. 3.3.

$$J_{B,BR} = \frac{J_{C0}}{\beta_{BR}} \exp\left(\frac{qV_{BE}}{mkT}\right) \quad \text{and} \quad J_{B,SCR} = C_2 J_{C0} \exp\left(\frac{qV_{BE}}{nkT}\right) \quad \dots(3.4)$$

The ideality factor n for SCR recombination is generally ~ 2 for recombination involving a single mid-gap level defect. Our analysis shows that an ideality factor greater than 2 may be obtained for recombination involving defects with a distribution of energy levels in the band gap.

For the unirradiated device, the contribution of the second term in eq. 3.3, $J_{B,SCR}$ is very small. Hence the current gain is constant at β_{BR} for all V_{BE} and hence it is independent of J_C as seen in Fig. 3.16. Neutron irradiation, however, gives rise to a significant increase in $J_{B,SCR}$ due to the displacement damage. For small V_{BE} , the second term in eq. (3.3), $J_{B,SCR}$ is more dominant. From eqs. 3.2a and 3.4, it is clear that the current gain is dependent on V_{BE} , or equivalently on J_C as seen in Fig. 3.16. Indeed, the base current ideality factor n determined from the low V_{BE} regime increases from ~ 1.3 for the unirradiated devices to ~ 2.8 for the highest dose confirming that the increase in base current after irradiation arises from the SCR recombination in the base-emitter junction. For large V_{BE} the first term $J_{B,BR}$ is dominant and the gain once again is independent of J_C .

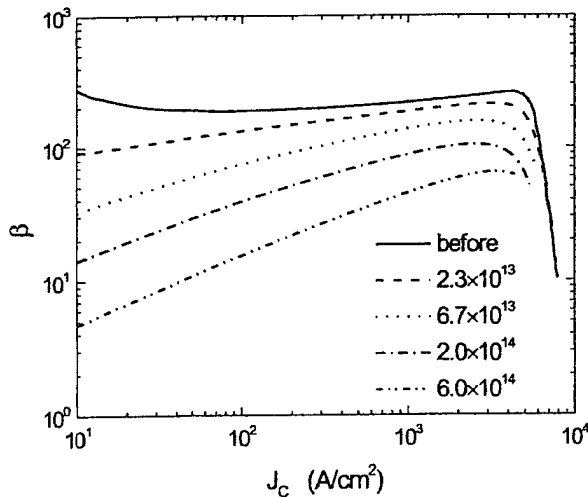


Figure 3.16 DC current gain as a function of collector emitter current density for different doses

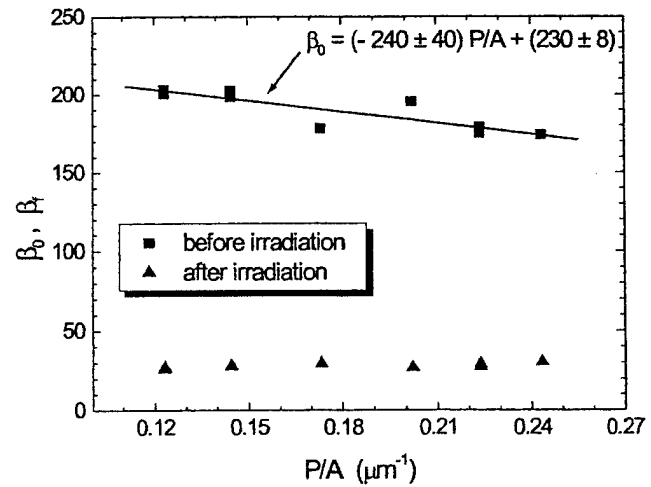


Figure 3.17 DC current gain as a function of P/A ratio for devices before and after radiation.

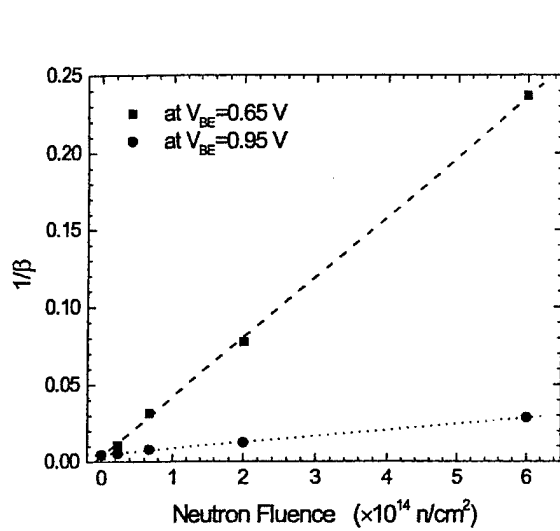


Figure 3.18 Inverse DC current gain as a function of neutron fluence measured at $V_{BE} = 0.65$ and 0.95 V.

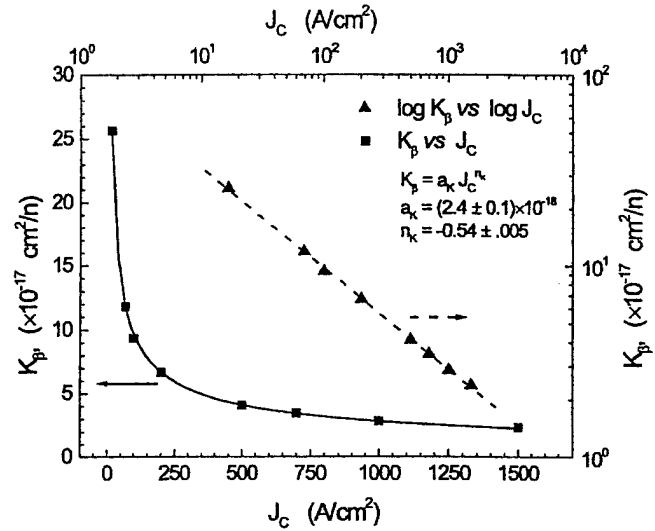


Figure 3.19 Gain degradation coefficient as a function of collector current density.

The gain degradation with neutron dose is found to obey the Messenger-Spratt relation

$$\frac{1}{\beta} = \frac{1}{\beta_0} + K_\beta \phi \quad \dots(3.5)$$

for all values of J_C . Examples of such plots for two different values of V_{BE} are shown in Fig. 3.18. The gain degradation coefficient K_β however is dependent on J_C since the dominant base current component is different in different V_{BE} regimes. In the low V_{BE} regime, the gain and the gain degradation coefficient are determined by the SCR recombination component of the base current and are strongly dependent on J_C . In the high J_C regime, K_β is less sensitive to J_C suggesting that the gain degradation in this regime is governed by the degradation of excess carrier lifetime in the quasi-neutral bulk region. The collector current dependence of K_β is shown in Fig. 3.19 and is found to obey the following power law relation with $r \sim -0.5$.

$$K_\beta = C J_C^r \quad \dots(3.6)$$

We will now discuss the origin of the increase in the $V_{CE,offset}$ caused by neutron irradiation. $V_{CE,offset}$ is an important device parameter for digital applications since any increase in $V_{CE,offset}$ causes an increase in power dissipation in saturating logic circuits and also increases the low level voltage and reduces the low noise margin of the circuit. We believe that the neutron induced increase in $V_{CE,offset}$ is caused by an increase in the saturation current of the B-C junction. The $V_{CE,offset}$ for a given base current I_b is given by

$$V_{CE,offset} = R_E I_b + \frac{n' kT}{q} \ln \frac{A_C J_{CS}}{\alpha_F A_E J_{ES}} \quad \dots(3.7)$$

where A_C , and A_E are the base-collector and base-emitter junction areas, respectively, J_{CS} and J_{ES} are the saturation currents of the B-C junction and the B-E junction, respectively and α_F is the common base forward gain of the transistor. In eq. 3.7, the ideality factors of B-E and B-C junctions are both assumed to be equal to n' . For our devices the contribution of the first term $R_E I_b$ in eq. 3.7 is very small. Eq. 3.7 may be rewritten for the value of $V_{CE,offset}(I_b)$ measured at a given I_b in the common emitter mode as

$$V_{CE,offset}(I_b) = \frac{kT}{q} \ln \left[\frac{(I_{BC}/I_b)^{n'}}{(I_C/I_b)^m} \right] \quad \dots(3.8)$$

where I_{BC} is the base current of the B-C junction as obtained from the inverse Gummel plot, n - the base current ideality factor in the inverse Gummel plot, I_C - the collector current from the forward Gummel plot and m is the collector current ideality factor in the forward Gummel plot. A graphical interpretation of eq. 3.8 is that the $V_{CE, offset}$ is simply obtained from the horizontal (voltage) displacement between the base current inverse Gummel plot and the collector current plot, at the desired value of I_b as shown in Fig. 3.20. As discussed earlier and also as seen in Fig. 3.20, the collector current in the forward Gummel plot is relatively unaffected by neutron irradiation. It is only the base current of the B-C junction (from the inverse Gummel plot) that increases steadily which in turn causes the increase in $V_{CE, offset}$. A comparison of $V_{CE, offset}$ determined by this procedure and the value of $V_{CE, offset}$ directly read from the common emitter J_C - V_{CE} characteristics is shown in Fig. 3.21. From this analysis it is clear that the increase in $V_{CE, offset}$ is directly related to the neutron radiation induced degradation of the B-C junction saturation current.

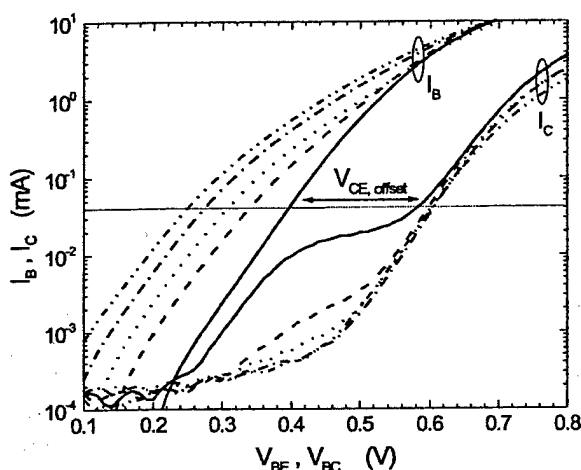


Fig. 3.20 Base currents from inverse and collector currents from forward Gummel plots for different doses.

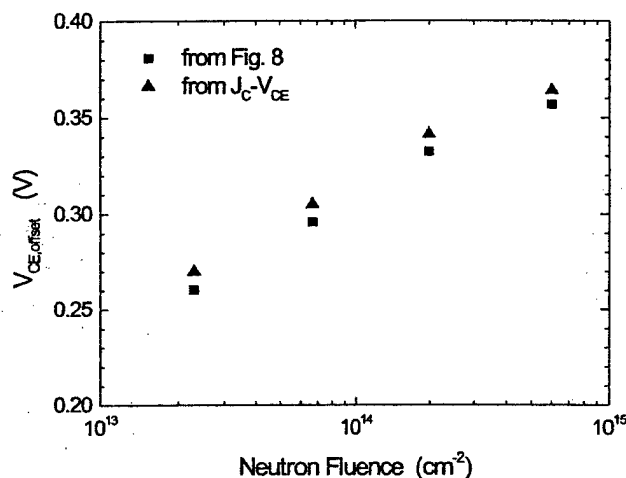


Fig. 3.21 $V_{CE, offset}$ extracted from Fig. 3.19 and J_C - V_{CE} as a function of neutron fluence.

3.4 Gamma Irradiation Effects in InP/InGaAs HBTs

Gamma irradiation of the devices was performed using a ^{60}Co gamma cell with the typical dose rate of 250 krad(Si)/hour. The device terminals were left in a floating condition at ambient temperature during irradiation. The maximum cumulative dose used in the present experiments was 44.3 Mrad(Si). The electrical characterization of the devices was done using an HP 4145B semiconductor parameter analyzer before irradiation and after intermediate doses of 0.3, 1.3, 4.3, 14.3 and 44.3 Mrad. The measurements were typically performed within a few hours after the irradiation.

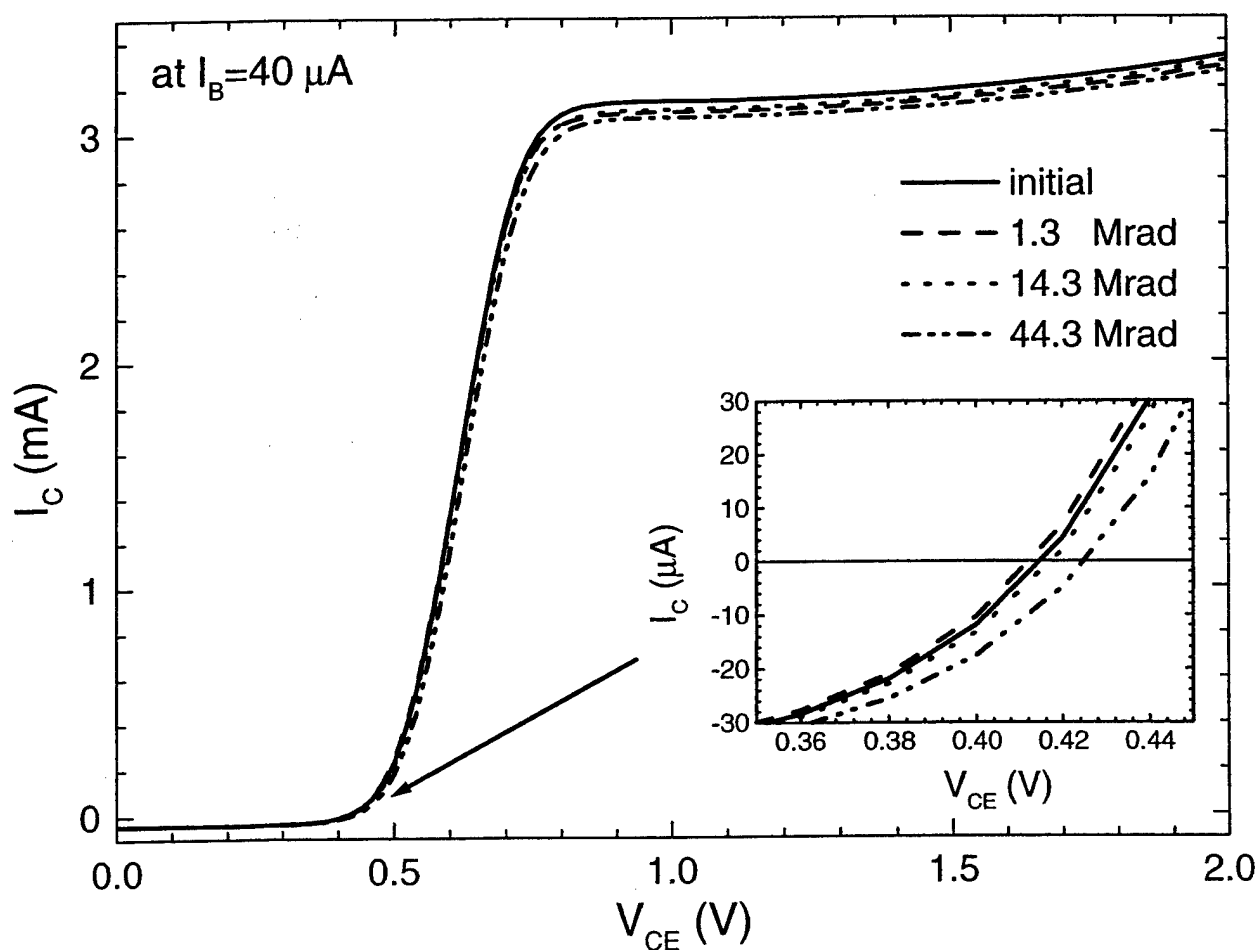


Fig. 3.22 I_C - V_{CE} characteristics of a typical device in group I for various gamma doses.

The devices investigated in this study may be classified into three groups depending on the extent and nature of degradation after gamma irradiation. The first group, which comprises of about forty percent of the total number of devices studied, suffered least degradation. Typical common-emitter I_C - V_{CE} characteristics measured at a base current of 40 μA at different intermediate doses are shown in Fig. 3.22. Only very slight decrease in the collector current and increase in $V_{CE,off}$ (as shown in the inset of Fig. 3.22) is observed. The collector current

dependence of DC current gain of these devices for various doses is shown in Fig. 3.23. There is very little change in gain at the high collector currents. The small decrease of gain in the low I_C

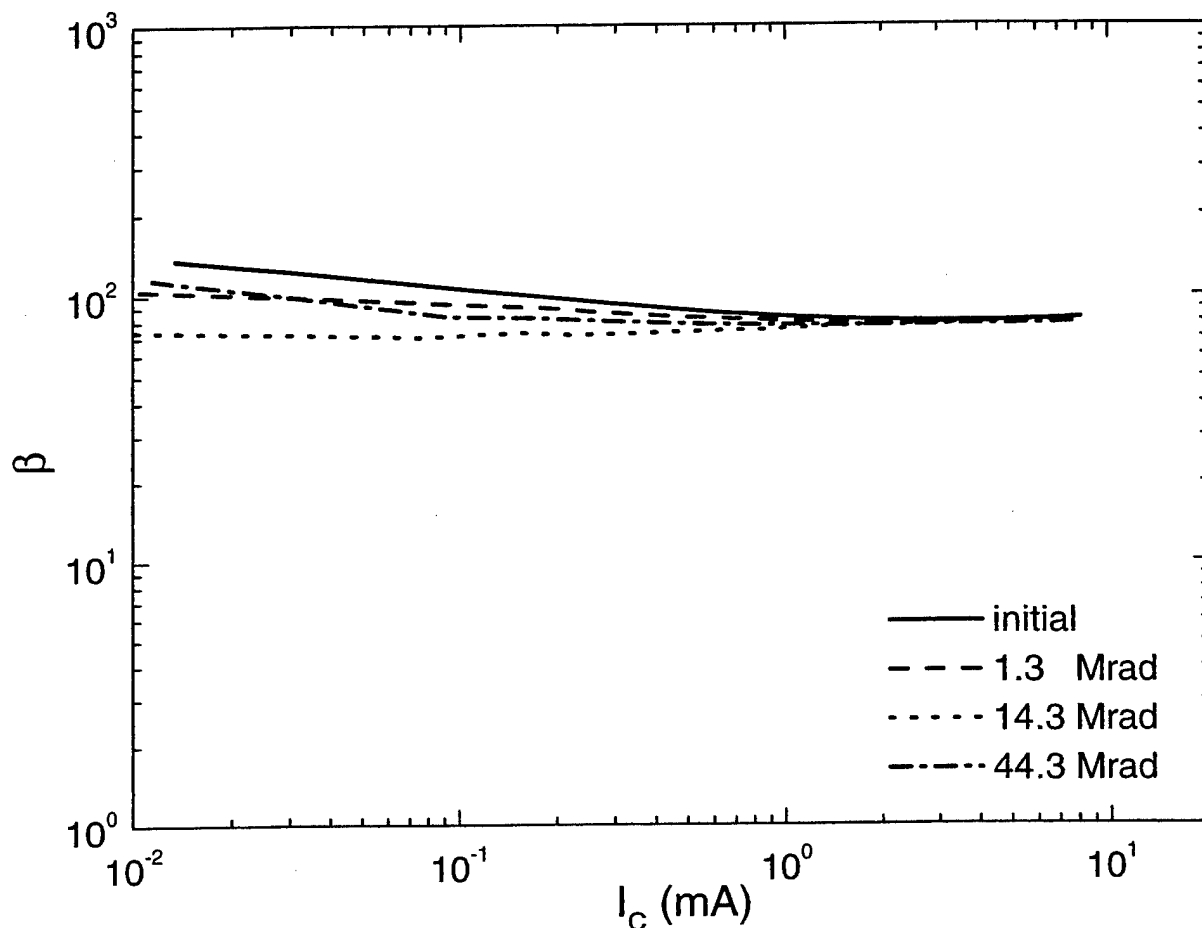


Fig. 3.23 DC current gain as a function of collector current for various gamma doses.

regime is associated with the base current increase. This increase in the base current is believed to be caused by the displacement damage in the BE depletion region associated with the gamma radiation and the additional recombination at these defect sites.

The second group of devices showed no degradation up to a certain dose and then a sudden jump in the collector, base and emitter leakage currents in the low bias range as shown in Figs. 3.24 and 3.25. In the high bias regime, the degradation is small, but is larger than that of the first group of devices. The common-emitter I_C - V_{CE} characteristics measured at a base current of $40\mu A$ at different intermediate doses are shown in Fig. 3.26. The collector current dependence of the gain of this group of devices is shown in Fig. 3.27. It may also be mentioned that the dose at which the devices showed the sudden degradation was not the same for all the devices in this group. About forty percent of the devices studied belong to this group. We believe that the large increase in the leakage currents in the low bias regime is caused by the degradation of the polyimide-semiconductor interface. The physical mechanism of the degradation is not exactly

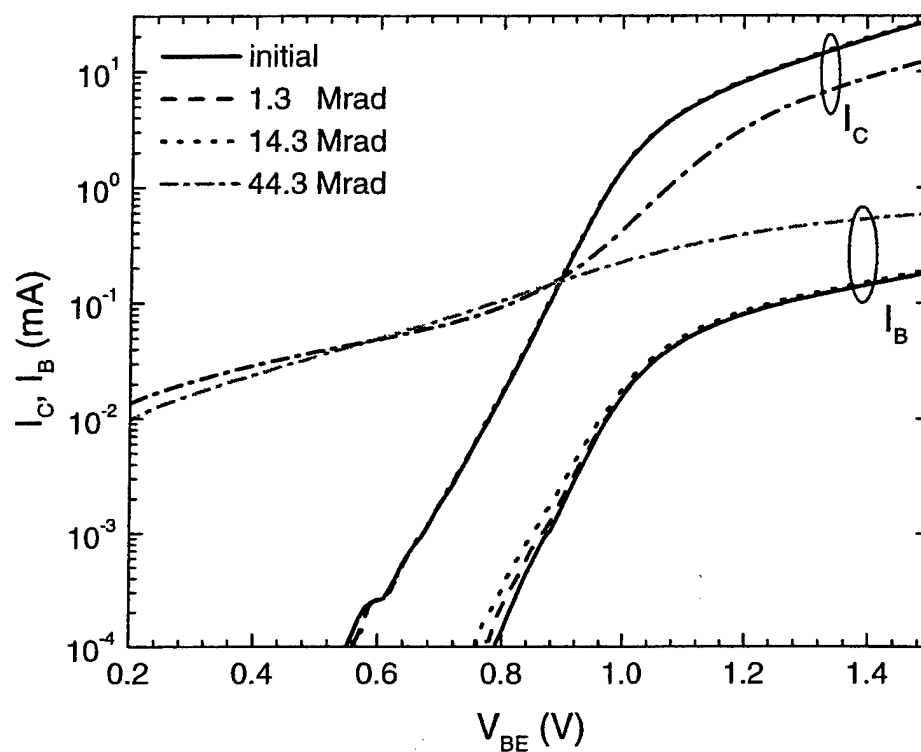


Fig. 3.24 Gummel plots of a typical device in group II for various doses

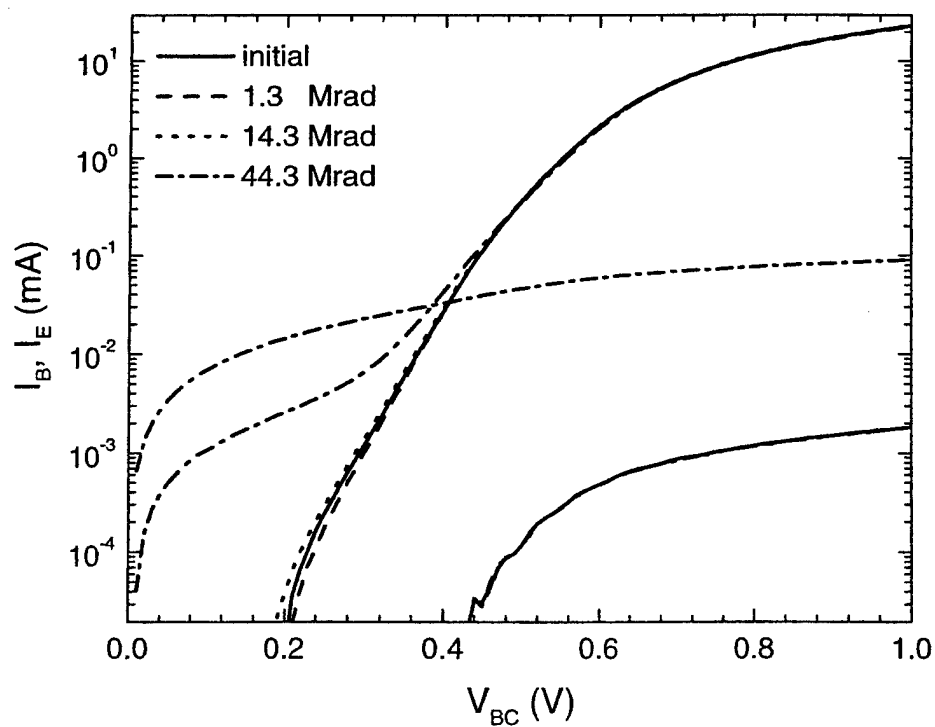


Fig. 3.25 Inverse Gummel plots of a typical device in group II for various doses

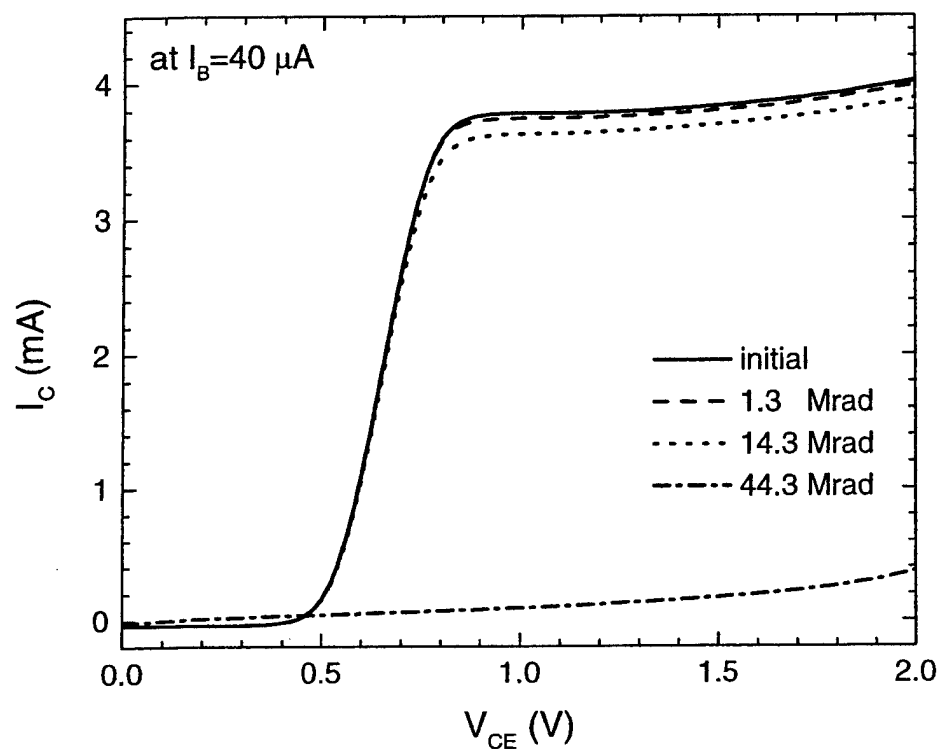


Fig. 3.26 I_C - V_{CE} characteristics of a typical device in group II for various gamma doses.

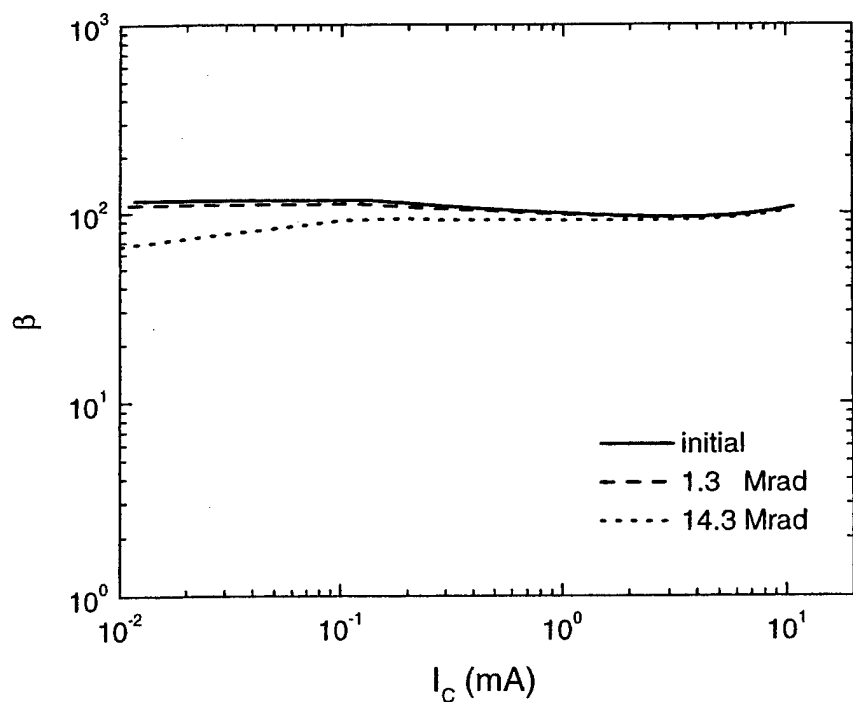


Fig. 3.27 Collector current dependence of DC current gain of a typical group II device.

understood at this time. It is most likely related to the ionization damage in the polyimide and the subsequent trapping of the charges at the defects near the polyimide-semiconductor interface. This in turn causes a surface channel to be formed at the mesa edges of the device through which the leakage current can flow.

The remaining-twenty percent of the devices that belong to the third group behaved somewhat similarly to the second group in that the degradation occurred suddenly after a certain dose. However, the degradation was not as severe, so that the devices did not fail catastrophically. Subsequent to the sudden degradation, these devices did not show much further deterioration for higher doses. The Gummel plots of I_B and I_C for this group of devices are shown in Fig. 3.28. The common-emitter I_C - V_{CE} characteristics measured at a base current of $40\mu\text{A}$ are shown in Fig. 3.29. The physical mechanism of degradation is believed to be the same as that of the second group. Only the extent of degradation is less severe leading to only a partial "failure" of the device. The evolution of the cumulative percentage of the devices in the groups II and III with gamma radiation dose is shown by the histograms in Fig. 3.30.

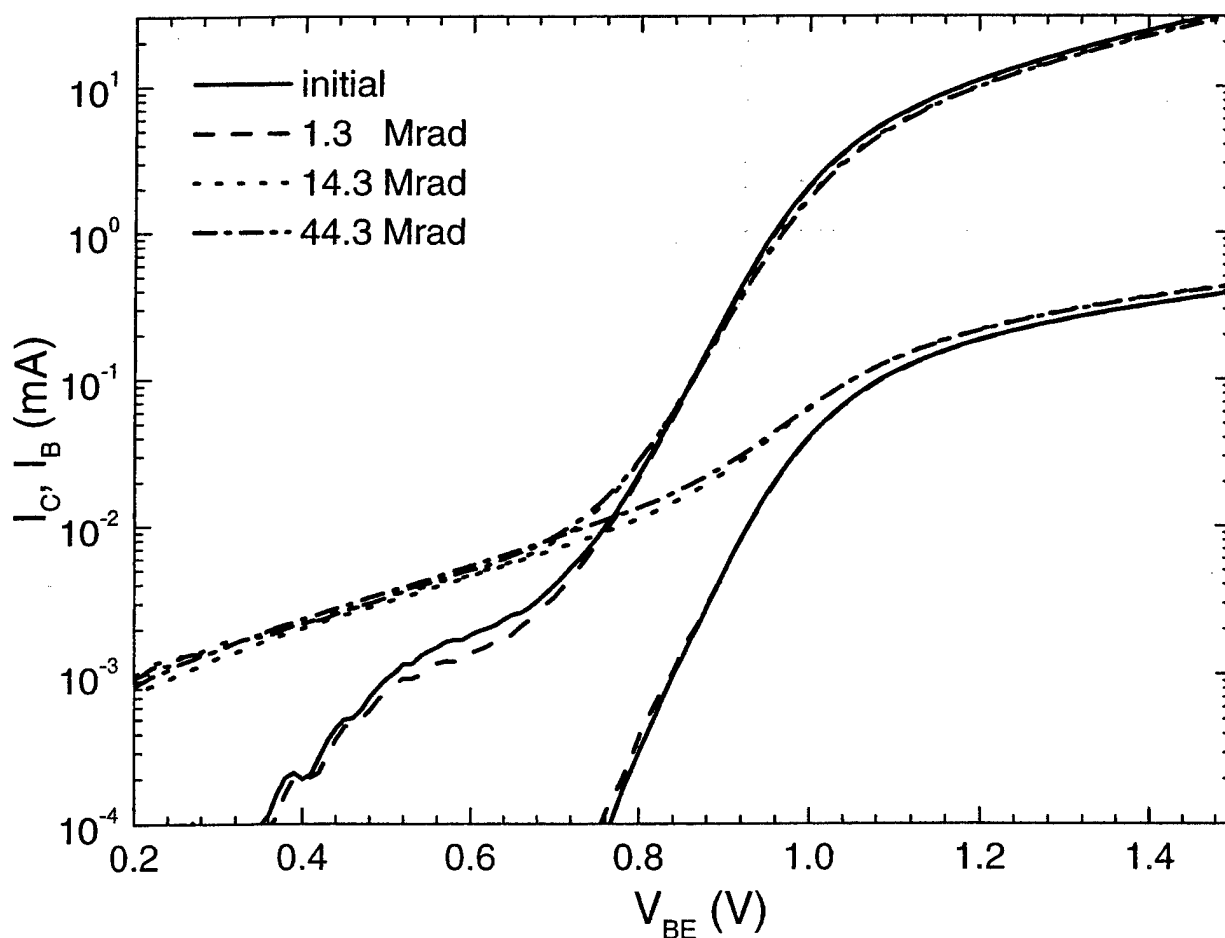


Fig. 3.28 Gummel plots of a typical device in group III for various doses

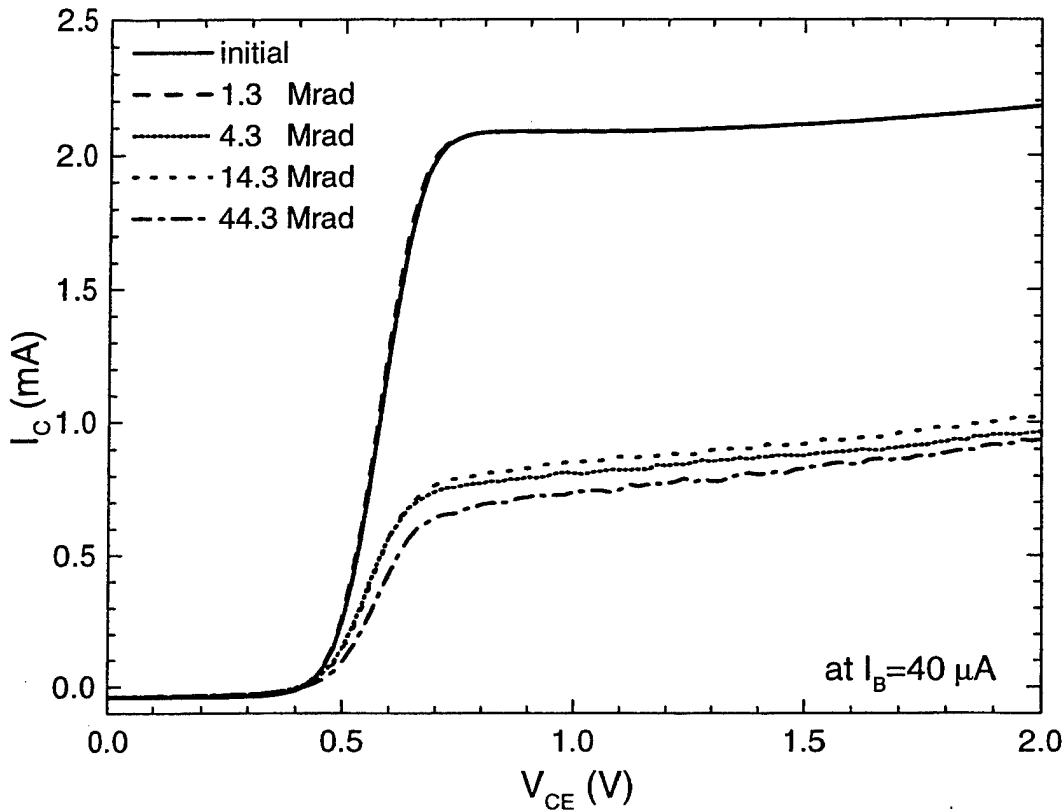


Fig. 3.29 I_C - V_{CE} characteristics of a typical device in group III for various gamma doses.

Radiation-hard Metallization Schemes

Finally to conclude this section, we present some results of our investigation of the gamma radiation effects on different metallization schemes. Gamma irradiation studies on InAlAs/InGaAs SHBTs reported by Witmer et al. [3.7] also showed a catastrophic failure of a certain fraction of the devices. The nature of failure in this case was reported to be an open-device between the emitter and the collector terminals after the gamma irradiation. This failure was attributed to the deterioration of contacts resulting from the lift-off of the contact metals as evidenced by the debris around the contact metals after irradiation. The failure mechanism in our devices was always related to the excess leakage currents causing loss of transistor action. The contact metallization consisting of 500 Å of Ti followed by 1200 Å of Au showed only very little signs of deterioration even after the highest dose. However, we have observed contact metal deterioration and the debris around the metals after gamma irradiation similar to the observation of Witmer et. al. when we used a thin layer of Ti (100-Å) followed by 1200 Å of Au. In a search for a reliable radiation-hard metallization scheme a number of different metal systems was tested. The results of these tests are summarized below.

- Au contacts offer very low resistivity and good stability, but adhere to the substrates very poorly.
- Ti/Au (150/1000 Å) metallization employs thin layer of Ti as an adhesion promoter. This, however, increases resistivity and makes the contact unstable if exposed to gamma radiation or elevated temperatures

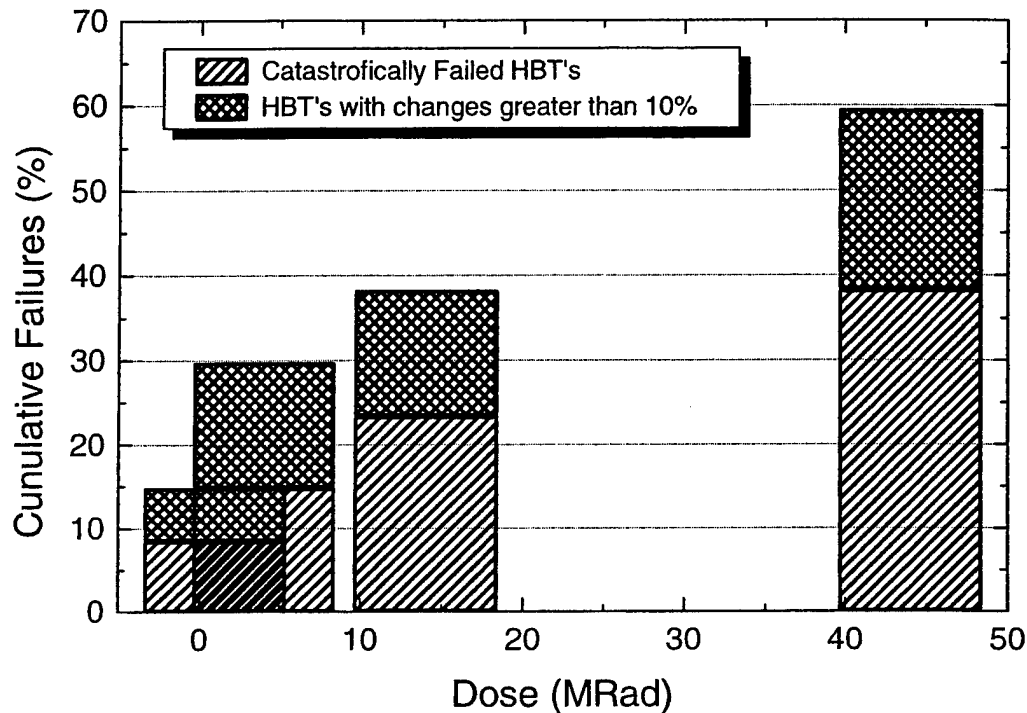


Fig. 30 Evolution of percentage failure in different groups as a function of gamma dose.

- In Ti/Au (1000/1000 Å) films thick Ti layer is used to eliminate the stability problems by further sacrificing conductivity of the contact.
- Alternatively thin layer of Ti can be separated from Au contact layer by a film of low resistive Pd or Pt as done in Ti/Pd/Au (150/500/1000 Å) and Ti/Pt/Au (150/500/1000 Å) schemes, respectively. These films exhibit very good adhesion, relatively low resistivity and are very stable under irradiation. Both schemes offer the comparable characteristics. However, very high temperatures needed for evaporation of Pt make PVD of Ti/Pt/Au (150/500/1000 Å) contacts very difficult.
- In Pd/Au (1000/1000 Å) films to further reduce resistivity adhesion-promoting Ti layer is removed entirely. The films still offer acceptable adhesion, are much easier to deposit and are very stable under irradiation.
- Ni/AuGe(100/1000 Å) annealed scheme can be used to produce low resistivity, stable contacts on n-type GaAs and InGaAs. It was also shown to form a good ohmic contact on n-type InP layers. Ni/AuGe can not however be used to contact p-type layers Ni/AuZn must be used instead) sometimes making the fabrication sequence more complex.

- Finally, in Ni/Au (150/1000 Å) contacts a thin layer of Ni is used as a wetting agent instead of Ti. The films, however, degrade rapidly under irradiation stress and therefore can not be used for device fabrication in our studies.
- The optimum contact metal schemes for smaller contact resistance and no degradation after gamma irradiation are found to be annealed Ni/AuGe for emitter/collector contacts, Pd/Au for the base layer and Ti/Pd/Au for the final metallization performed on top of a passivation layer.

SECTION 4

Radiation Effects in AlGaAs/GaAs Heterojunction Bipolar Transistors

In this section we present some results and discussion of our investigation of electron irradiation effects in AlGaAs/GaAs HBTs. The complete fabrication of these devices including the growth of the structures by molecular beam epitaxy was done at OSU. The details of the fabrication scheme are described in Ref. 4.1. The electron irradiation was performed at OSU Radiation Center using the $^{90}\text{Sr}/^{90}\text{Y}$ described earlier. Devices of different perimeter/area ratio of the emitter were investigated to separate the bulk and surface effects. The details of the device layout are also described in Ref. 4.1. The results and the discussion of this section are published in Ref. 4.2.

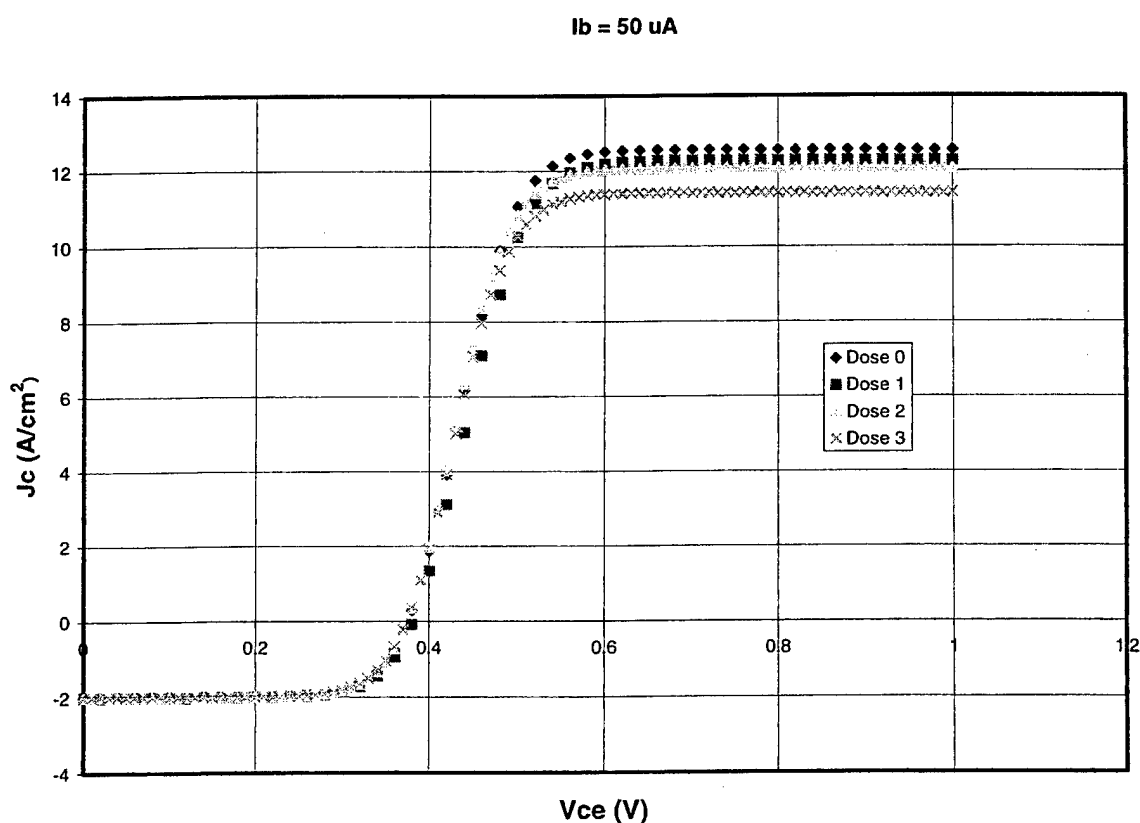


Fig.4.1 J_C - V_{CE} characteristics of a typical device (D5H7) after different electron doses for $I_B = 50 \mu\text{A}$. Dose 0 = Unirradiated; Dose 1 = $1.0 \times 10^{15} \text{ e/cm}^2$; Dose 2 = $3.5 \times 10^{15} \text{ e/cm}^2$, and Dose 3 = $9.2 \times 10^{15} \text{ e/cm}^2$. Emitter area is $50 \times 50 \mu\text{m}^2$.

The common emitter J-V (J_C - V_{CE}) characteristics of a typical device (emitter area $50 \times 50 \mu\text{m}^2$) at a base current of $50 \mu\text{A}$, for different electron doses are shown in Fig. 4.1. The only significant change noticed from these plots is the reduction in the collector saturation current

density ($J_{C,sat}$) with increasing electron dose. No significant change after irradiation is observed in the offset voltage ($V_{CE,off}$) at which the collector current crosses zero, in the collector voltage at which the current begins to saturate ($V_{CE,sat}$) and in the collector output conductance ($g_c = \Delta I_C / \Delta V_{CE}$). Reduction in the collector current implies a degradation of the common emitter current gain ($\beta = I_C / I_B$). The changes in the values of β caused by a cumulative dose of $9.2 \times 10^{15} \text{ e/cm}^2$ for a few representative devices with different emitter areas are summarized in Table 4.1.

Table 4.1: Summary of gains determined from the J_c - V_c characteristics of different types of devices before and after irradiation of $9.2 \times 10^{15} \text{ e/cm}^2$.

Base thickness	Device i.d.	Area (μm^2)	P/A (μm^{-1})	I_B (μA)	β (pre-rad)	β (post-rad)	$\Delta\beta/\beta(\%)$
600 A	D1H1	50x50	0.08	10	7.56	4.58	-39.4
				50	19.87	17.06	-14.1
1000 A	D5H7	50x50	0.08	10	4.99	4.31	-13.5
				50	6.28	5.58	-8.3
	D3H7	20x50	0.14	10	4.59	3.99	-12.9
				50	5.9	5.53	-6.0
	D2H7	10x50	0.24	10	4.41	4.09	-7.1
				50	5.92	5.72	-3.34
	D4H7	10x20	0.3	10	4.69	4.44	-5.3
				50	6.24	6.16	-1.28

The following observations may be made from Table 4.1.

- (1) Base-thickness dependence: For a given emitter size, the gain of the unirradiated devices decreases with increase in the base thickness. The radiation-induced reduction of the gain is smaller for the larger base thickness device.
- (2) Emitter perimeter/area (P/A) ratio dependence: The radiation-induced reduction in the gain ($\Delta\beta$) is smaller for the larger P/A ratio of the emitter.
- (3) Base current dependence: The gain degradation is more at the smaller base currents than at the larger base currents for all the devices.

The dependence of gain (β) on the electron irradiation dose (ϕ_e) is found to obey the Messenger-Spratt relationship

$$\frac{1}{\beta} = \frac{1}{\beta_0} + K_\beta \phi_e \quad \dots(4.1)$$

as shown in Fig. 4.2. In eq. (4.1), β_0 is the gain of the device prior to irradiation, and K_β is known as the gain degradation coefficient. The observations made earlier from Table 4.1 are further corroborated by the dependence of the gain degradation coefficient on the base thickness, on the base current and on the P/A ratio of the emitter. It is found that K_β decreases with increase in the base thickness as shown in Fig. 4.3, and it decreases with increasing P/A ratio as shown in Fig. 4.4. The base current dependence of K_β is clearly seen in both Figs. 4.3 and 4.4. The value of K_β is always larger for the smaller base current (10 μA) than for the larger base current (50 μA), for all the devices studied.

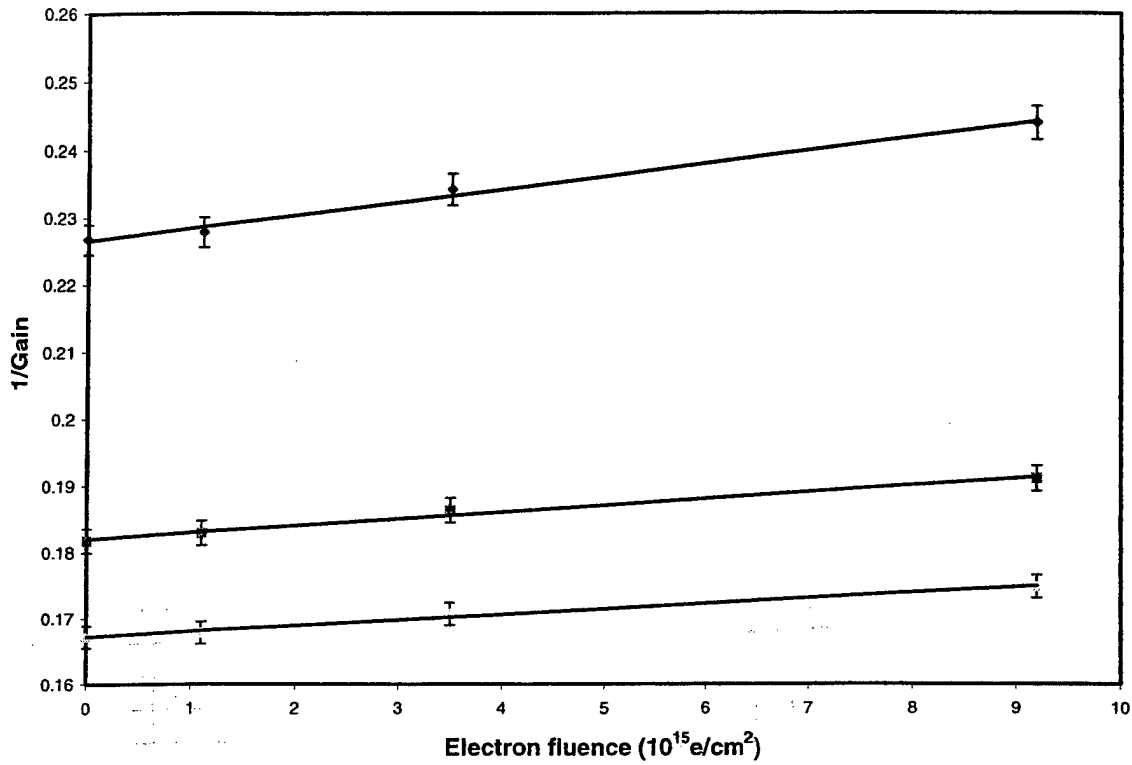


Fig. 4.2 Electron irradiation dose dependence of reciprocal gain at three different base currents. Diamonds: $I_B = 10 \mu\text{A}$, squares: $I_B = 30 \mu\text{A}$, and triangles: $I_B = 50 \mu\text{A}$. The straight lines are linear fits.

In order to understand the gain degradation mechanisms, it is important to consider the relative contributions of the different components of the base current. To this end, we have carried out Gummel plot measurements of J_B and J_C as functions of V_{BE} for $V_{BC} = 0$. The measured Gummel plots of a typical device before and after irradiation are shown in Fig. 4.5. It is seen that the collector current is nearly the same before and after irradiation.

The dependence of the collector current density (J_C) on V_{BE} may be written as

$$J_C = J_{C0} \exp(qV_{BE} / mkT). \quad \dots(4.2)$$

For a HBT with compositionally graded B-E heterojunction, the collector current ideality factor, m , is expected to be close to unity. Indeed, the fit of our measured collector current Gummel plot ($\ln(J_C)$ vs. V_{BE}) to eq. 4.2 gives values of m in the range from 1.0 to 1.2 and they are not significantly affected by radiation. The collector current in a HBT is determined by thermionic

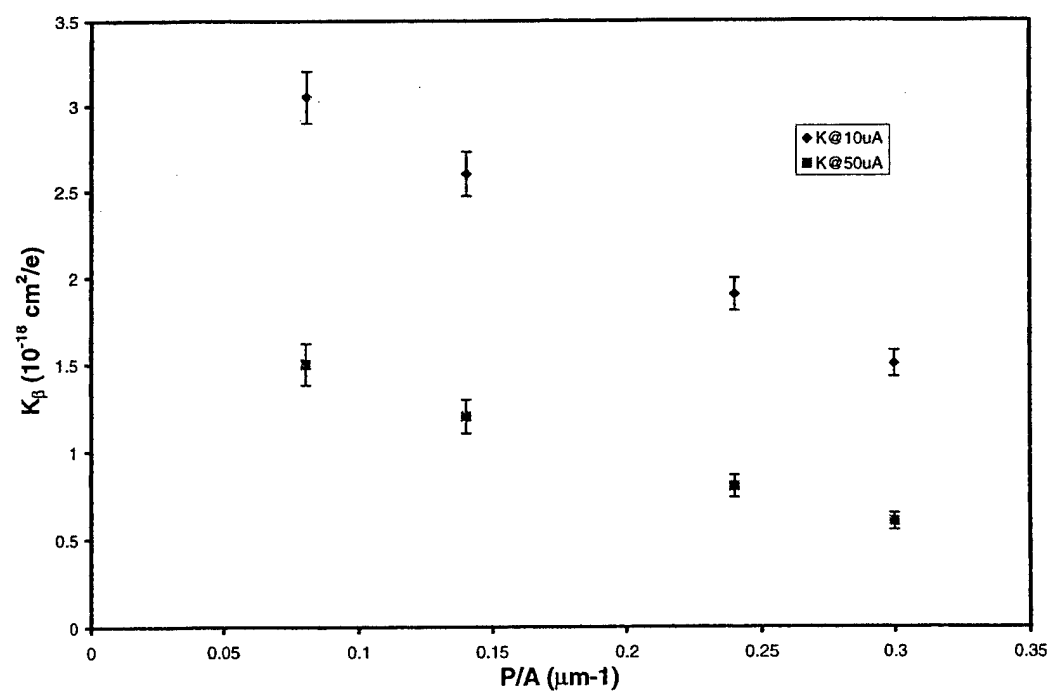
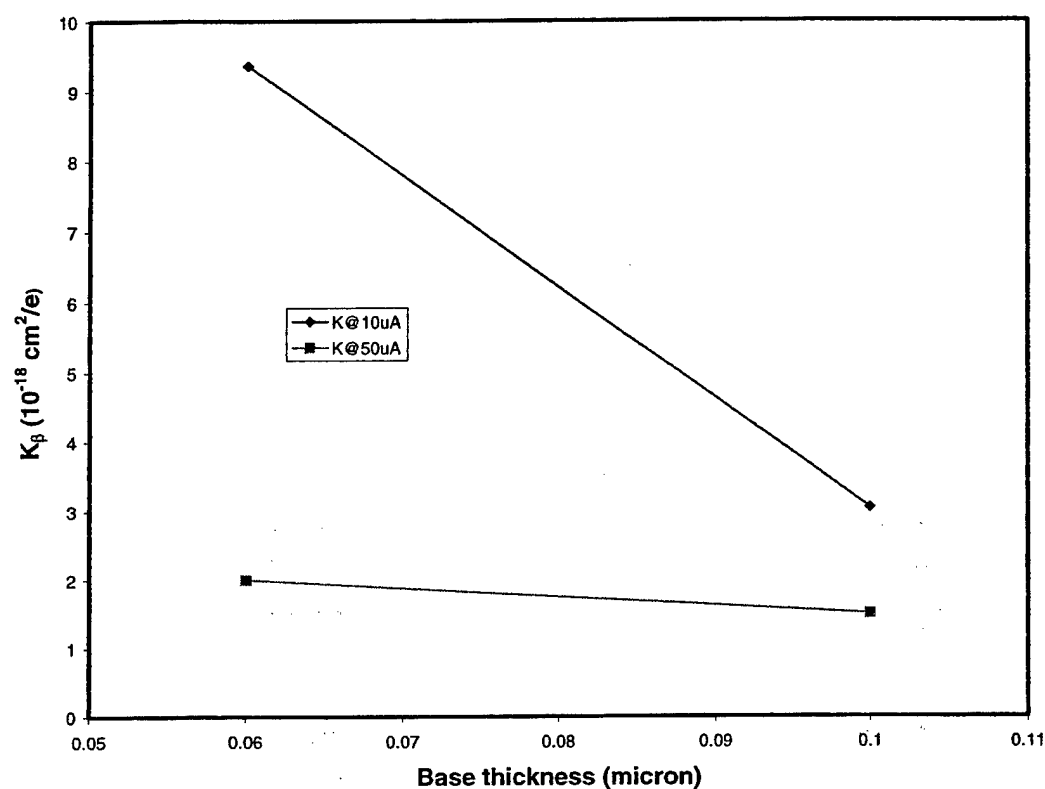


Fig. 4.3 (Top) Base thickness dependence of the gain degradation coefficient K_β for two different values of I_B . Fig. 4.4 (Bottom): P/A dependence of K_β .

emission at the B-E junction followed by diffusion across the base [4.3]. The absence of any change in the collector current density for a given V_{BE} suggests that the collector current transport is unaffected by electron irradiation. The saturation of J_C in the high V_{BE} regime ($V_{BE} > 1.2$ V) is due to the series resistance effects.

The base current, on the other hand, shows an increase after irradiation as seen in Fig.

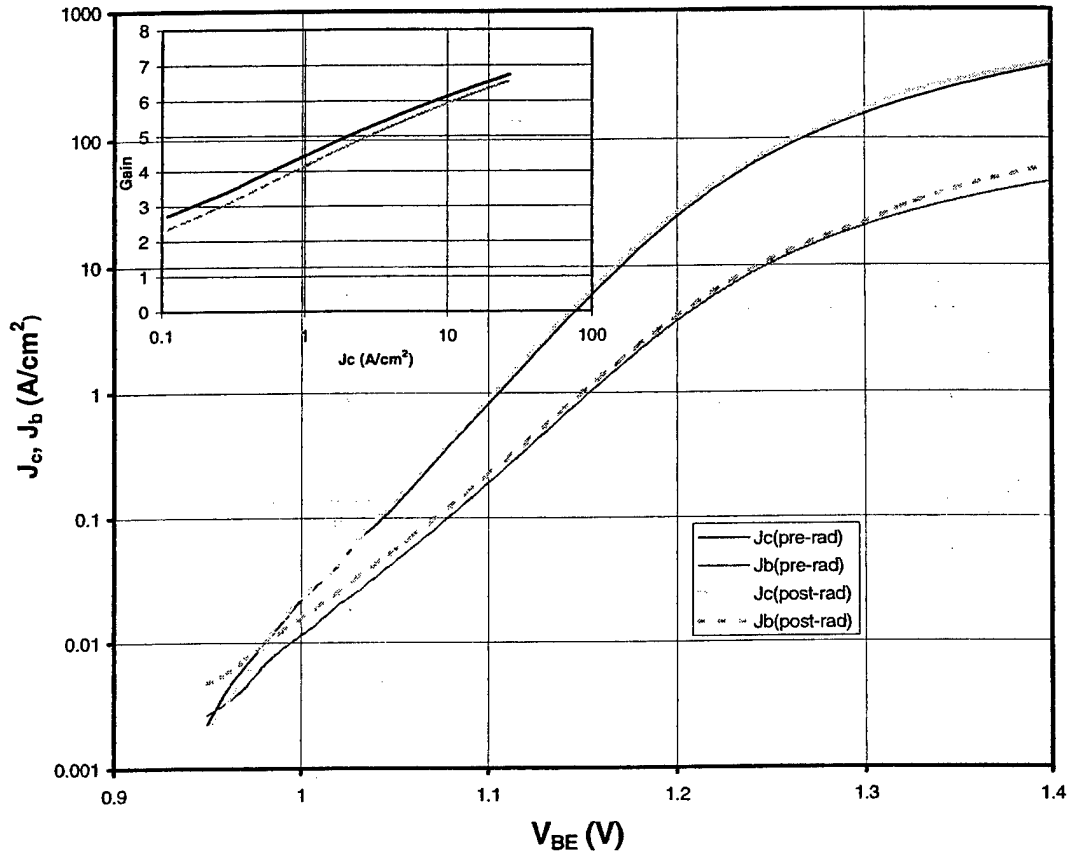


Fig. 4.5 Gummel plots of the collector current density J_C , and base current density J_B at $V_{BC} = 0$ for a typical device before and after irradiation with $9.2 \times 10^{15} \text{ e/cm}^2$. Emitter area is $50 \times 50 \mu\text{m}^2$. The inset shows the collector current dependence of gain determined from the Gummel plot.

4.5. The increase in the base current is responsible for the gain degradation. The base current in a HBT consists of the following components. (1) J_{SCR} , the bulk recombination current in the B-E junction space charge region (SCR) with an ideality factor ~ 2.0 ; (2) $J_{S,SCR}$, the surface recombination current at the periphery of the B-E junction depletion region with an ideality factor ~ 2.0 [4.4]; (3) J_{BD} , the diffusion/recombination current in the bulk quasi-neutral base region with an ideality factor ~ 1.0 ; and (4) $J_{B,surf}$, the surface recombination current at the extrinsic base region with an ideality factor ~ 1.0 [4.5]. Thus the dependence of J_B on V_{BE} may be written as

$$J_B = (J_{BD} + J_{B,surf}) \exp(qV_{BE} / mkT) + (J_{SCR} + J_{S,SCR}) \exp(qV_{BE} / nkT) \quad \dots(4.3)$$

with values of m and n close 1.0 and 2.0, respectively. Normally, the second term in equation 2 is more dominant at smaller V_{BE} (or smaller base currents) and the first term begins to take over at larger values of V_{BE} (or larger base currents). In such a case, the base current Gummel plot, $\ln(J_B)$ vs. V_{BE} , will show two distinct regions with slopes approximately equal to 2 and 1, for the low and the high V_{BE} regimes, respectively. However, depending upon the relative magnitude of the prefactors of the two terms in eq. 3 the above two regimes overlap together and give rise to a single slope with an effective ideality factor, n_{eff} , lying between 1.0 and 2.0. From the value of this effective ideality factor, it is possible to deduce if the junction region components are dominant ($n_{eff} \rightarrow 2.0$) or the quasi-neutral base region components are dominant ($n_{eff} \rightarrow 1.0$). The values of m and n extracted for a few devices, before and after irradiation are summarized in Table 4.2.

Table 4.2 Summary of the extracted ideality factors from the Gummel plots for a few typical devices before and after irradiation

Device i.d.	Dose e/cm ²	m	n
D1H1	0	1.17	2.48
	9.2×10^{15}	1.24	3.28
D5H7	0	1.016	1.35
	9.2×10^{15}	1.04	1.6
D2H7	0	1.03	1.4
	9.2×10^{15}	1.05	1.68

As seen in Fig. 4.5, the radiation-induced change in J_B is more at smaller V_{BE} , and it decreases as V_{BE} increases. As pointed out earlier, the junction SCR component of the base current (2nd term in eq. 3) is more dominant at smaller V_{BE} . Hence our result in Fig. 4.5 suggests that electron irradiation degrades the junction SCR components of the base current more than the neutral base components. Thus the radiation-induced gain degradation is more at smaller base currents or equivalently at smaller collector currents. This result is similar to that observed in the case of InP/InGaAs HBTs presented in Section 3. The collector current density dependence of the gain determined from the Gummel plots before and after irradiation is shown in the inset of Fig. 4.5. In the high V_{BE} regime ($V_{BE} > 1.32$ V) the radiation-induced change in the base current is once again large as evident from Fig. 4.5. We believe that this increase in the base current in the high V_{BE} regime is caused by an increase in the collector series resistance after irradiation. The voltage drop across the collector series resistance forward biases the B-C junction (with external $V_{BC}=0$) giving rise to the additional base current. We have observed a similar effect also in the case of InP/InGaAs HBTs after electron irradiation as discussed in Section 3.2.

The junction SCR component of the base current is further subdivided into two components, the bulk SCR and the surface SCR as noted in eq. 4.3. Which of these two components degrades more by radiation can be learnt from the dependence of gain degradation on the emitter P/A ratio of the devices. However, the collector current density also changes with the change in the emitter size. Hence, the P/A dependence of gain degradation shown in Fig. 4.4 can not be directly used to determine whether the bulk SCR or the surface SCR current degrades more. The P/A dependence of gain at a constant collector current density for a 1000Å base device before and after irradiation is shown in Fig. 4.6. It is seen that the gain decreases with P/A ratio.

This is the so-called emitter size effect and it is well known to be caused by the increased surface recombination in the larger P/A ratio devices [4.6]. It is also seen from Fig. 4.6 that the radiation-induced gain reduction is smaller for the larger P/A devices. This result suggests that

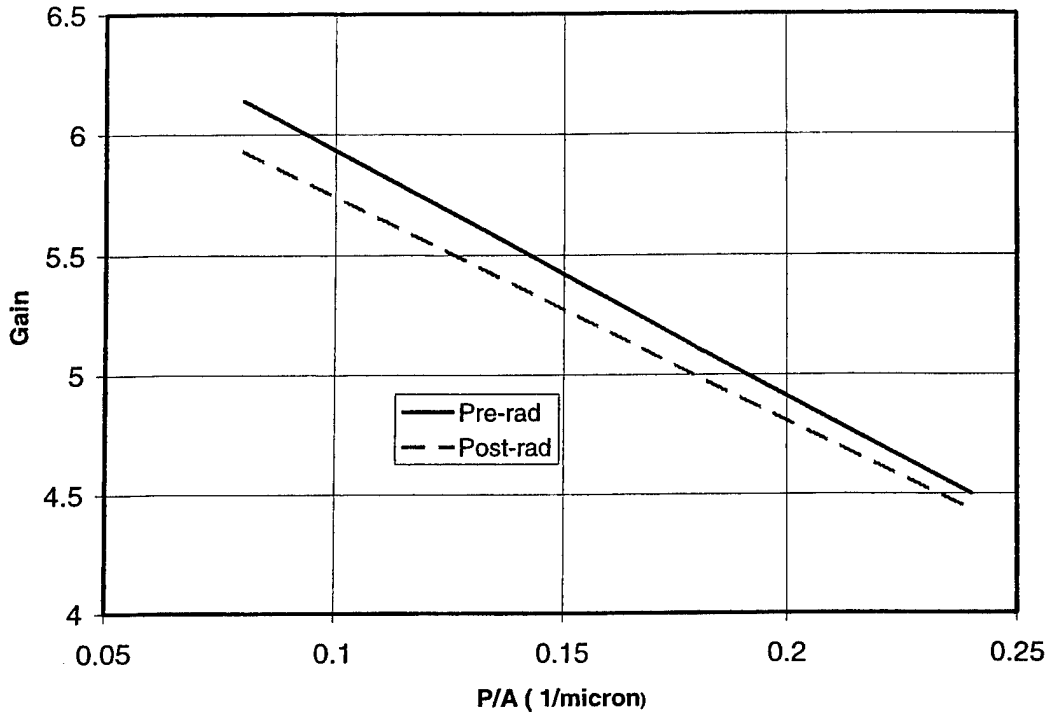


Fig. 6 P/A dependence of gain before and after irradiation with $9.2 \times 10^{15} \text{ e/cm}^2$, at a constant collector current density, $J_C = 10.0 \text{ A/cm}^2$.

the radiation degrades the bulk SCR component more than the surface SCR component. In the smaller P/A (or the larger emitter area) devices, the base current is predominantly due to the bulk SCR recombination and hence the gain degradation is larger. As P/A ratio increases, the relative contribution of the surface recombination current to the base current increases. However, since the surface recombination component is less affected by radiation, the radiation-induced gain degradation is smaller for the larger P/A ratio devices.

Finally, the base thickness dependence of the gain degradation is also consistent with the model that the radiation predominantly affects the junction bulk SCR component of the base current. In the smaller base thickness device (600Å-base) the junction SCR current (2nd term in eq. 4.3) is more dominant since the SCR region occupies a significant part of the base thickness. This is also consistent with the larger base current ideality factor ($n_{\text{eff}} = 2.48$) observed for this device. Furthermore this is a large emitter-size ($50 \times 50 \text{ } \mu\text{m}^2$) and hence the contribution of the surface SCR current would be small. Thus the base current in this device has the largest contribution from the bulk SCR recombination, the principal component that degrades with radiation. Hence the radiation-induced gain degradation is maximum in this device.

As the base thickness is increased (1000Å-base, $50 \times 50 \text{ } \mu\text{m}^2$ emitter), the gain of the unirradiated device decreases. This is easily understood by the decrease of the base transport factor α given by [4.3]

$$\alpha = \frac{1}{\coth\left(\frac{w}{\sqrt{D\tau}}\right)} \quad \dots(4.4)$$

With the increase in base thickness the contribution of the quasi-neutral base region recombination (1st term in eq. 4.2) to the base current also increases. This is also consistent with the smaller base current ideality factor observed in this device ($n = 1.35$). Since the neutral base recombination component of the base current does not degrade significantly with radiation, the overall gain degradation is smaller.

We will now discuss why radiation affects the junction bulk SCR component of the base current more than the other components. The junction SCR current arises from the recombination at the deep level defects by the conventional SRH mechanism [4.7]. Clearly the radiation introduced defects in the B-E junction region are responsible for the increase in the junction SCR recombination current. Ideality factors greater than 2.0 observed in some (e.g. 600Å – base) devices may be associated with recombination involving distributed centers rather than a single discrete level and/or tunneling assisted recombination [4.8].

The neutral bulk recombination in the base region of a HBT predominantly takes place via radiative recombination and Auger recombination. The radiative recombination rate is proportional to the product (pn) of the hole and electron concentration in the base. The Auger recombination rate goes as pn^2 or np^2 . Since the base region of a HBT is typically very heavily doped ($\sim 10^{19} \text{ cm}^{-3}$) the radiation induced defects do not significantly affect the carrier concentrations in the base. Our independent experiments by using Hall measurements on control samples with carrier concentration similar to that of the base layer show that the change in base carrier concentration is indeed negligible even at the highest levels of electron irradiation dose used in our experiments. This justifies our assumption that the neutral base recombination is not affected by the radiation in our experiments.

The surface recombination current in HBTs has been extensively investigated in the literature [4.4, 4.5]. It is clear from these studies that the surface recombination is controlled by the Fermi level pinning at the surface of the semiconductor. It is well known that the large density of intrinsic defects at the surface of III-V compound-semiconductors cause a strong Fermi level pinning. In the case of passivated devices, the concentration of the radiation-induced defects at the surface is probably much less than the intrinsic defect concentration at the surface and hence the Fermi level pinning is not significantly affected. Therefore, the surface recombination current is also not significantly affected by radiation.

The results of our present study are in complete agreement with the results of investigation of neutron irradiation induced degradation of AlGaAs/GaAs HBTs by Song *et al* [4.9] that showed that the low gain devices degraded less than the high gain devices. This result was explained by arguing that the base current of the low gain devices has more surface recombination component and that the surface recombination current is not affected by radiation. Our present study also implies the same result that the low gain devices degrade less. We have further investigated this result by identifying the roles of the different components of the base current on the degradation of the current gains of HBTs having different base thickness and P/A ratios of the emitter. Our results suggest that the electron irradiation affects only the junction SCR recombination and that it has negligible effect on the surface recombination and the quasi-neutral base recombination currents in polyimide-passivated HBTs.

We now give a brief discussion of the possible implications of our results on the radiation-hard- design issues for AlGaAs/GaAs HBTs and circuits using them. Our experimental result on the base-thickness dependence of the gain degradation suggests that there is a trade-off between increasing gain prior-to-irradiation and increasing radiation-induced-gain-degradation as the base thickness is reduced. Radiation-hard HBT design should carefully take this trade-off into account. Secondly, smaller emitter-size (larger P/A) devices undergo less degradation and hence it is advantageous to use smaller size devices in radiation-hard circuit design. Finally, our results on the base current dependence of gain degradation suggest that circuit designs with larger base current bias would suffer less degradation in radiation environment.

CONCLUSIONS

In this section, we have investigated the electron irradiation effects on polyimide passivated AlGaAs/GaAs HBTs of different base thickness and different emitter sizes. Our results show that the electron irradiation induced gain degradation of the passivated AlGaAs/GaAs HBTs decreases with (1) increase in the base thickness (2) increase in the perimeter to area ratio of the emitter and (3) increase in the base current. These results suggest that the gain degradation due to electron irradiation is mainly caused by an increase in the emitter-base junction space charge region recombination. The influence of electron radiation on the quasi-neutral base recombination and the surface recombination currents appear to be negligible.

5. Radiation Effects in High Electron Mobility Transistor Structures and Devices

AlGaAs/GaAs High Electron Mobility Transistors (HEMTs) are extensively used in low noise microwave amplifiers and high-speed digital circuits in space based systems. Hence the radiation sensitivity of these devices is an important concern. We have carried out extensive investigations on both the basic device structures and finished devices to study the radiation degradation of material parameters and their influence on the devices performance. In section 5.1, we describe a method to characterize the radiation effects in single heterojunctions by C-V measurements. In section 5.2, we describe the radiation effects in single quantum wells characterized by C-V and photoluminescence measurements. Radiation effects on transport properties (mobility and carrier concentrations) of two-dimensional electron gas (2-DEG) in HEMT structures are discussed in Section 5.3. Finally, the radiation effects in actual HEMT devices are described in Section 5.4.

5.1 Gamma radiation effects in n-N isotype GaAs/AlGaAs heterojunctions

The main objective of this experiment was to investigate the influence of gamma radiation on the integrity of heterojunction interfaces which constitute the basic components of many modern devices. Gamma radiation is an ionizing radiation and is very penetrating. Silicon devices suffer considerable damage due to ionizing radiation because of the charge build-up in the oxide layer. This type of damage is absent in the case of III-V devices since they do not generally have an oxide layer as an intrinsic part of the device. However, gamma radiation can also cause permanent displacement damage through the Compton electrons generated during the primary interaction of the gamma photon with the material. The object of the experiment was to determine if the displacement damage in the neighborhood of the heterojunction interface would cause interdiffusion of the chemically dissimilar atoms on the two sides of the interface and thereby give rise to a slight smearing of the heterointerface. It may be noted that the interdiffusion by a few monolayers on both sides is adequate to cause sufficient smearing of the interface that can significantly affect device performance.

The effect of gamma radiation on the band offset and the defect density at the heterointerface was studied by C-V measurement using Kroemer's method. In this method, a Schottky barrier is placed parallel to the heterojunction interface at an appropriate distance from the heterojunction plane. The depletion region of the Schottky barrier is swept through the heterojunction region by varying the reverse bias on the Schottky barrier. The band offset and the

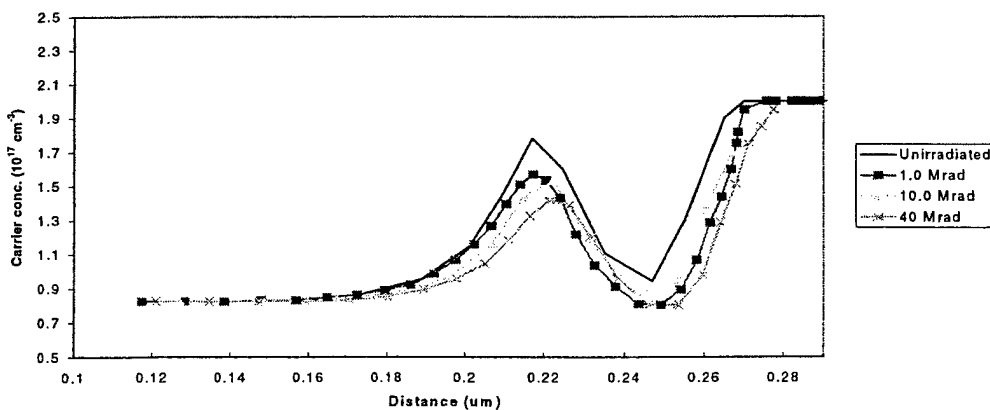


Fig. 5.1 Measured carrier concentration profiles of GaAs/AlGaAs heterojunction after different gamma exposure.

interface defect density are determined by an analysis of the measured (apparent) carrier concentration profiles shown in Fig. 5.1. Our analysis shows that the band offset values are not affected at all, within experimental errors, even after 40 Mrad of gamma radiation. The only effect of radiation is found to be a slight change in the interface defect density from $\sim 1.0 \times 10^{11} \text{ cm}^{-2}$ to $\sim 2.0 \times 10^{11} \text{ cm}^{-2}$. Thus, it is concluded that there is no significant interdiffusion at the GaAs/AlGaAs interface after 40 Mrad of gamma radiation and that the radiation induced interface defect density is $\sim 1.0 \times 10^{11} \text{ cm}^{-2}$.

5.2 Gamma radiation effects in GaAs/InGaAs/GaAs strained quantum wells

Strained InGaAs quantum wells play an important role in pseudomorphic High Electron Mobility Transistors (p-HEMT). The idea of this experiment was to investigate if the strain plays a role in promoting interdiffusion during radiation. The experiment is very similar to the one described in Section 5.1. However, in this case there is no simple analysis (as in Kroemer's method) available to determine the band offset. The measured carrier profiles were compared

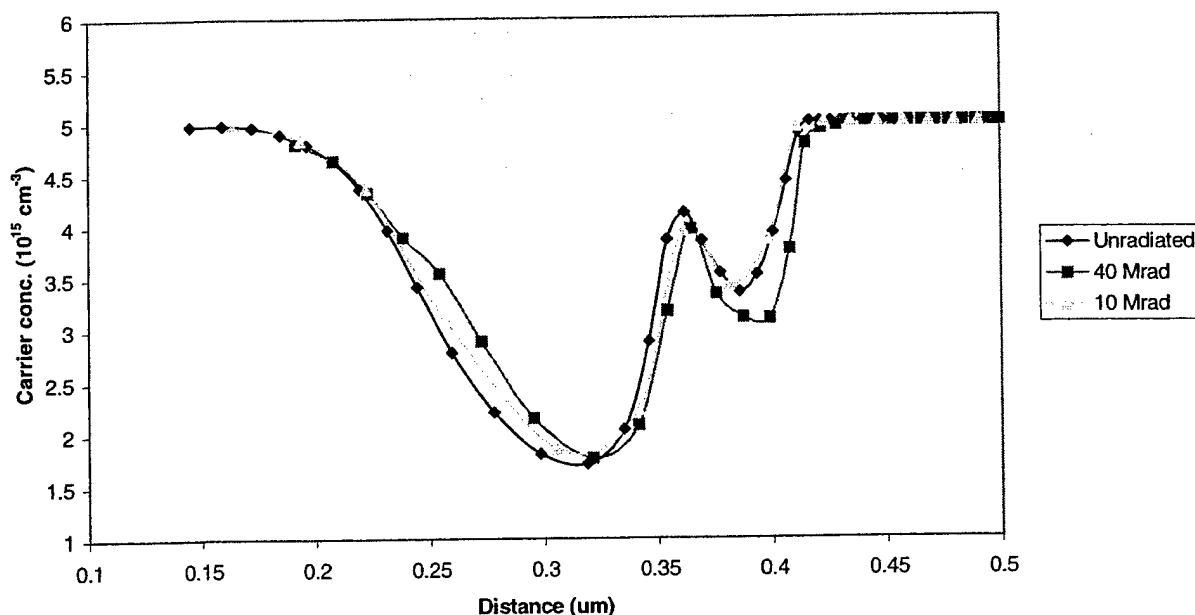


Figure 5.2 Measured carrier concentration profiles of GaAs/InGaAs/GaAs quantum well after different gamma exposure.

with the theoretically simulated carrier profiles to determine the band offset values. The measured carrier concentration profiles before and after gamma radiation are shown in Figure 5.2. It is seen that the measured carrier profiles are asymmetric with respect to the peak carrier concentration at the center of the well. Our theoretical simulation shows that this asymmetry arises from a nonuniform In concentration along the direction normal to the heterojunction interfaces. We believe that this nonuniform In distribution in the unirradiated sample is caused by the surface segregation of In during the molecular beam epitaxy growth. The carrier concentration profile after 40 Mrad of gamma radiation is seen to be more symmetric than that of the unirradiated sample. Thus, it appears that In redistributes during the irradiation so as to reduce the original In

concentration gradient. Radiation enhanced diffusion mechanism in which the energy released by electron hole pair recombination aids the diffusion process is believed to be responsible for the redistribution of In at such low temperatures ($< 100^\circ\text{C}$) during irradiation. The results of these studies have been published in Ref. 5.1.

5.3 Radiation effects on the transport properties of modulation doped AlGaAs/GaAs heterostructures

A. Gamma radiation effects

Hall effect measurements were performed to determine the mobility and carrier concentration of 2-dimensional electron gas (2-DEG) in modulation doped AlGaAs/GaAs heterostructures before irradiation and after several doses of gamma radiation up to a cumulative dose of 40 Mrad. To investigate if a surface passivation layer has any influence in minimizing the radiation damage, some samples were covered with a layer of 2000 Å thick SiO_2 deposited by Plasma Enhanced Chemical Vapor Deposition (PECVD) process before exposing the samples to gamma radiation. Hall measurements were performed before and after the PECVD process and it was found that the PECVD process did not have any influence on the transport properties of these samples.

The dependence of normalized mobility at 300 K on the gamma radiation dose is shown in Figure 5.3 for a few samples with and without the SiO_2 passivation layer.

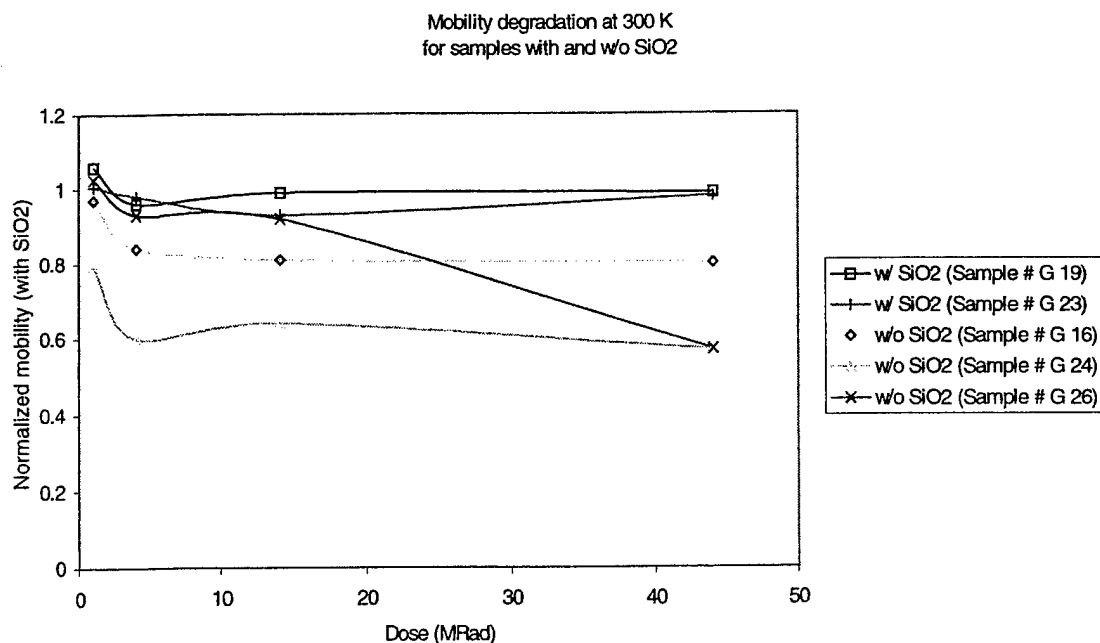


Figure 5.3 Normalized mobility at 300 K of modulation doped GaAs/AlGaAs heterostructures with and without SiO_2 passivation as function of gamma radiation dose.

It is clearly seen that while the samples without SiO_2 passivation layer show a degradation of mobility, the passivated samples show much less degradation. A similar difference in 77K

mobility degradation between the unpassivated and the passivated samples is evident from Fig. 5.4.

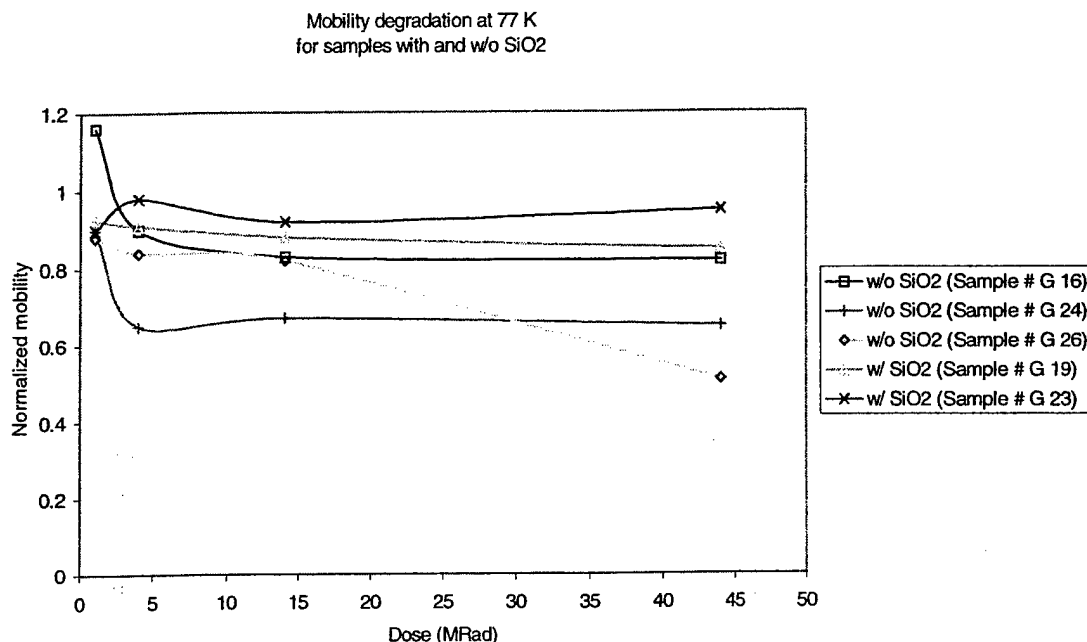


Figure 5.4 Normalized mobility at 77 K of modulation doped GaAs/AlGaAs heterostructures with and without SiO₂ passivation as a function of gamma radiation dose.

From these results, it is clear that mobility degradation of the unpassivated samples is much more than that of the passivated samples. It is surprising how a thin (2000 Å) layer of SiO₂ can offer protection against gamma ray induced damage since one would expect gamma rays to easily go through such a thin layer of SiO₂ without much absorption. If the mobility degradation is due to bulk displacement damage in the vicinity of the 2-DEG layer, one would expect the damage to be similar in both types of samples since the number of Compton electrons causing the displacement damage near the 2-DEG layer should be same in both the cases.

We propose the following mechanism to explain the difference in mobility degradation between the passivated and the unpassivated samples. We believe that the main difference between the two types of samples is the presence of the 'free surface' of the semiconductor very close (about 500 Å) to the 2-DEG channel in the case of unpassivated samples. We believe that the defects generated near the surface region can move toward the channel region by the phenomenon of 'recombination enhanced diffusion' well documented for silicon. In this phenomenon, the diffusion of defects is enhanced by orders of magnitude due to the energy released by the electron-hole pair recombination in the neighborhood of the defects.

The above results have also been published in Ref. 5.1

B. Neutron Radiation Effects in modulation doped AlGaAs/GaAs heterostructures

Neutron radiation of the modulation doped AlGaAs/GaAs heterostructures were performed using the OSU TRIGA nuclear reactor facility in the fluence range from 10^{14} cm⁻² to

10^{16} cm^{-2} . The damage was characterized by transport (Hall effect) and photoluminescence measurements.

The normalized values of 300 K mobility and carrier concentration as functions of neutron dose are plotted in Figure 5.5. The normalized 77 K mobility and carrier concentrations are shown in Figure 5.6.

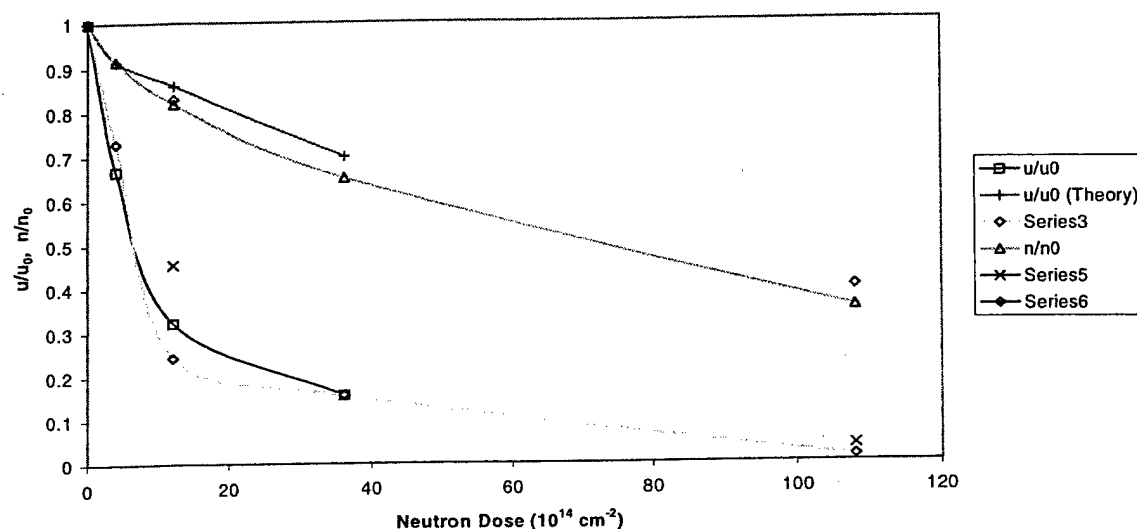


Figure 5.5 Normalized mobility and carrier concentration at 300 K as functions of neutron dose for different GaAs/AlGaAs modulation doped heterostructures.

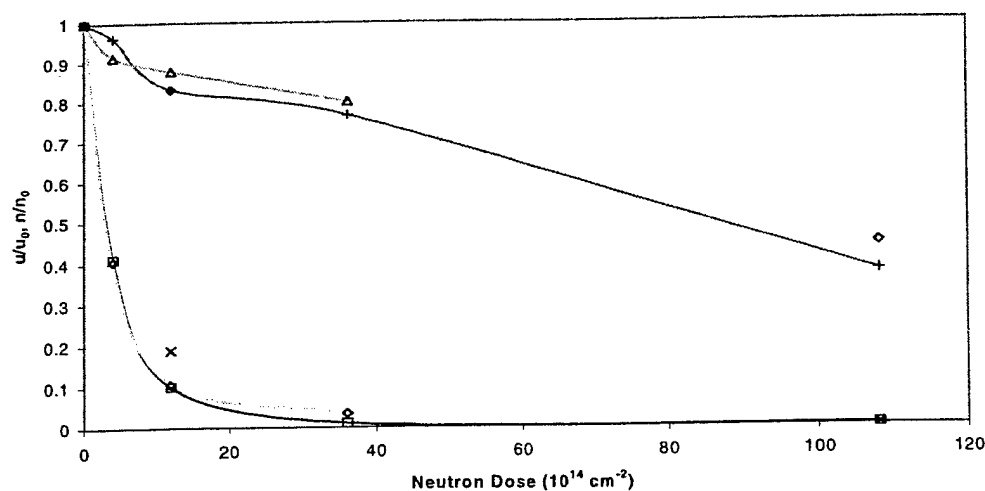


Figure 5.6 Normalized mobility and carrier concentration at 77 K as functions of neutron dose for different GaAs/AlGaAs modulation doped heterostructures.

A mobility analysis including various scattering mechanisms was performed to study the neutron induced damage more quantitatively. Our analysis shows that the dominant mechanism limiting the mobility at 77K is the ionized impurity scattering in the buffer layer (near the 2-DEG channel) and the remote impurity scattering from the impurities in the spacer layer. Hence, the

mobility degradation is believed to be due to the neutron radiation induced defects in these two layers. The net concentration of defects introduced in these two layers (assumed to be equal) as determined from our analysis is plotted as a function of neutron dose in Figure 5.7. The net

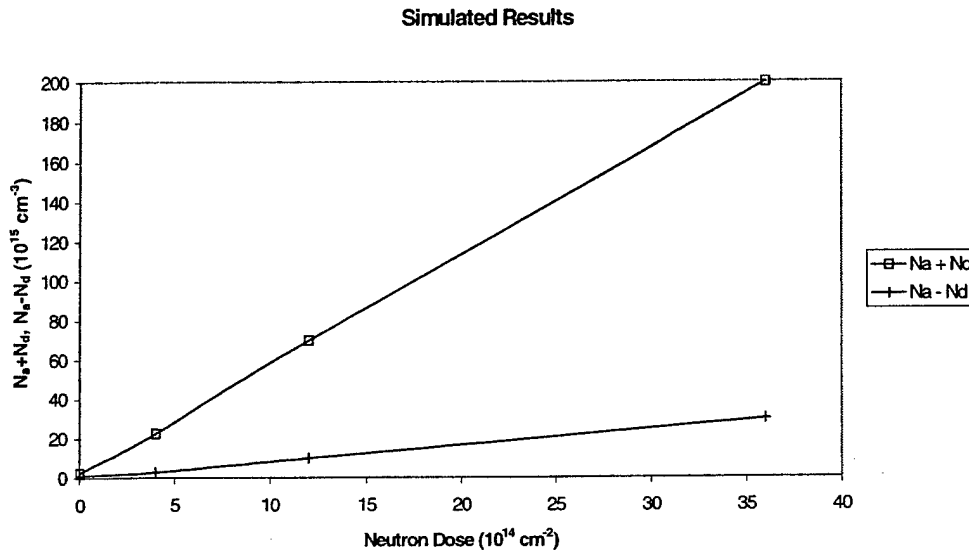


Figure 5.7 Total defect concentration and the net acceptor concentration in the GaAs buffer layer as function of neutron dose.

introduction rate of defects (donor + acceptor) from the slope of this line is found to be 50 cm^{-1} . This is slightly larger than the reported introduction rate of defects in neutron irradiated bulk GaAs. This discrepancy may be related to the fact that the defect concentration obtained from our analysis is for a narrow region close to the 2-DEG channel region whereas the concentration of defects reported for the bulk samples in the literature is an average over a much larger thickness (several microns) of the samples.

The change in carrier concentration of the 2-DEG was analyzed by a self consistent solution of Poisson - Schrodinger equations. Our analysis shows that the change in carrier concentration is related to the increase in the net acceptor like traps introduced by neutron irradiation in the buffer layer. This causes the Fermi level at the heterojunction interface to move toward valence band which in turn results in a decrease of 2-DEG concentration. The net acceptor concentration ($N_A - N_D$) in the buffer layer as a function of neutron dose is also plotted in Figure 5.7.

The photoluminescence spectra of one of the samples is shown in Figure 5.8 after various doses of neutron irradiation. The PL intensity is found to decrease steadily with increasing neutron dose. For the highest dose, the PL intensity was too low to be measured by our detection system. The main PL line arises from a transition from the 2-DEG to the photogenerated holes in the buffer GaAs in the vicinity of the 2-DEG. The decrease in PL intensity is due to the defects introduced by neutron irradiation in the vicinity of the 2-DEG region acting as non-radiative recombination centers. In addition to the decrease in PL intensity, the width (FWHM) of the PL line is also found to increase slightly with increasing neutron dose (from $\sim 2.5 \text{ meV}$ to $\sim 5.0 \text{ meV}$). This increase in PL linewidth is an indication of the possibility of slight compositional smearing of the heterointerface after neutron irradiation.

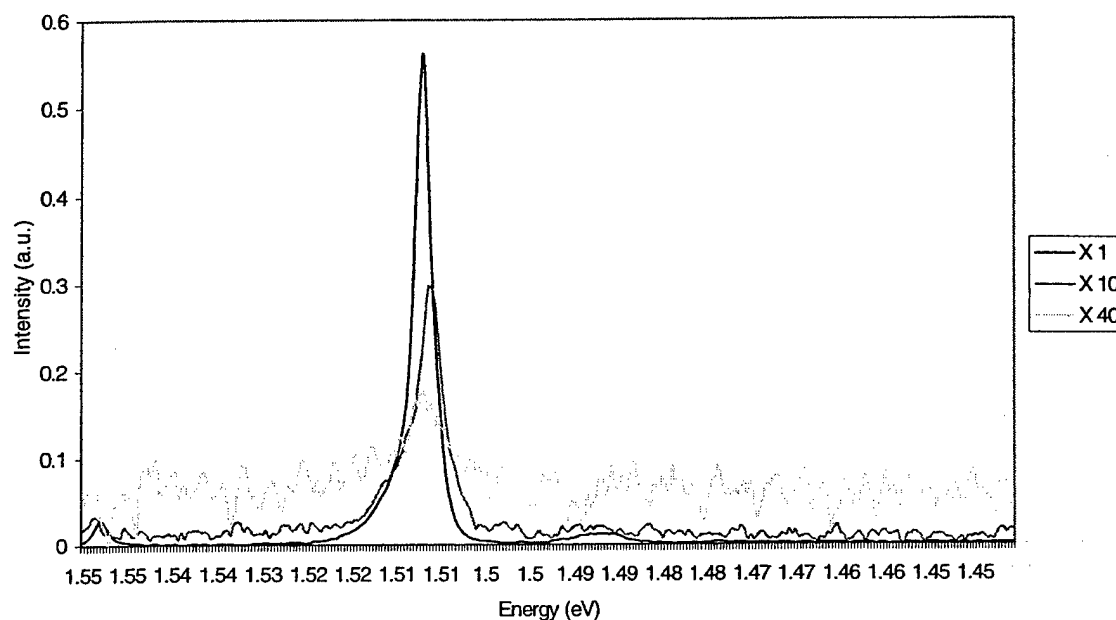


Figure 5.8 Low temperature (10K) PL spectra of neutron irradiated GaAs/AlGaAs modulation doped samples. X1: Dose = 4.0×10^{14} n/cm², x10: Dose = 1.2×10^{15} n/cm², x40: Dose = 3.6×10^{15} n/cm².

5.4 Electron Radiation Effects in HEMT Devices

Samples for this study were grown in house using the OSU MBE facility. The complete fabrication of the devices was also done at OSU. Devices with gate lengths in the range from 5 to 20 microns and widths in the range from 75 to 125 microns were fabricated. Both uniformly doped HEMTs and δ -doped HEMTs were investigated. Results were similar for both types of devices. Details of device fabrication are detailed in Ref. 5.2. Results for the δ -doped device are discussed below.

The drain current versus drain voltage (I_{DS} vs. V_{DS}) characteristics of a typical δ -doped device for different gate voltages (V_{GS}) before irradiation and after a dose of 9.6×10^{15} e/cm² are shown in Figures 5.9a and 5.9b, respectively.

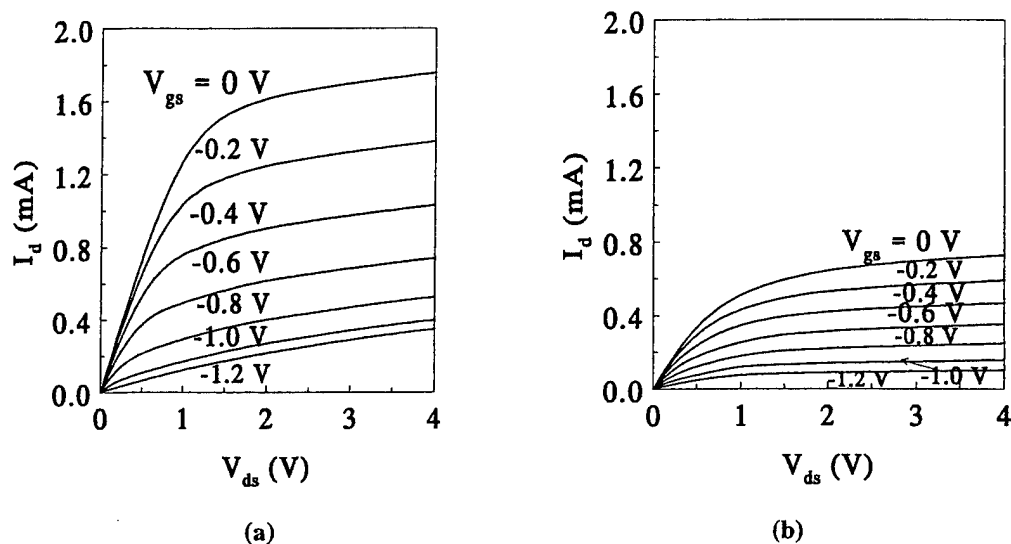


Figure 5.9 I_{DS} - V_{DS} characteristics of a δ -doped device. (a) Unirradiated (b) After a dose of $9.6 \times 10^{15} \text{ e/cm}^2$.

The reduction in drain saturation current (I_{DSS}) at a given V_{GS} caused by radiation damage is evident. The I_{DS} vs. V_{DS} characteristics of the device at a fixed V_{GS} for different electron doses are shown in Figure 5.10.

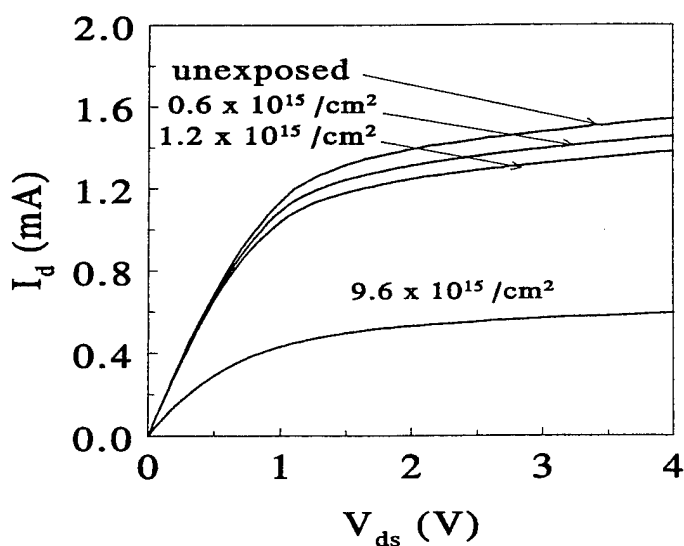


Figure 5.10 I_{DS} vs. V_{DS} characteristics of the device at a fixed V_{GS} for different electron doses.

The transfer characteristics (I_{DS} vs. V_{GS}) of the devices at $V_{DS} = 2.0 \text{ V}$ for different exposures were also measured and the threshold voltage (V_{th}) of the device for different exposures was

determined by extrapolating the linear portion of the transfer characteristics to $I_{DS} = 0$. The electron dose dependence of the threshold voltage V_{th} device is shown in Figures 5.11.

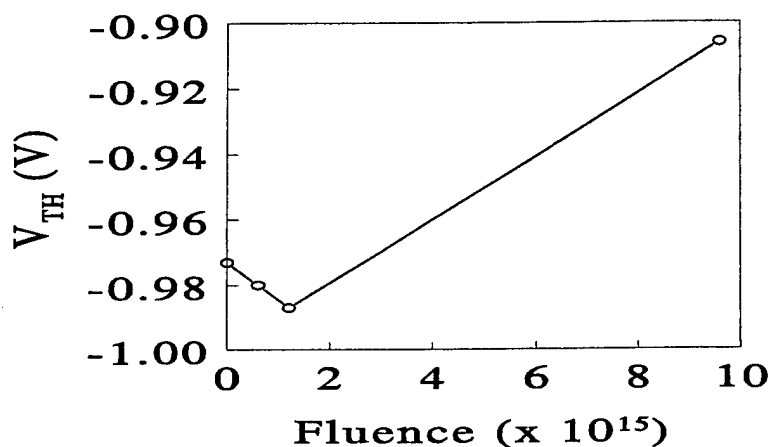


Figure 5.11 Electron dose dependence of the threshold voltage.

5.4 Neutron Radiation Effects in HEMT Devices

Neutron radiation effects in AlGaAs/GaAs HEMTs were first reported by Krantz *et al.* [5.3]. They attributed the threshold voltage shift observed their devices to the neutron-induced acceptor like traps in the channel (buffer) GaAs region. More recently, Papastamatiou *et al.* [5.4] reported a detailed study of the neutron radiation effects in HEMTs by analyzing the gate voltage (V_G) dependence of the sheet carrier concentration (N_s) by capacitance measurements and the sheet carrier concentration dependence of mobility (N_s vs. μ_s) from $I_{DS} - V_{DS}$ measurements. From this analysis they concluded that the threshold voltage shift observed in their devices is caused by the acceptor-like traps introduced in the AlGaAs donor layer and that the net acceptor concentration in the buffer layer decreases in contrast with the results of Krantz *et al.* In both these studies, even though good agreement was reported between the experiment and the respective physical model there was no verification of the proposed model by other independent measurements. To resolve this controversy we performed experiments that combine the I-V measurements of HEMT devices with Hall measurements on control samples subjected to neutron radiation along with the HEMT devices. The results of our investigation clearly shows that the neutron radiation induced threshold voltage shift is caused by the acceptor-like traps introduced in the GaAs buffer layer.

The samples used in this study were grown by molecular beam epitaxy. In addition to the HEMT device structures, control samples of single layers of GaAs and AlGaAs were also grown. The devices were fabricated by conventional photolithography and wet etching techniques. Devices with different gate lengths in the range from 6 μm to 20 μm were fabricated. Neutron irradiation was performed using the TRIGA Mark II reactor at OSU Radiation Center. For each dose, one small chip containing several devices, one sample of the as-grown device structure, one sample n-type GaAs and one sample of n-type AlGaAs were used. The last three samples had ohmic contacts at the corners and were used for Hall measurements. The devices were unbiased

during irradiation. All the samples were enclosed in cadmium boxes during irradiation to block the thermal neutrons.

The I_{DS} - V_{DS} characteristics of a typical device with a gate length of $8\text{ }\mu\text{m}$ for different doses are shown in Fig. 5.12. The data are plotted in normalized form (relative to unirradiated device) since different pieces cut from the same wafer (of a given type) were used for different doses. The I_{DS} - V_{GS} (transfer) characteristics of the same device for different neutron doses are shown in Fig. 5.13. The threshold voltage (V_{th}) was determined by extrapolating the I_{DS} - V_{GS} characteristics to $I_{DS} = 0$.

The decrease of drain current (at a given V_{GS}) with neutron dose is caused by a combination of the increase in V_{th} as well as the decrease in transconductance. The decrease in transconductance is caused by a decrease in sheet carrier concentration (for a given V_{GS}) and a decrease in carrier mobility. Moreover, the mobility is a function of sheet carrier concentration. A complete analysis of the neutron dose dependence of the I_{DS} - V_{DS} characteristics is quite complex and is currently under progress. We now focus on the physical mechanism responsible for the threshold voltage shift.

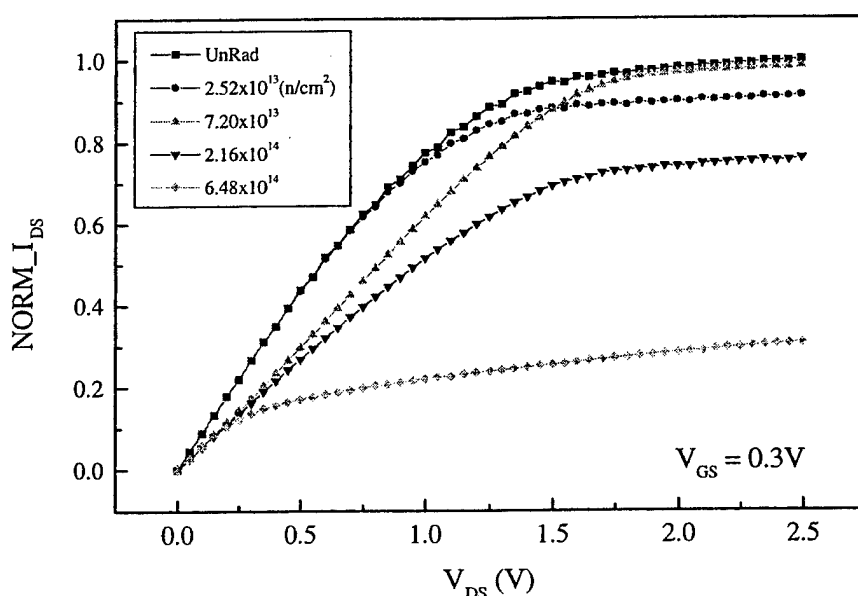


Fig. 5.12 The I_{DS} - V_{DS} characteristics of a typical device with a gate length of $8\mu\text{m}$ for different doses.

The threshold voltage shift (ΔV_{th}) of our devices as a function of neutron dose is shown in Fig. 5.14. The magnitude of ΔV_{th} is about the same as that observed by Krantz et al [5.3] as well as by Papastamatiou et al [5.4]. The threshold voltage of HEMTs is affected by both the donor concentration in the AlGaAs layer and by the acceptor concentration in the GaAs buffer layer. Other parameters that determine the value of V_{th} are not affected by neutron irradiation. Krantz et al assumed that the carrier removal rate in the n-type AlGaAs layer is the same as that of the n-

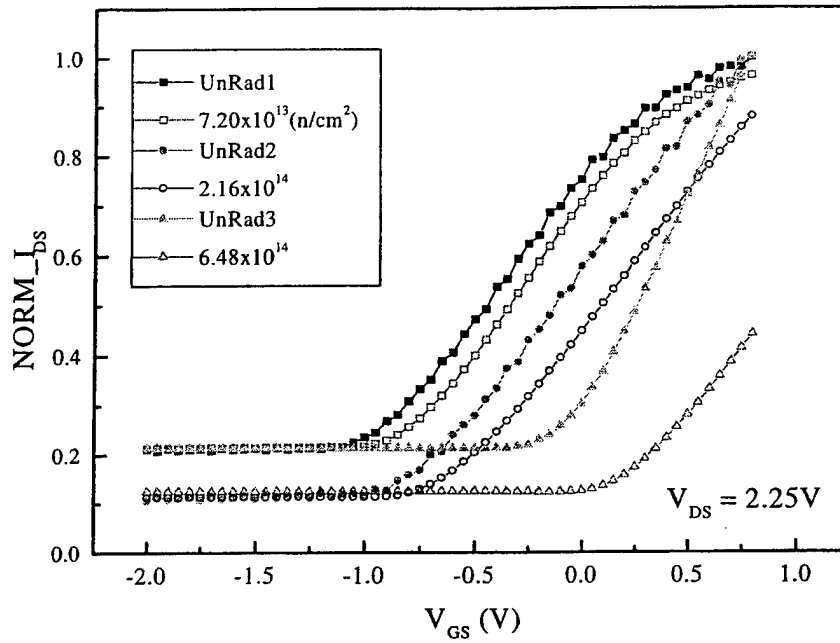


Fig. 5.13 The I_{DS} – V_{GS} characteristics of the same device for different neutron doses.

type GaAs reported in the literature and found that the contribution of AlGaAs layer to the threshold voltage shift is quite small. Hence they proposed that the observed increase in the threshold voltage is caused by the neutron induced introduction of acceptors in the buffer GaAs layer. They also derived an expression for the threshold voltage based on a strong inversion charge control model and obtained the acceptor introduction rate by fitting the experimental data of threshold voltage as function of neutron dose to this model. Papastamatiou et al derived an

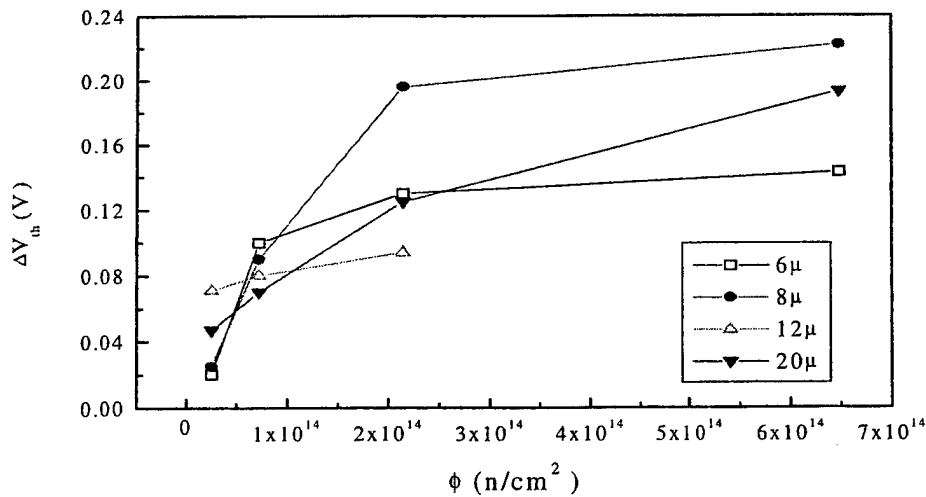


Fig. 5.14. The threshold voltage shift (ΔV_{th}) of the devices as a function of neutron doses

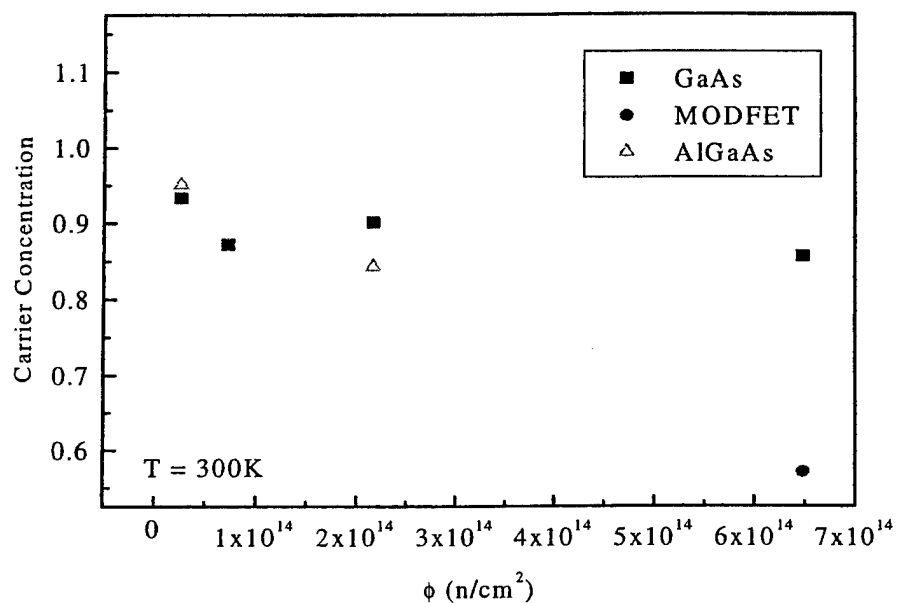


Fig. 5.15. The neutron dose dependence of normalized sheet carrier concentration of the 2-DEG in the HEMT structure, AlGaAs, and GaAs.

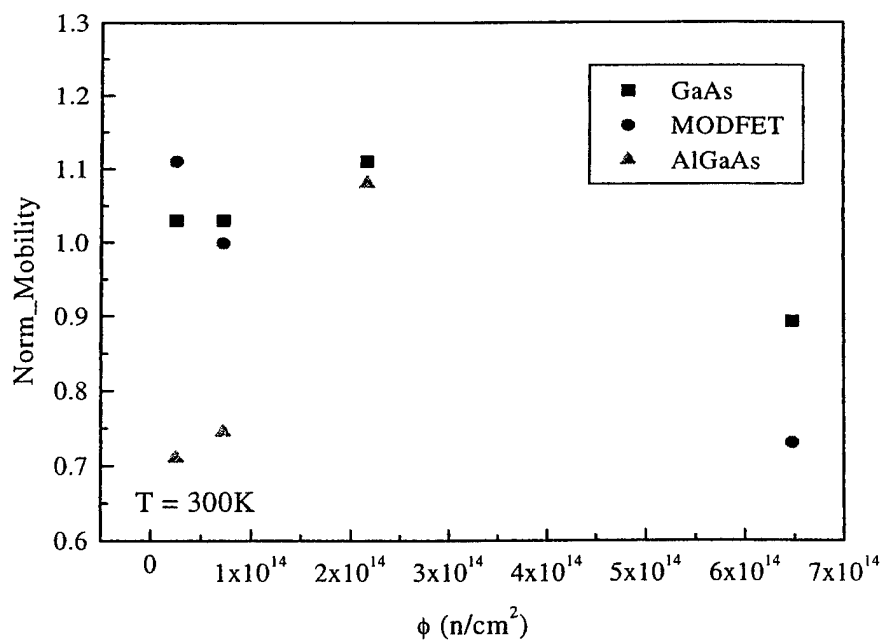


Fig. 5.16 The dose dependence of the normalized mobility of the 2-DEG in the HEMT structure, AlGaAs, and GaAs

expression for the sheet carrier concentration as a function of V_{GS} and fitted their experimental data to this model and obtained the defect introduction rates in both AlGaAs and GaAs simultaneously. Their analysis suggests a decrease of acceptor concentration in buffer GaAs and a carrier removal rate of $\sim 300 \text{ cm}^{-1}$ in AlGaAs, much larger than the reported values of carrier removal rate for GaAs.

In order to study the defect introduction rate independently we have carried out Hall measurements on control samples subjected to neutron irradiation as mentioned earlier. The neutron dose dependence of normalized sheet carrier concentration of the 2DEG in the HEMT structure, and the carrier concentrations in AlGaAs and GaAs are shown in Fig. 5.15. The dose dependence of the normalized mobility is shown in Fig. 5.16. From these plots it is clearly seen that the carrier concentration and mobility of the 2-DEG in the HEMT structures decreases with neutron fluence. On the other hand, the AlGaAs sample with an initial carrier concentration in the range of 10^{18} cm^{-3} and the GaAs sample with an initial carrier concentration in the range of 10^{17} cm^{-3} both show only a marginal decrease with neutron dose. Unfortunately we could not perform Hall measurements on undoped GaAs similar to the buffer layer of the HEMT structure since they were very highly resistive.

From this experiment, it is clear that the carrier concentration reduction in the HEMT structures and the threshold voltage shift of the HEMT devices are related to the neutron radiation induced defects in the buffer GaAs. Our theoretical calculations based on the self-consistent solution of Schrodinger-Poisson equations also shows that the decrease of 2-DEG concentration and the increase of threshold voltage can be explained by an increase in the acceptor concentration in the GaAs buffer layer. Our theoretical analysis is in accordance with the simpler analytical model of Krantz et al that assumes a triangular potential well at the heterojunction interface. By combining the experimentally determined threshold voltage as a function of neutron dose with our theoretical model for the dependence of the threshold voltage on the acceptor concentration in the GaAs buffer layer we have obtained the acceptor concentration in the buffer GaAs as a function of neutron dose. From this analysis the acceptor introduction rate in the buffer GaAs is found to be $\sim 10 \text{ cm}^{-1}$.

SECTION 6

Resonant Tunneling Diodes

Resonant tunneling diodes (RTDs) are important modern heterostructure devices that are used in a number of high speed / high frequency applications such as microwave mixers and oscillators. It is important to assess the radiation reliability of these device for applications involving space and nuclear environment. The devices used in our radiation studies are AlGaAs/GaAs/AlGaAs double barrier RTDs fabricated at MIT Lincoln Laboratory. A schematic cross section of the device structure is shown in Figure 5.1. One would expect these devices to be quite sensitive to radiation since any defects incorporated in the well or roughening of the interface would drastically affect the tunneling and thus deteriorate the device performance. However, our results show that these devices are surprisingly quite stable against gamma and beta radiation with little change in the peak current or peak to valley current ratio. The only observed change was a slight change in the peak voltage after gamma radiation. Beta radiation was found to have no effect on the devices at all.

InGaAs (50nm, $1e19$)	
n GaAs (100nm, $2e17$)	
n GaAs (100nm, $2-10e17$)	
	RTD
n GaAs (100nm, $2-10e17$)	double
	barrier
n+ GaAs (300nm, $2e18$)	
GaInP (10nm)	
n GaAs (150nm, $1-2e17$)	
SI substrate	

Fig. 6.1 Schematic diagram of the cross-section of the AlGaAs/GaAs/AlGaAs double barrier resonant tunneling diode (DBRTD) used in this work.

The radiation testing was done at the wafer level. A block diagram of the RTD test chip is shown in Figure 5.2. It consists of five blocks, each block containing 65 devices arranged in five columns by 13 rows. Because of the large number of devices in the test structure, a semi-automatic probing system was developed for testing. This system consists of a special probe card manufactured by JEM America (identical to the one used at MIT) and a Xynetics Model 1034X probe station. The test pads are $100\text{ }\mu\text{m}$ squares on a $200\text{ }\mu\text{m}$ pitch and are arranged in horizontal rows of 28 pads each that match exactly with the probe spacing. The testing for one row was done

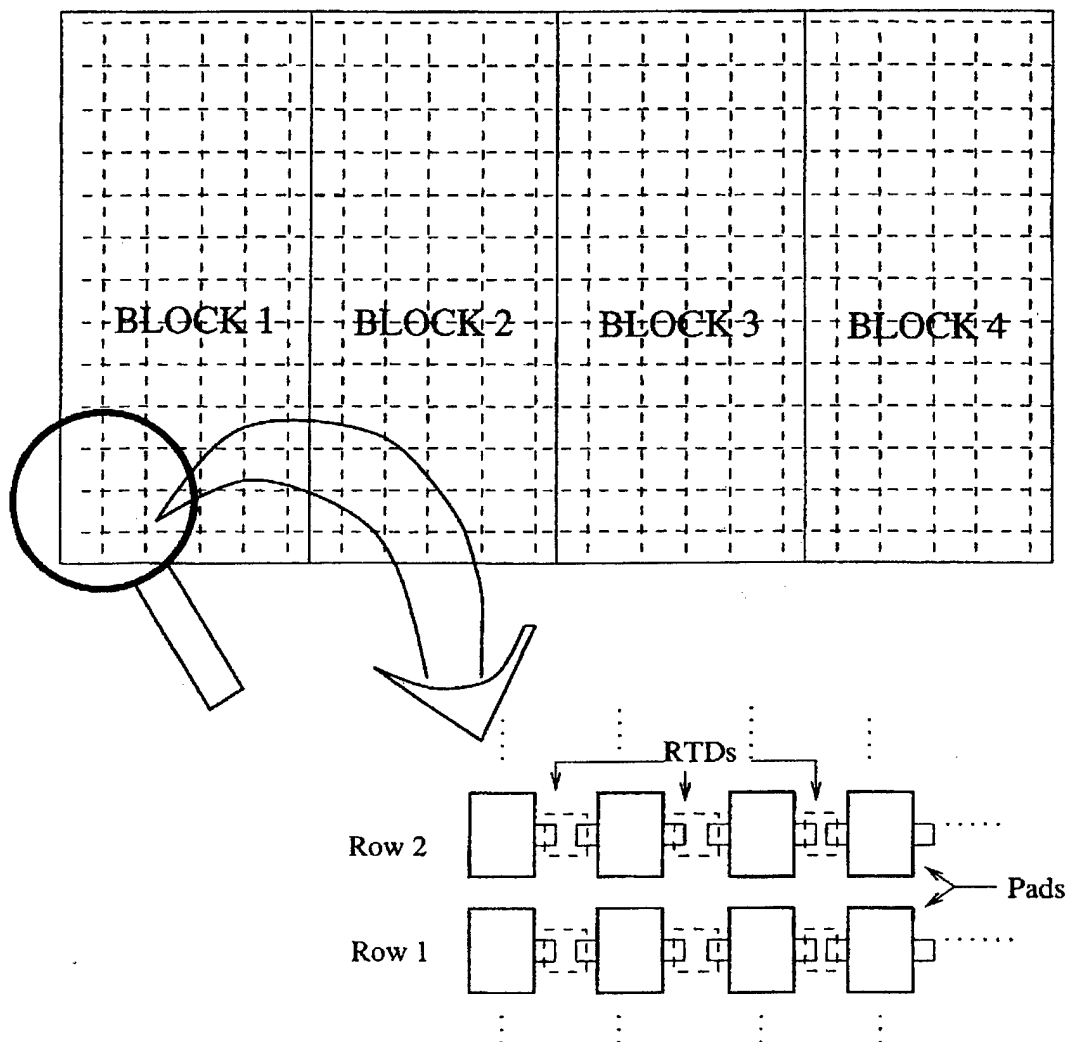


Figure 5.2 Block diagram of the device layout.

A. Gamma radiation results:

Typical I-V characteristics of a device before irradiation and after three doses of gamma radiation are shown in Figure 5.3. It is seen that the device exhibits excellent negative differential characteristics even at room temperature. Very little change in the I-V characteristics is observed even after 40 Mrad of gamma radiation. It is particularly significant to note that there is no change in the peak current or peak-to-valley current ratio. Some devices showed a slight change in the peak voltage. Average values of V_p , I_p etc. over a number of devices after different doses are summarized Table 5.1. Once again, it is seen that the only observed effect of gamma radiation

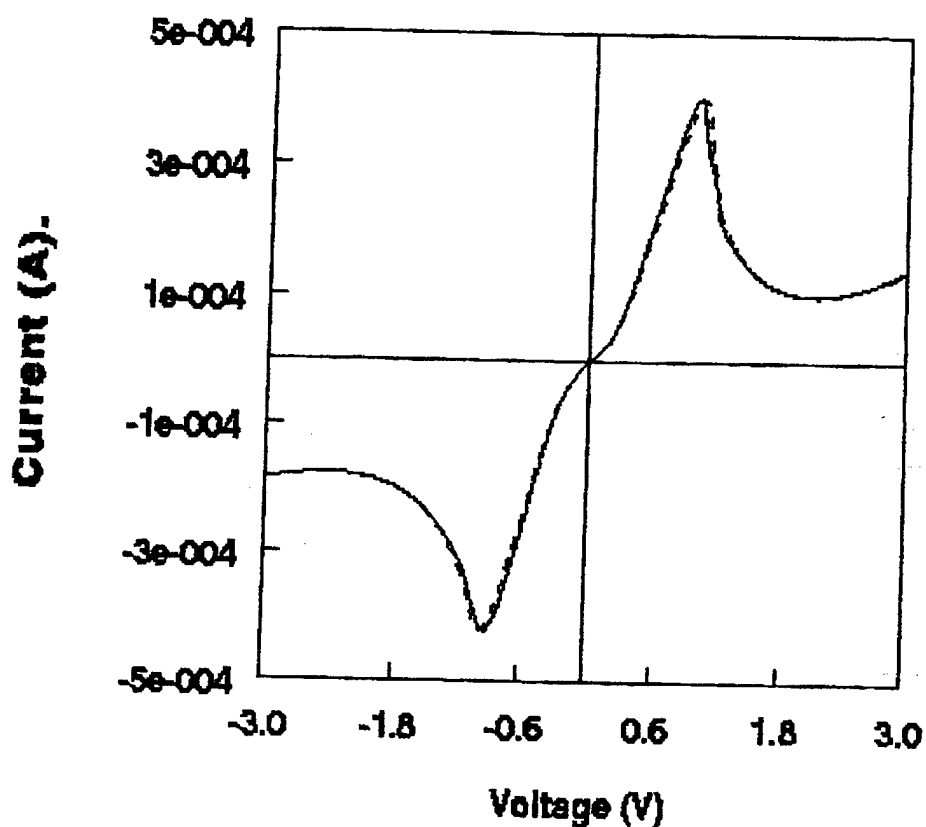


Figure 5.3 I-V characteristics of a typical RTD device after different doses of gamma exposure.

automatically by using a Tektronix switching card and HP4145 Parameter Analyzer and the probes were manually moved to the next row for further probing. is a slight change in V_p . We believe that the change in V_p is caused by an increase in the series resistance after radiation. The effect of series resistance on the V_v would be small because of the smaller value of I_v . The quantum well and the heterointerfaces do not seem to be affected very much by radiation since the I_p has not changed significantly.

Table 5.1 Gamma radiation results on RTDs.

Dose (Mrad)	V_p (V)	I_p (μ A)	V_v (V)	I_v (μ A)
0	1.245	435.2	2.49	151.05
1.0	1.29	437.8	2.53	151.4
10.0	1.4	418.25	2.59	152.66

40.0 1.57 426.4 2.63 152.3

B. Beta radiation results:

Our beta radiation experiments show that there is no change at all in the I-V characteristics of the devices after a dose of $\sim 1.1 \times 10^{16} \text{ e/cm}^2$. The average values of I_p , V_p , etc. over a large number of devices after several doses of beta radiation are summarized in Table 5.2. Unlike the gamma radiation results, the effect of series resistance after radiation is also found to be negligible since the V_p values did not show any change.

Table 5.2 Beta radiation results on RTDs.

Dose (10^{15} e/cm^2)	V_p (V)	I_p (μA)	V_v (V)	I_v (μA)
1.5	0.783	242.5	1.857	86.47
3.5	0.833	241.06	1.859	85.02
7.5	0.801	241.98	1.863	86.46
115	0.79	240.06	1.86	86.61

SECTION 7

CONCLUSIONS

In this program we conducted detailed experimental investigation of gamma, electron and neutron irradiation effects on HEMTs, HBTs and RTDs. In all the cases the main focus was to understand the basic mechanism of degradation. The most extensive investigation was on HBTs. We studied both InP/InGaAs HBTs and AlGaAs/GaAs HBTs. The four major degradation effects observed in the case of HBTs are (1) current gain degradation (2) output conductance degradation (3) increase of $V_{CE,sat}$ and (4) increase of $V_{CE,offset}$. We have identified the basic mechanism associated with each of these degradation behaviors. The current gain degradation is due to the increase in the base current. The collector current for a given base-emitter voltage (V_{BE}) is unaffected by any type of radiation. This shows that there is no change in the current transport (by thermionic-field emission) across the base-emitter junction. Our work shows that the increase in the base current is due to the increased recombination in the B-E junction space charge region due to the radiation-induced displacement defects. The surface recombination in the polyimide passivated devices is not affected very much by radiation. This is in contrast with the radiation degradation of Si BJTs which show total dose effects due to the radiation-induced charges in the oxide at the junction boundary. The increase in the neutral base recombination is also found to be small for the small base thickness (~ 600 Å) devices studied. The physical mechanism for the output conductance degradation is the degradation of the base-collector junction breakdown voltage. The increase in $V_{CE,sat}$ is due to the increase in series resistance either in the emitter or collector most probably due to increase in contact resistance. The increase in $V_{CE,offset}$ is due to the displacement damage in the collector region which in turn increases the saturation current of the B-c junction.

HEMTs show two major degradation effects: threshold voltage shift and transconductance degradation. The basic mechanism responsible for both these effects is the displacement damage in the buffer layer near the 2-DEG channel. At the basic material parameter level, this displacement damage gives rise to a decrease in the 2-DEG channel concentration and the mobility which in turn affect the threshold voltage and transconductance at the device level. RTD's show the negligible degradation with gamma or electron radiation..

We also developed detailed quantitative calculations for the ionizing and non-ionizing dose in the materials of our interest for all the three types of radiation. This step is essential to correlate our laboratory-based experimental results to the expected degradation in the actual radiation environment. We have also used these calculations for a quantitative comparison of degradation of the same type of device (InP/InGaAs HBT) for all the three types of radiation.

We also developed our own SPICE model and detailed analytical device models to analyze the experimental data of device current voltage characteristics and identify the physical mechanisms responsible for the observed degradation effects.

Future directions

In this program we studied only the degradation of the DC characteristics of the selected heterojunction devices. A main extension of this program will be to study radiation effects on the RF performance of the devices. It will also be very useful to conduct experimental investigation

of radiation tolerance of other passivation schemes (SiO_2 , Si_3N_4 , etc.). Finally, the effects of proton radiation (an important component of space radiation) on these devices should be investigated.

BIBLIOGRAPHY

- 1.1 D.K. Nichols and V.A.J. van Lint, in *Solid State Physics*, Vol. 18, edited by F. Seitz and Turnbull (Academic Press, New York, 1966)pp. 1-54.
- 1.2 J.W. Corbett, "Electron Radiation Damage in Semiconductors and Metal", *Solid State Physics*, Supplement 7, Academic Press, New York, 1966.
- 1.3 F. Larin, *Radiation Effects in Semiconductor Devices*, Wwiley, New Your, 1968.
- 1.4 R.H. Chafin, *Microwave Semiconductor Devices: Fundamentals and Radiation Effects* Wiley-Interscience, New York, 1973.
- 1.5 C.C. Messenger and M.S. Ash, *The Effects of Radiation on Electronic Systems*, Van Nostrand, New York, 1986.
- 1.6 R. Zuleeg, "Radiation effects of GaAs Integrated Circuits" in *VLSI Electronics, Microstructure Science*, vol. 11, eds. N.G. Einspruch and W.R. Weisseman, Academic Press, 1985, pp. 391-436.
- 1.7 D.C. Tsui, A.C. Gossard and D.J. Dolan, "Radiation effects on modulation-doped GaAs-AlGaAs heterostructures," *Appl. Phys. Lett.*, vol. 42, 1983, pp. 180-182.
- 1.8 M.J. O' Loughlin, "Radiation effects in high electron mobility transistors: Total dose gamma irradiation," *IEEE Trans. Nucl. Sci.*, vol. NS-34, 1987, pp. 1808-1811.
- 1.9 W.T. Anderson, M. Simmons, W.F. Tseng, J.A. Herb, and S. Bandy, "Transient Radiation Effects in AlGaAs/GaAs MODFETs," *IEEE Trans. Nucl. Sci.*, vol. NS-34, 1987, pp. 1669-1675.
- 1.10 R.J. Krantz, W.L. Bloss, and M.J. O' Loughlin, "High energy neutron irradiation effects in GaAs MODFETs: Threshold voltage," *IEEE Trans. Nucl. Sci.*, vol. NS-35, 1988, pp. 1438-1443.
- 1.11 B.K. Janousek, R.J. Krantz, w.L. Bloss, W.E. Yamada and S. Brown, "Characteristics of GaAs HFETs and source follower FET logic inverters exposed to high energy neutrons," *IEEE Trans. Nucl. Sci.*, vol. NS-36, 1989, pp. 2223-2228. G.A. Schrantz, N.W. van Vannon, W.A. Krull, MA. Rao, S.I. Long, and H. Kroemer, "Neutron irradiation effects in AlGaAs/GaAs heterojunction bipolar transistors," *IEEE Trans. Nucl. Sci.*, vol. 35, pp. 1657 - 1661, Dec. 1988.
- 1.12 Y. Song, M.E. Kim, A.K. Oki, M.E. Hafizi, W.D. Murlin, J.B. Camou, and K.W. Kobayashi, "Effects of neutron irradiation on GaAs/AlGaAs heterojunction bipolar transistors," *IEEE Trans. Nucl. Sci.*, vol. 36, pp. 2155 - 2160, Dec. 1989.
- 1.13 S.B. Witmer, S.D. Mittleman, and S.J. Pearton, "Radiation effects on InP-based heterojunction bipolar transistors," in *InP HBTs: Growth, Processing and Applications*, B. Jalali and S.J. Pearton, Eds., Boston, MA: Artech House, 1995, pp. 195-228, ch. 6.
- 2.1 J. Lindhard, V. Nielsen, M. Schargg, and P.V. Thomsen, "Integral equations governing radiation effects", *Matematisk-fysiske Meddelesler*, 33(10), 1963, pp. 1-42.
- 2.2 B.T. Kelly, "Irradiation Damage in Solids", Pergamon Press, 1966.
- 2.3 M.J. Norgett, M.T. Robinson, and I.M. Torrens, "A proposed method of calculating displacement dose rates", *Nuclear Engineering and Design*, 33, 1975, pp. 50-54.
- 2.4 "Dosimetry of External Beta Rays for Radiation Protention", ICRU Report 56, 1997.
- 2.5 F.H. Attix, "Introduction to Radiological Physics and Radiation Dosimetry", John Wiley & Sons, 1986.
- 2.6 S.M. Seltzer and M.J. Berger, "Bremsstrahlung spectra of high-energy electrons and positrons by nuclei", *Nuclear Instrumentaion and Methods*, B12, 1985, p. 95.
- 2.7 G.P. Summers, E.A. Burke, MA. Xapsos, C.J. Dale, P.W. Marshall, and E.L. Petersen, "Displacement damage in GaAs structures", *IEEE Trans. Nucl. Sci.*, 35, 1987, pp. 1221-1226.
- 2.8 R.M. Curr, "The Coulom sacttering of high energy electrons and positrons by nuclei", *Proceeding of Royal Physical Society (London)*, A69, 1955, pp. 156-164.
- 2.9 M.J. Berger and J.H. Hubbell, NIST XCOM: Photon Cross Sections Database, <http://physics.nist.gov/PhysRefData/Xcom/Text/XCOM.html> (accessed 02/2000).

- 3.1 A. Bandyopadhyay, S. Subramanian, S. Chandrasekhar, A.G. Dentai, and S.M. Goodnick, "Degradation of DC characteristics of InGaAs/InP single heterojunction bipolar transistors under electron irradiation," *IEEE Trans. Electron Devices*, vol. 46, pp. 840-849, May 1999.
 - 3.2 A. Bandyopadhyay, S. Subramanian, S. Chandrasekhar, A.G. Dentai, and S.M. Goodnick, "Degradation of InGaAs/InP dingle heterojunction bipolar transistors under electron irradiation," *IEEE Trans. Electron Devices*, vol. 46, pp. 850-858, May 1999.
 - 3.3 Alexei Shatalov, "Radiation Effects in InP/InGaAs Herojunction Bipolar Transistors", Ph.D. Thesis, Oregon State University, 2000.
 - 3.4 A. Shatalov, S. Subramanian, S. Chandrasekhar, A. Dentai and S. Subramanian, "Electron irradiation effects in polyimide passivated InP/InGaAs single heterojunction bipolar transistors," *IEEE Trans. Nucl. Sci.*, vol. 40, pp. 1570-1577, Dec. 1999.
 - 3.5 J.J. Liou, L.L. Liou, and C.I. Huang, "Kink effect on the base current of heterojunction bipolar transistors", *Solid State Electronics* 36, 1993, pp. 1222-1224.
 - 3.6 M. Sotoodeh, A.H. Khalid, and A.A. Rezasadeh, "DC characterization of HBTs using the observed kink effect on the base current", *Solid State Electronics* 42, 1998, pp. 531-539.
 - 3.7 S.B. Witmer, S.D. Mittleman, and S.J. Pearton, "Radiation effects on InP-based heterojunction bipolar transistors," in *InP HBTs: Growth, Processing and Applications*, B. Jalali and S.J. Pearton, Eds., Boston, MA: Artech House, 1995, pp. 195-228, ch. 6.
 - 3.8 R.D. Schrimpf, "Recent advances in understanding total-dose effects in bipolar transistors", *IEEE Trans. Nucl. Sci.* 43, 1996, pp. 787-796.
 - 3.9 S. Subramanian, A. Sarkar, L. Ungier, and S.M. Goodnick, "Integrity of III-V heterojunction interfaces under gamma irradiation", *IEEE Trans. Nucl. Sci.* 44, 1997, pp. 1862-1869.
 - 3.10 Y. Song, M.E. Kim, A.K. Oki, M.E. Hafizi, W.D. Murlin, J.B. Camou, and K.W. Kobayashi, "Effects of neutron irradiation on GaAs/AlGaAs heterojunction bipolar transistors," *IEEE Trans. Nucl. Sci.*, vol. 36, pp. 2155 - 2160, Dec. 1989.
 - 3.11 A. Sarkar, S. Subramanian, and S.M. Goodnick, "Electron Irradiation Effects in AlGaAs/GaAs Single Heterojunction Bipolar Transistors", To appear in *IEEE Trans. Electron Devices*, 2000.
-
- 4.1 A. Sarkar, "Radiation effects in compound semiconductor heterostructure devices," M.S. Dissertation, Oregon State University, Corvallis, OR, August 1998.
 - 4.2 A. Sarkar, S. Subramanian, and S.M. Goodnick, "Electron Irradiation Effects in AlGaAs/GaAs Single Heterojunction Bipolar Transistors", To appear in *IEEE Trans. Electron Devices*, 2000.
 - 4.3 J.J. Liou, L.L. Liou, C.I. Huang, and B. Bayraktaroglu, "A physics-based analytical heterojunction bipolar model including thermal and high current effects," *IEEE Trans. Electron Devices*, vol. 40, pp. 1570-1577, Sep. 1993.
 - 4.4 C.H. Henry, R.A. Logan, and F.R. Merritt, "The effect of surface recombination on current in AlGaAs heterojunctions," *J. Appl. Phys.*, vol. 49, pp. 3530-3542, 1978.
 - 4.5 S. Tiwari, D.J. Frank, and S.L. Wright, "Surface recombination in GaAlAs/GaAs heterojunction bipolar transistors," *J. Appl. Phys.*, vol. 64, pp. 5009-5012, 1988.
 - 4.6 O. Nakajima, K. Nagata, H. Ito, T. Ishibashi, and T. Sugeta, "Emitter-base junction size effect on current gain H_{fe} of AlGaAs/GaAs heterojunction bipolar transistors," *Japan. J. Appl. Phys.*, vol. 24, pp. L596-598, 1985.
 - 4.7 C.T. Sah, R.N. Noyce, and W. Shockley, "Carrier generation and recombination in p-n junction characteristics," *Proc. IRE*, vol. 45, pp. 1228-1243, 1957.
 - 4.8 Y. Song, M.E. Kim, A.K. Oki, M.E. Hafizi, W.D. Murlin, J.B. Camou, and K.W. Kobayashi, "Effects of neutron irradiation on GaAs/AlGaAs heterojunction bipolar transistors," *IEEE Trans. Nucl. Sci.*, vol. 36, pp. 2155 - 2160, Dec. 1989.
 - 4.9 A.G. Chynoweth, W.L. Feldman and R.A. Logan, "Excess tunnel current in silicon Esaki junctions", *Physical Review* 121, 1961, pp. 684-694.

- 5.1 S. Subramanian, A. Sarkar, L. Ungier, and S.M. Goodnick, "Integrity of III-V heterojunction interfaces under gamma irradiation", IEEE Trans. Nucl. Sci. 44, 1997, pp. 1862-1869.
- 5.2 R.J. Krantz, W.L. Bloss, and M.J. O'Loughlin, "High Energy Neutron Irradiation Effects in GaAs Modulation Doped Field Effect Transistors: Threshold Voltage, IEEE Trans. Nucl. Sci., vol. 35, Dec. 1988, pp. 1438 - 1443.
- 5.3 M. Papastamatiou, N. Arpatzanis, G.J. Papaioannou, and A. Christou, "Neutron Radiation Effects in High Electron Mobility Transistors", IEEE Trans. Electron Devices, vol. 44, March 1997, pp. 364, 371.